Seismogeodetic Imaging of Active Crustal Faulting

Thesis by
Asaf Inbal

In Partial Fulfillment of the Requirements for the
degree of
Doctor of Philosophy

CALIFORNIA INSTITUTE OF TECHNOLOGY
Pasadena, California

2017
Defended August 18, 2016

ACKNOWLEDGEMENTS

I would like to acknowledge the immense support I have received from my mentors Jean-Paul Ampuero, Rob Clayton, and Jean-Philippe Avouac throughout my studies at Caltech. J.-P. Ampuero's rigorous approach and persistence, broad knowledge, scientific intuition and precision were a source of inspiration over these years. His guidance have shaped the manner in which I conduct scientific research. R. Clayton introduced me into to the subject of dense seismic array seismology. I was fortunate to learn from his rich experience and knowledge in the field of seismic wave propagation and migration, big data processing, regional tectonophysics, seismic field operations and more. His deep enthusiasm and joy of making scientific discoveries effectively acted as a powerful engine advancing my research. J.-P. Avouac introduced me into the field of geodetical imaging and finite fault inversions. His ample experience and deep understanding of tectonic processes on multiple spatio-temporal scales, the mechanics of faulting and friction helped in clarifying many concepts associated with the joint strain and earthquake approach. Alon Ziv provided important insights regarding the joint strain and seismicity analysis, which significantly contributed to the development of this technique. His timely and valuable advice helped me make difficult decisions at important junctions along the way. Discussions with Hiroo Kanamori and Mark Simons raised important issues and questions touching the foundations of seismological research, which helped sharpen my own scientific perspective. Dan Hollis provided us with the Long-Beach dense array data set, and was also helpful in conduction field work during our Lost Hills deployment. I would like to thank my wife Cecilia Iribarren for creating the stable and unshakable ground of true friendship, and to my parents Dodik and Shoshi Inbal, and my brother Boaz Inbal, who gave me the courage and strength to peruse my dreams.

To Cecilia and Amalia

ABSTRACT

Monitoring microseismicity is important for illuminating active faults and for improving our understanding earthquake physics. These tasks are difficult in urban areas where the SNR is poor, and the level of background seismicity is low. One example is the Newport-Inglewood fault (NIFZ), an active fault that transverses the city of Long-Beach (LB). The catalog magnitude of completeness within this area is M=2, about one order of magnitude larger than along other, less instrumented faults in southern California. Since earthquakes obey a power-law distribution according to which for each unit drop in magnitude the number of events increases by a tenfold, reducing the magnitude of completeness along the NIFZ will significantly decrease the time needed for effective monitoring. The LB and Rosecrans experiments provides a unique opportunity for studying seismicity along the NIFZ. These two array contain thousands of vertical geophones deployed for several-months periods along the NIFZ for exploration purposes. The array recordings are dominated by noise sources such as the local airport, highways, and pumping in the nearby oil fields. We utilize array processing techniques to enhance the SNR. We downward continue the recorded wave field to a depth of a few kilometers, which allows us to detect signals whose amplitude is a few percent of the average surface noise. The migrated wave field is back-projected onto a volume beneath the arrays to search for seismic events. The new catalog illuminates the fault structure beneath LB, and allows us to study the depth-dependent transition in earthquake scaling properties.

Deep aseismic transients carry valuable information on the physical conditions that prevail at the roots of seismic faults. However, due the limited sensitivity of geodetic networks, details of the spatiotemporal evolution of such transients are not well resolved. To address this problem, we have developed a new technique to jointly infer the distribution of aseismic slip from seismicity and strain data. Our approach relies on Dieterich (1994)'s aftershock model to map observed changes in seismicity rates into stress changes. We apply this technique to study a three-month long transient slip event on the Anza segment of the San Jacinto Fault (SJF), triggered by the remote M_w7.2, 2010 El Mayor-Cucapah (EMC) mainshock.

The EMC sequence in Anza initiated with ten days of rapid (≈100 times the long-term slip rate), deep (12-17 km) slip, which migrated along the SJF strike. During the following 80 days afterslip remained stationary, thus significantly stressing a segment hosting the impending M_w5.4 Collins Valley mainshock. Remarkably, the cumulative moment due to afterslip induced by the later mainshock is about 10 times larger than the moment corresponding to the mainshock and its aftershocks. Similar to sequences of large earthquakes rupturing fault gaps, afterslip generated by the two mainshocks is spatially complementary. One interpretation is that the stress field due to afterslip early in the sequence determined the spatial extent of the late slip episode. Alternatively, the spatial distribution is the result of strong heterogeneity of frictional properties within the transition zone. Our preferred model suggests that Anza seismicity is primarily induced due to stress transfer from an aseismically slipping principal fault to adjacent subsidiary faults, and that the importance of earthquake interactions for generating seismicity is negligible.

PUBLISHED CONTENT AND CONTRIBUTIONS

Inbal, A., J.-P. Ampuero, and J.-P. Avouac. “Locally and remotely triggered afterslip on the central San Jacinto Fault near Anza, CA, from joint inversion of strain and earthquake data”. In: *J. Geophys. Res.* In review. A.I. wrote and implemented the software used to process the strain and aftershock data, and perform the inversion ; generated the figures; analyzed the results; and wrote the manuscript.

Inbal, A., J.-P. Ampuero, and R.W. Clayton. “Localized deformation in the upper mantle revealed by dense seismic arrays”. In: *Science*. In press. A.I. wrote and implemented the software used to process the LB data set ; generated the figures; analyzed the results; and wrote the manuscript.

Inbal, Asaf, R.W. Clayton, and J.-P. Ampuero (2015). “Imaging widespread seismicity at mid-lower crustal depths beneath Long Beach, CA, with a dense seismic array: Evidence for a depth-dependent earthquake size distribution”. In: *Geophys. Res. Lett.* pp. 6314-6323. ISSN: 1944-8007. DOI: 10.1002/2015GL064942. URL: http://dx.doi.org/10.1002/2015GL064942. A.I. wrote and implemented the software used to process the LB data set ; generated the figures; analyzed the results; and wrote the manuscript.

TABLE OF CONTENTS

LIST OF ILLUSTRATIONS

1

INTRODUCTION

Elucidating the physical processes governing slip at the bottom edge of seismogenic faults is important for understanding the underlying mechanisms of earthquake nucleation, propagation, and arrest. However, due to the limited sensitivity of surface monitoring systems, the spatiotemporal evolution of slip at the brittle-ductile transition zone, and the coupling between seismic and aseismic slip at large depths, are not well resolved. This dissertation describes research focused on utilizing seismological and geodetic observations to better constrain a range of processes occurring at the roots of continental seismic faults. In order to improve our understanding of the physical processes governing deep fault slip, we have developed methodologies to process large, dense seismic array data, and to improve the resolution of geodetic inversions by incorporating information on the space-time evolution of seismicity.

Dense array seismology is an emerging field in earthquake source studies. Because the array sensor spacing is two orders of magnitude smaller than conventional seismic networks, it allows us to resolve the incoming wave-field at frequencies as high as 10 Hz. This attribute, together with the large number of sensors (>1000), makes such arrays ideal for purposes of microseismic monitoring, which is the primary tool for illuminating active faults. The quality of the seismic catalog is measured by its magnitude of completeness, M_c, defined as the magnitude above which all earthquakes are registered by the network. Earthquakes obey a scaling law according to which for each unit drop in magnitude the number of events increases by roughly tenfold, therefore reducing M_c in a given area by one unit will reduce the time needed for effective seismic monitoring by a factor of ten. Due to seismic attenuation, waves emitted from events occurring near the bottom edge of the seismogenic zone, the area in which large ruptures are thought to initiate, are more difficult to detect than ones emitted from shallower depths. In addition, recent observations of deep seismicity on crustal faults suggest that their size distribution falls off more rapidly than a power law. If deep crustal earthquakes obey a characteristic distribution, then their detection will become even more challenging, as the population is dominated by very small, albeit frequent, microearthquakes. The dense array methodology significantly increases the detectability of deep microearthquakes, offering the opportunity to resolve dynamic processes at depths and scales that are inaccessible to a sparse local network.

In Chapter 1, we describe a new methodology for efficient, simultaneous analysis of thousands of seismic channels. We apply this methodology to dense array data recorded near the Newport-Inglewood Fault Zone (NIFZ). This technique enabled us to reduce M_c in the target area by 2 units. The new catalog illuminates a transition from a diffused zone of deformation in the upper crust to a narrow ($\sim$ 1 km) seismically active zone that extends into the lithospheric mantle beneath the mapped trace of the NIFZ. Our observations uniquely constrain the spatial extent and degree of shear localization within the seismogenic crust and upper mantle, which are parameters that are usually very poorly determined. In addition, the catalog offers an opportunity to study the transition in earthquake scaling properties across the brittle-ductile transition zone. Our analysis demonstrates that the transition to a ductile deformation regime has profound implications on earthquake relaxation mechanisms, and style and degree of earthquake interaction along the NIFZ.

Geodetic inversions, which are the most important tool for mapping fault slip at depth, are routinely performed in a variety of tectonic environments, and used to constrain pre-, co-, and post-seismic deformation. Because of the large number of unknowns, slip inversions are underdetermined, and their solutions are non-unique. This issue is usually addressed by imposing smoothness constraints, which stabilizes the inversion at the expense of reducing its resolution. As a result, slip on deep fault segments (below 5 km in the case of near-vertical strike-slip faults) is usually very poorly resolved. To understand the mode of slip along deep fault portions, information on the location and timing of microseismicity is often used in conjunction with fault slip maps. Due to elastic interactions, the space-time patterns of seismicity are strongly tied to fault slip, and hence changes in earthquake occurrence are expected to reflect variations in underlying processes that control rupture nucleation, propagation, and arrest. Not only is the incorporation of seismicity helpful in resolving the fine scale characteristics of slip, it also allows us to quantify the style and degree of stress transfer from aseismic regions to seismically active areas, which, in turn, helps constrain the physics that govern deep fault slip.

In Chapter 2 we present an approach that accounts for time-dependent changes in fault slip and stress via a joint inversion of strain and seismicity data. Seismicity rate response to a stress change is quantified through a constitutive relation which is based on an empirical friction law (Dieterich, 1994). This enables us to infer

the fault's constitutive parameters, and thus to gain important insights onto physical mechanisms controlling slip. We have applied this approach to study transient slip events along the Anza segment of the San-Jacinto Fault. The results provide detailed slip maps at depths that are inaccessible to the surface geodetic network, and allow us to constrain the mode of static stress-transfer to seismically active fault segments. Our study shows that earthquake interactions are less important than aseismic slip for understanding the evolution of seismicity during the sequence. Additionally, the new on-fault stress maps are used to address the scale and amplitude of loading along the Anza Gap, a 35-km long segment which is expected to fail in a Mw > 7 event.

2

IMAGING MICROSEISMICITY WITH DENSE SEISMIC ARRAYS

2.1 Introduction

Earthquakes occurring along transform plate boundaries are generally confined to the upper portions of the crust, with upper-mantle deformation being predominantly aseismic (Maggi et al., 2000). Seismological investigations of active faulting at lower-crustal depths are limited by highly attenuated signals whose level barely exceeds the noise at the Earth's surface, and by the sparseness of regional seismic networks. Consequently, important physical parameters characterizing the transition from brittle fracture to ductile flow at the base of the seismogenic zone are generally very poorly determined (Bürgmann and Dresen, 2008).

Because seismic tomography usually cannot resolve features whose spatial extent is less than about 10 km in the mid-lower crust (Thurber et al., 2006; Kahraman et al., 2015; Shaw et al., 2015), the occurrence of localized shear at those depths is largely inferred from geological observation of ancient shear zones, where tectonic deformation can be accommodated within a region whose thickness does not exceed 2 km (Norris and Cooper, 2003). The presence of fault-generated melt in the form of pseudotachylytes injected into exposed mylonites, and the inferred subsequent ductile deformation of the two, indicate that seismic slip may occur within largely aseismic deep shear zones (White, 2012). This is often interpreted as resulting from ruptures that nucleate at shallow depth but penetrate into the deep ductile region enabled, for example, by thermal weakening mechanisms (Rice, 2006). Here, in contrast, we present evidence of significant seismicity that nucleates at lower-crustal to upper-mantle conditions along the Newport-Inglewood Fault Zone (NIFZ). Next, we describe the seismotectonic setting of the NIFZ.

2.2 Seismotectonic Background

The Los Angeles (LA) basin is a deep sedimentary basin traversed by several active faults, among which the NIFZ, a major boundary fault in southern California. The NIFZ is well manifested by a series of small hills trending to the NW that extend for about 64 km between Culver City and Newport Beach (Figure 2.1). Since it bounds some of the region's most productive oil fields, the NIFZ has been drilled extensively, and this has revealed a complex fault geometry that consists of several overlapping en-echelon strike-slip faults which cut through the oil bearing anticlines (Barrows, 1974; Bryant, 1988; Wright, 1991). In Long Beach (LB), tectonic motion is primarily accommodated by a single strand known as the Cherry Hill Fault, which is a right-lateral strike-slip fault. It is sub-vertical down to about 5 km, but may dip as much as 60° at larger depths (Wright, 1991).

While reflection seismic surveys provide extensive data on the geometry of the NIFZ above 5 km, the structure of the NIFZ at larger depths is not well resolved, thus obtaining precise earthquake locations at those depths is important for hazard mitigation. The spatiotemporal distribution of microseismicity provides valuable information on the mechanics of fault slip and earthquake interactions, and nucleation (Rubin, Gillard, and Got, 1999; Rubin, 2002; Ziv, 2006; Bouchon, Karabulut, et al., 2011; Bouchon, Durand, et al., 2013). Activity is LB is not easily associated with the NIFZ, and occurs primarily to the NE of the fault (Figure 2.1), with the largest recorded event being the 1933 $M_w 6.4$ LB earthquake, located about 10 km SE of LB (Hauksson and Gross, 1991).

The NIFZ, which hosts many deep earthquakes, is unusual in that it does not display the strong compression, relatively low heat-flow, or strong topographical relief associated with deep faults in southern California (Bryant and Jones, 1992; Magistrale, 2002; Hauksson, 2011). Moreover, given the local geotherm ($\sim$ 32°C/km (Price, Pawlewicz, and Daws, 1999)), deep NIFZ seismicity nucleates at depths where typical continental crustal rocks are expected to deform in a ductile manner. To understand the long-term mode of seismic deformation along that fault, we examined a relocated earthquake catalog from the Southern California Seismic Network (SCSN) (Hauksson, Wenzheng, and Shearer, 2012). We observed a systematic variation in the spatial pattern of microseismicity along the NIFZ strike, which we attribute to a transition in faulting style. Earthquake epicenters are tightly clustered on en-echelon strike-slip faults northwest of LB, but do not follow the mapped trace of the NIFZ to the southeast of LB (Figure 2.1A). From NW to SE, earthquake density decreases and maximum earthquake depth, which we define as the depth above which 95% of seismicity occurs, increases from 10 to 17 km. Along the same section, Moho depth decreases by about 5 km (Figure 2.1C). The opposite trends of focal and Moho depths represent an unusual case in which the increase in seismogenic depth is anti-correlated with crustal thickness (Hauksson, 2011). Finding such deep events is surprising on a slow (0.5-1 mm/yr (Grant et al., 1997)) tectonic fault as the NIFZ.

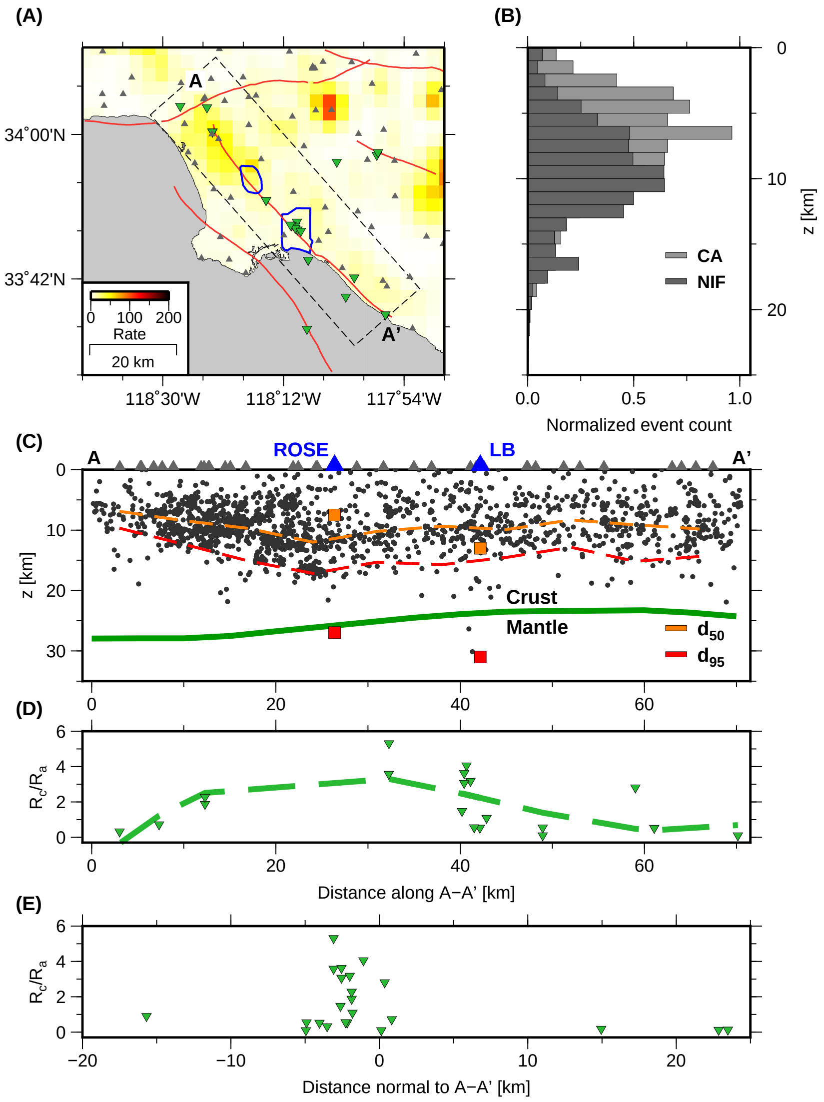

Figure 2.1: The spatial distribution of seismicity that occurred between 1980-2011 and was recorded by the Southern California Seismic California (SCSN), and Helium ratios (^{3}He/^{4}He) in the LA basin, which were measured and corrected for air contamination by *Boles et al.* (2015). (A) The earthquake density as a function of location. We used the color bar labeled "Rate" to indicate the spatially smoothed number of events over a 30-year period, binned in 9 km^2 squares. The location of Helium measurements, seismic stations, and dense seismic arrays are denoted by green inverted triangles, gray triangles, and blue polygons, respectively. We indicated the region from which we extracted the earthquakes we used in panels B and C by the dashed curve, and the surface trace of active faults by red curves. (B) The SCSN catalog seismicity depth distribution along the NIFZ and in southern California. (C) The depths of NIFZ seismicity and the Moho as function of location along line A-A' in panel A. The Moho is indicated by the green curve. The depths above which 50% and 95% of the earthquakes occur in the SCSN and back-projection derived catalogs are indicated by the orange and red dashed curves and squares, respectively. (D) The Helium ratios within the area enclosed by the dashed polygon in panel A as a function of distance along A-A'. The polynomial best fit to the observations is indicated by the dashed curve. (E) The Helium ratios as a function of distance normal to A-A'.

Ductile flow laws predict that the depth of the brittle-ductile transition increases with strain rate (Kohlstedt, Evans, and Mackwell, 1995; Hirth and Beeler, 2015). This should result in a shallower transition along the NIFZ compared to the faster San Andreas Fault (~ 2 cm/yr (Lindsey and Fialko, 2013)), assuming similar pressure and friction coefficient on these two faults. Moreover, if we make the common assumption that seismicity rate correlates with strain rate, then the observed 50-fold reduction in earthquake rate recorded by the SCSN from NW of Rosecrans to LB (Figure 2.1A), should have been accompanied by resolvably shallower seismicity. In order to improve our understanding of the spatial distribution of anomalous NIFZ seismicity, we examined earthquake properties in two NIFZ segments that host the deepest events reported in the regional catalog.

Our study is based on earthquake detection from continuous, simultaneous analysis of thousands of seismic channels from two dense arrays (Figures 2.1A). We used the 5200-sensor, 7×10 km LB, and 2600-sensor, 5×5 km Rosecrans arrays to compile catalogs with six and one month of data, respectively. The arrays contain 100 m spaced, 10 Hz vertical geophones sampling at 500 Hz. Data were down-sampled to 250 Hz, and band-pass filtered at 5-10 Hz. Signals at frequencies above this range may be affected by spatial aliasing, while analyzing frequencies lower than 5 Hz significantly decreases our spatial resolution. The recordings are contaminated by various anthropogenic noise sources, such as traffic from local freeways, landing at the LB airport, trains, and pumping in the LB Oilfield. The volume of the data set and the characteristics of anthropogenic signals in LB require that event detection be done automatically. Standard STA/LTA based detection algorithms are inadequate for our purposes, because such methods depend on the SNR of individual traces, and are thus easily distracted by spurious signals that originate from shallow noise sources in the vicinity of the geophones. Given the poor SNR, we turn to seismic array analysis to detect, locate, and determine the size of seismic events beneath LB. We only analyze nighttime data (6pm-6am), because during these intervals noise levels in LB significantly decrease.

2.3 Noise Mitigation via Downward Continuation

Our approach for event detection consists of two steps. In the first step we improve the SNR of the raw data by downward continuation, and in the second we continuously back-project the downward-continued data to search for coherent high-frequency radiation from structures beneath the array.

Downward continuation by phase-shift migration (Claerbout, 1976; Gazdag, 1978) is a common imaging technique used in geophysical exploration. We only analyze vertical component geophones, and thus neglect S-wave energy and use an approximate solution to the scalar (acoustic) wave equation. The acoustic wave field on a surface, $p(x, y, z_0, t)$, is used as a boundary condition to determine $p(x, y, z_0 + \Delta z, t)$, the wave field at depth $z = z_0 + \Delta z$. Assuming a depth-dependent, layered velocity model, the Fourier transformed data, $p(k_x, k_y, z_0, \omega)$, are downward continued to the target depth, z_n, with:

$$p(k_x, k_y, z_n, \omega) = p(k_x, k_y, z_0, \omega) \exp\left(-i \sum_{j=1}^{n} k_{z_j} h_j\right), \tag{2.1}$$

where k_x and k_y are the horizontal wavenumbers, ω is the frequency, and h_j is the thickness of the j'th depth increment whose velocity is v_j. The vertical wavenumber, k_{z_j}, is equal to:

$$k_{z_j} = \sqrt{\frac{\omega^2}{v_j^2} - (k_x^2 + k_y^2)}. \tag{2.2}$$

Imaginary values of k_{z_j} correspond to horizontally traveling evanescent waves. Their contributions to Equation 2.1 are discarded in our analysis. The space-time domain representation of the downward continued wave field is obtained by inverse Fourier transformation. In practice, data are downward-continued to a depth of 5 km, for which the velocity model is well constrained from borehole data, and which is deep enough to suppress surface noise.

Downward continuation assumes the data are uniformly spaced and periodic. To avoid having wrapped-around signals contaminating the records, the traces and spatial domain are first zero-padded out to twice and 8-times the spatial and temporal dimensions of the data, respectively. Furthermore, in order to suppress the influence of strong spatial variations of SNR on the procedure, the data are first normalized by its hourly RMS. We interpolate the data to a uniform grid whose cell size is 100×100 m, by assigning each data point a value equal to an exponentially weighted sum of its 4 nearest neighbors. Interpolation de-amplifies phases with high incidence angles that are mostly generated by shallow sources. The amplitude difference between the raw and interpolated data can be as high as 10% inside the LB Oil Field, the noisiest area covered by the array, and is at a level of 3-5% in most other parts of the array. From synthetic tests presented in the Section 2.6, this procedure has a negligible effect on the location of events in the depth range of interest. For a well-resolved wave field, downward continuation significantly decreases the amplitude of uncorrelated noise relative to coherent signals with high apparent velocities, which are focused back to their origin point at depth. Given the slow seismic velocities beneath the array and the short inter-station distances, wave fields with a characteristic frequency of up to about 15 Hz are well resolved by the LB array.

2.4 Event location via Back-Projection

In the second step of the analysis we back-project the envelope of the downward-continued data to a volume beneath the array. By stacking the signal's envelope we effectively reduce the sensitivity to unknown structure and focal mechanisms. The envelope, $s(t)$, is defined here by squaring the filtered, normalized, migrated waveforms, smoothing the squared waveforms using a 18-point (0.072 seconds) median window, and decimating to a new sampling rate of 50 Hz.

The stacked envelope is defined as:

$$S_i(t) = \frac{1}{n}\sum_{j=1}^{n} s(t + \tau_{ij}), \tag{2.3}$$

where n is the number of grid points on the downward-continuation target surface (same as the number of geophones) and τ_{ij} is the P-wave travel time difference between the j'th downward-continuation grid point and a reference grid point assuming a source located at the i'th back-projection grid point. When the source-receiver distance is much larger than the aperture of the array, the wave-front arriving at the array is typically approximated as a plane-wave. However, given the LB array geometry and the distance to the sources we wish to image, this approximation is not valid. We therefore migrate the seismic envelopes and project the energy back to the origin. Theoretical travel-times are computed on a mesh whose elements are 0.125 km^3 using a local 1-D velocity model extracted from the SCEC Community Velocity Model - Harvard (CVM-H) (Süss and Shaw, 2003; Plesch et al., 2011). We analyze the amplitude of the migrated stack to identify coherent energy in the frequency band of interest. Figure 2.2 presents the raw and downward-continued waveforms, and spatial distribution of the log of the stack amplitude of an $M_w = 0.4$ event whose focal depth is 14 km. Note that the arrivals are only visible after the data are downward-continued. Figure 2.3 presents the down-continued waveforms and surface ground motions due to a $M_w = 0.4$ that occurred beneath the Rosecrans array.

Our approach does not take into account any lateral heterogeneities in the velocity field, which may differ significantly from theoretical travel times computed using a 1-D model. Thus, a detailed 3-D velocity model should improve the accuracy of hypocentral locations. However, for the expected range of source-receiver distances in LB, the available 3-D model would only slightly modify the computed travel times, and hence introduce slight shifts to the locations obtained with a 1-D model. To confirm that, we compared travel time predictions from the CVM-H velocity model to the predicted travel times using the 1-D model, and found that the residuals are up to 5% of the travel time along the path, which would introduce location shifts that are smaller than our location uncertainties. This suggests that our interpretations are not strongly dependent on the velocity model we use.

2.5 Probabilistic Approach for Event Detection in Back-Projection Images

The detection procedure is carried out by analyzing the filtered, normalized, downward-continued, stacked envelopes. We stack (delay and sum) the envelopes of the downward continued waveforms for each potential position, window the stack for each position in our grid with 5-second, non-overlapping windows, construct a back-projection image from the peak amplitude of each window, and select the location that corresponds to the maximum of the image. We end up with a time-series containing the maxima of the back-projection image, on which the detection is made. Figure 2.4a shows the distribution of the logarithm of amplitudes of the migrated envelopes for a node located in the middle of our grid during one night of recordings. Figure 2.4b shows the distribution of the maxima in the 5-seconds windows for the same time period. Because the noise is log-normally distributed, the ensemble of observations containing its maxima belongs to a Gumbel distribution.

A 5-second window is identified as containing a true event if its maximum amplitude exceeds a threshold corresponding to 5 times the MAD of the distribution of noise. This value allows us to determine the probability of false detections, which is the probability that a sample randomly drown from the ensemble of the stack maxima is actually noise. The probabilities can be computed based on the fact that the stack maxima belongs to a Gumbel distribution, but the signal we wish to detect is belongs to a power-law or exponential distributions. To estimate the probabilities we generate 1000 realizations of Gaussian noise whose variance is equal to the variance in the back-projection images, select the maxima of each realization, and use a maximum-likelihood estimator to fit the data to a Gumbel distribution. For a given threshold value T, the probability of false detection is estimated by using:

$$P = 1 - F(T; \mu, \beta), \tag{2.4}$$

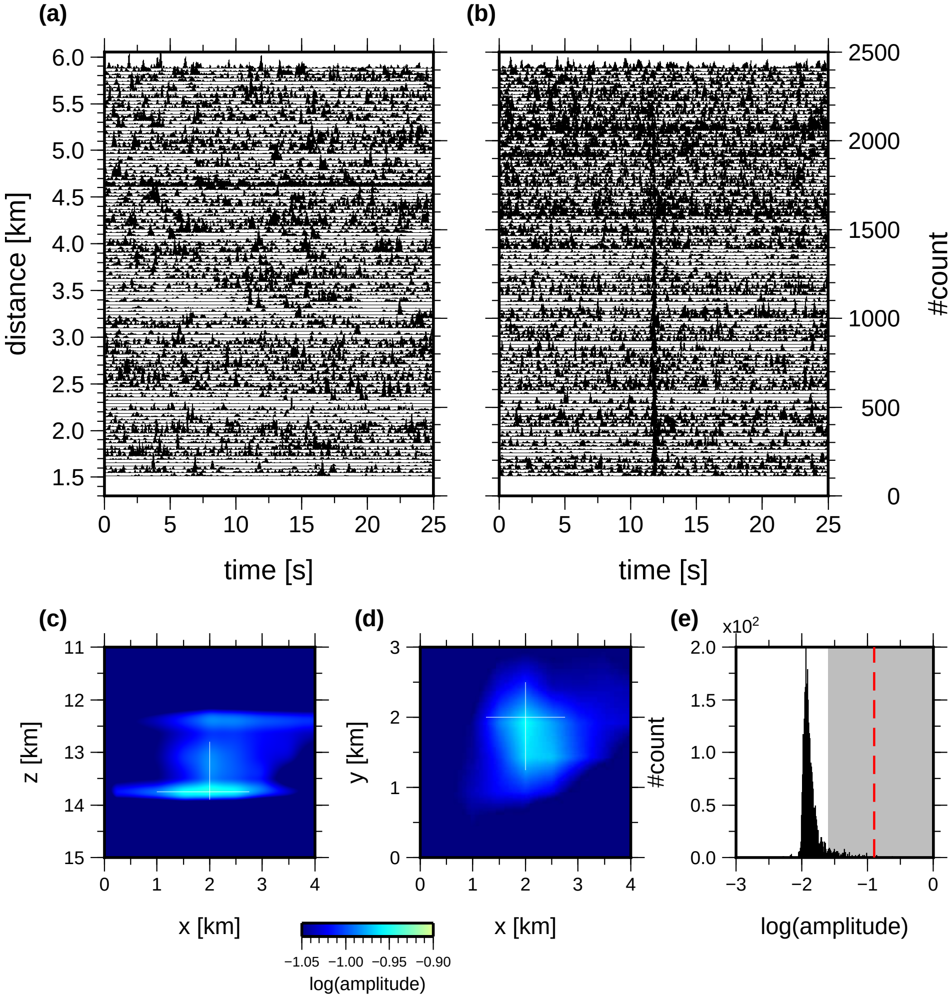

Figure 2.2: Amplitude as a function of time for traces containing a $M_w = 0.4$, and back-projected stack amplitude as a function of position. a. Waveform envelopes before downward-continuation. b.After downward continuation to a depth of 5 km. Vertical axes indicate epicentral distance (left) and trace count (right). Traces are normalized by their maximum. c. Log of maximum stack power for a 5-second window projected onto a vertical cross-section oriented EW. d. Map view of log of maximum stack power averaged over a depth range between 19 and 27 km. 1-MAD location uncertainty is indicated by white lines. e. Histogram of log of stack maxima in a 4-hour window around the detected event. Grey rectangle indicates region of acceptance, and red dashed curve indicates log of the stack maxima for the $M_w = 0.4$ event.

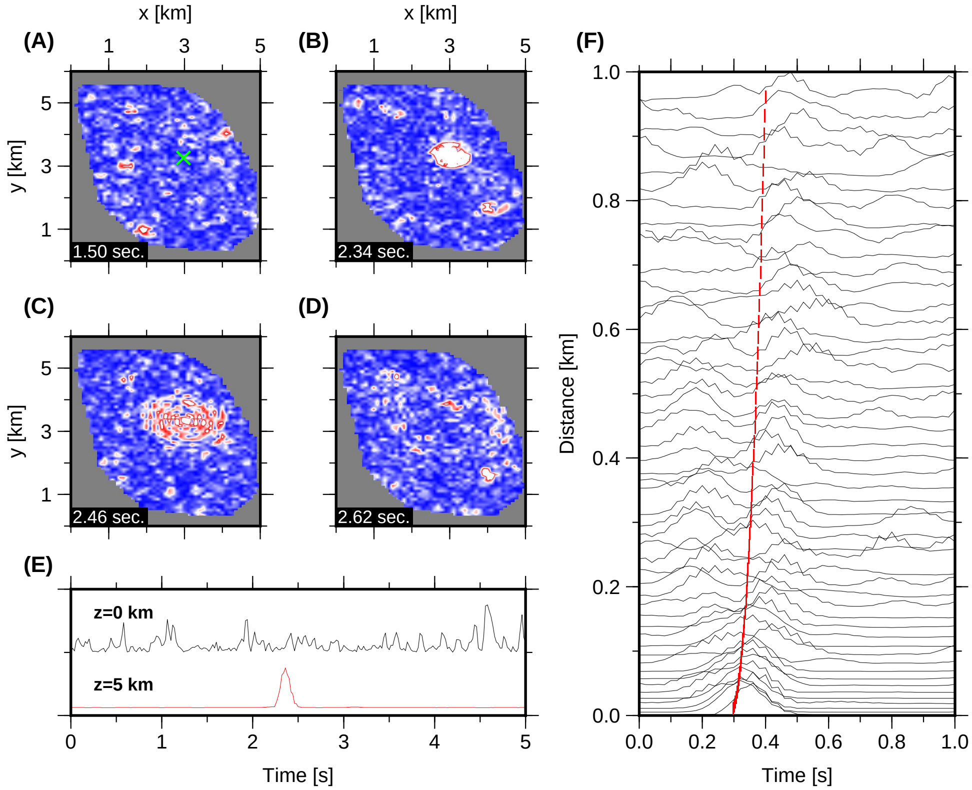

Figure 2.3: Ground velocity amplitudes in Rosecrans due to a M$_w$=0.4 earthquake. (A)-(D) Velocity envelopes of downward-continued waveforms as a function of position at 5 km depth. (E) Velocity envelopes at the surface (black) and at 5 km depth (red) for 2 collocated points within the array which are indicated by the green cross in panel A. (F) Downward-continued envelopes. Left and right axes indicate epicentral distance and trace count, respectively. Traces are normalized by their maximum. Red bars indicate expected P-wave arrival times.

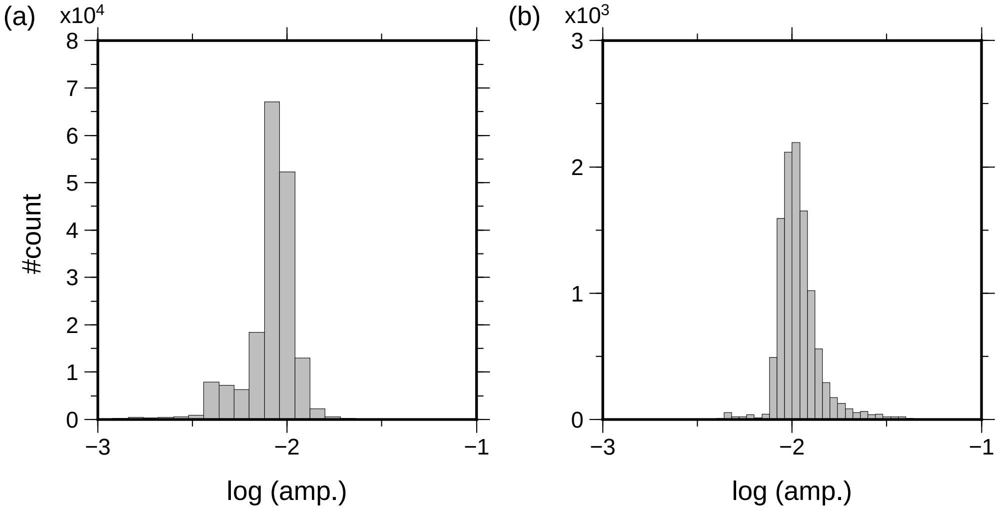

Figure 2.4: Amplitude distribution from one night of recordings. (a) Log amplitudes of stack at the center of the grid. (b) Peak log amplitude for 5-second windows.

where μ and β are the fitting coefficients. The rate of false alarms is obtained by multiplying the probability by the number of instances on which detection is preformed. The probabilities that a variable drawn from a Gumbel distribution will exceed the 5-MAD and 2-MAD thresholds are 3.22×10^{-7} and 1.27×10^{-4}, which translates to a constant rate of about 2×10^{-3} and 1 false alarm per night.

2.6 Location Error Estimation

To estimate the location uncertainty we first compute the surface seismograms due to a strike-slip point source. We use a 1-D velocity profile extracted from the SCEC CVM-H model. The synthetic traces are processed in the same fashion as the real data. We spatially interpolate the seismograms, downward-continue, and back-project the migrated envelopes onto the volume beneath the array. We then add noise whose distribution is derived from the real data and perform the detection. Our detection scheme operates on the images maximum amplitudes.

We estimate the location uncertainty from Monte-Carlo simulations. In each simulation we perturb the amplitudes of the synthetic back-projection images with log-normally distributed, spatially uncorrelated noise, and extract the location of the node with the largest perturbed amplitude. We perform 1000 simulations and

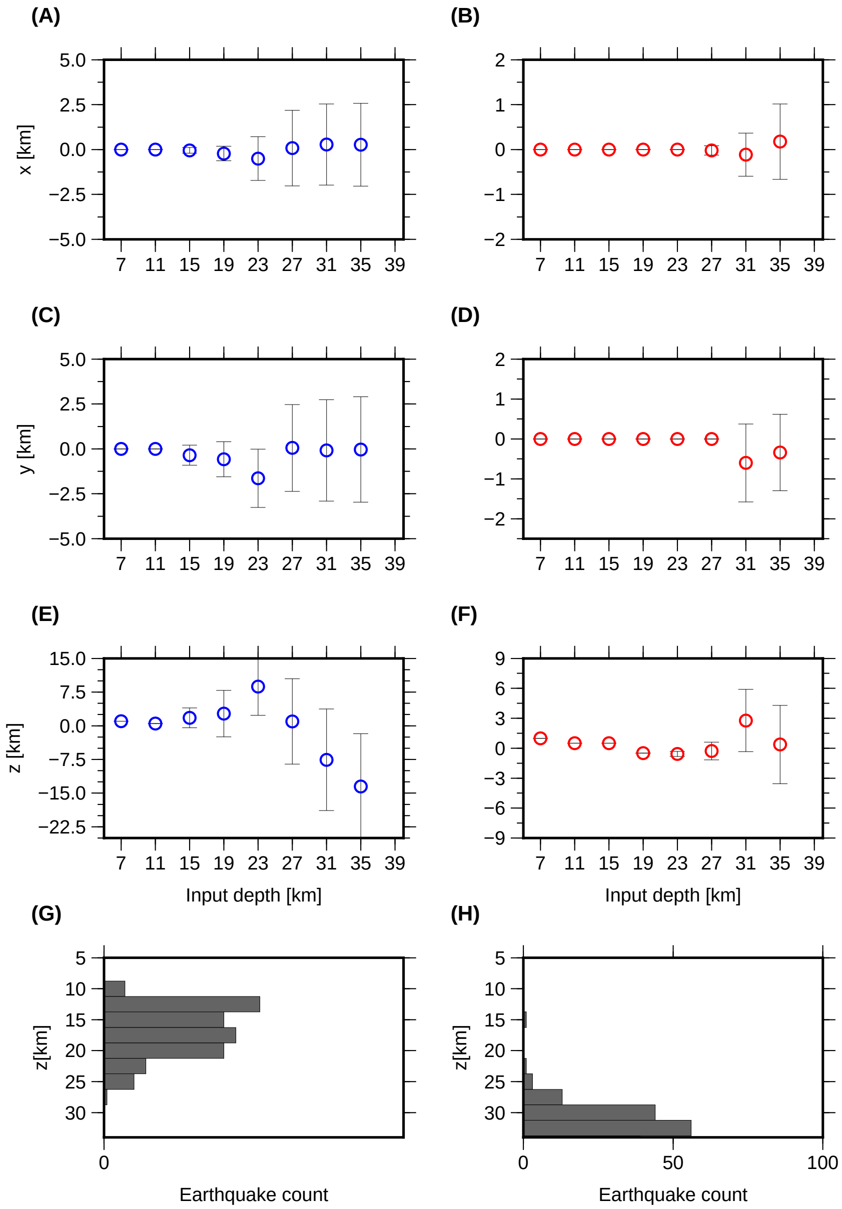

Figure 2.5: The location errors derived from synthetic tests. The Left and right columns are for input sources with M_w=0.5 and M_w=1.5, respectively. For each input magnitude, we show the difference between input and output x, y, and z coordinates in panels A-B, C-D, and E-F, respectively. The error bars indicate 1-sigma uncertainties. Focal depth distribution in LB for events with $0.4 < M_w < 0.5$, and $M_w > 1.5$ are shown in panels G and H, respectively.

report the mean and standard deviation of the output locations. Figure 2.5 presents the error analysis for synthetic sources whose depth varies between 7 to 35 km. For events with $M_w > 1.5$, our procedure accurately recovers the input locations down to depth of about 27 km. The uncertainty on the location of a source located at a depth of 31 km (below the Moho in our study area) is about 3 and 1 km in vertical and horizontal directions, respectively. The location uncertainty on events with $M < 0.5$ at depths below 20 km is generally larger, however the majority of the smallest magnitude events in our catalog occupy shallower depths (Figure 2.5G).

2.7 Magnitude Determination

In order to determine the magnitude of the detected events we use a simulation-based calibration scheme. Unfortunately, the regional catalog does not contain any events that occurred during the survey within the target volume, which forces us to use a model to calibrate the amplitudes. We compute the surface seismograms due to a strike-slip point source with $M_w = 1$ and a 3 MPa stress drop using the frequency-wavenumber wave propagation method of Zhu and Rivera (2002) together with the velocity and attenuation structure from the CVM-H model. The entire catalog is calibrated with a single event since the corner frequencies of the reference and recorded events are much higher than the frequencies we analyze. In the same fashion as the real data, the synthetics are normalized, downward-continued, back-projected onto the input hypocentral locations, which populate the target volume at 1 and 2 km spacing in the horizontal and vertical directions, and interpolated to a finer grid using bi-cubic interpolation. Since the raw data are normalized by their hourly RMS, the process is repeated for the synthetic data using the RMS values of the raw traces. Our procedure determines event magnitudes from the amplitude ratio between the observed and synthetic data. Because the synthetic data are produced with a realistic attenuation model, the procedure does not require that we apply any attenuation corrections.

2.8 Results: Deep Faulting in Long-Beach and Rosecrans

Our catalog illuminates a transition from diffuse seismic deformation in the upper crust to localized deformation in the lithospheric mantle. Shallow seismicity (<15 km) in LB is diffuse and uncorrelated with the mapped fault trace or with the nearby oilfield (Figure 2.6A). To the southwest of the main NIFZ strand, we identify a NW-NNW striking segment that is mostly active between 12 and 20 km, but contains sparse seismicity outside this depth range. A second structure is located to the northeast. Below 20 km, this zone is very seismically active, but the location near the edge of the array prevents us from resolving its geometry in detail.

With increasing depth, seismicity progressively concentrates beneath the mapped trace of the NIFZ and the width of the seismically active zone decreases (Figure 2.6A-C). Below ~20 km seismicity localizes onto a 1 km wide area that is located directly beneath the mapped trace of the NIFZ. The vertical cross-section (Figure 2.6D) clearly shows that the fault dip below 15 km is near-vertical, and that it retains this geometry in the upper mantle. In particular, our observations do not support a previous suggestion that the NIFZ is truncated at shallow depths by an active detachment fault (Crouch and Suppe, 1993). Accounting for location uncertainties in our catalog, the deformation zone illuminated by deep LB seismicity is no more than 2 km wide, consistent with several exhumed mylonite shear zones (Norris and Cooper, 2003). We also find that deep seismicity (>20 km) accounts for at most 10%-20% of the cumulative long-term moment rate accommodated by the fault, assuming a slip rate 0.5 mm/year (Grant et al., 1997). Based on these results, we conclude that aseismic, viscous flow accommodates most of the deformation in the lower crust.

The spatial distribution of deep seismicity varies along the NIFZ strike. Seismicity in Rosecrans occurs along 4 or 5 strands that form a 5 km wide fault zone, which is active down to about 15 km, but contains few events below that depth. Unlike the LB segment, these strands appear to dip at up to 70° to the northeast (Figure 2.7). Multiple en-echelon strike-slip faults are generally observed at shallower depths along that section (Wright, 1991), and our study confirms that these structures are active at larger depths. If the Rosecrans catalog is representative of the long-term deformation along that segment, then the scarcity of deep seismicity suggests that the zone of deep, localized seismic deformation extends no more than 15 km along the NIFZ strike to the northwest of LB.

Independent evidence compatible with deep faulting comes from recent measurements of ^{3}He/^{4}He, a primary indicator of mantle-derived phases within the crust (Kennedy et al., 1997), in deep boreholes in the LA basin (Boles et al., 2015) (Figure 2.1A and 2.1D-E). ^{3}He enrichment is more than twice as high than along the much more tectonically active San Andreas Fault. The observed along-strike trend in the fraction of mantle derived Helium is remarkably well correlated with the seismicity depths in the regional catalog. They both first increase towards the southeast, then decrease somewhat and flatten southeast of LB (Figure 2.1C and 2.1D). Further evidence of the deep root of the NIFZ comes from the seismic imaging of a sharp vertical offset in the lithosphere-asthenosphere boundary (Lekic, French, and Fischer, 2011), which extends to a depth of about 90 km beneath the zone of deep seismicity and anomalous ^{3}He enrichment. We suggest that the narrow deformation zone hosting deep seismicity beneath LB acts as a major conduit for fluid transfer

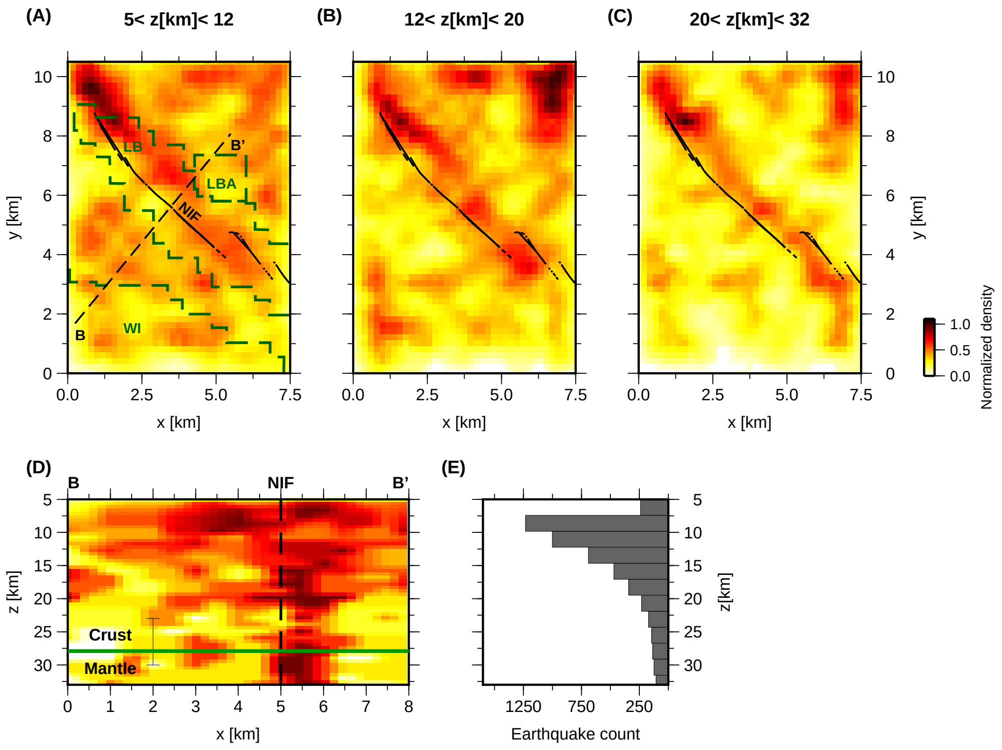

Figure 2.6: The spatial distribution of earthquake density we derived from a catalog spanning 93 nights of the LB array dataset. (A)-(C) A map view of event density in the 5-12, 12-20, and 20-32 km depth range. We normalized the densities in each panel by their maximum value. We represented areas with intense seismicity by orange and red colors, and areas devoid of seismicity by yellow and white colors. The NIFZ surface trace, and the local oilfields are denoted by black and green dashed lines, respectively. LB: Long-Beach oilfield, LBA: Long-Beach Airport oilfield, WI: Wilmington oilfield. (D) A vertical cross-section showing event density along line B-B' in panel A. We normalized the counts in each 2 km depth bin by their maxima. The Moho depth is indicated by a green curve, and the uncertainty on this estimate using previously published results. (E) The seismicity depth distribution in the LB array dataset.

between the upper mantle and the crust. These fluids in turn could provide a source of high pressures that extend the depth of seismic deformation.

2.9 Results: Depth-Dependent Earthquake Size Distribution and Temporal Clustering

The along-depth variation in the spatial distribution of NIFZ seismicity is most likely due to a rheological transition, which we expected to manifest itself as a resolvable change in the statistics of the catalog. To test this hypothesis, we analyzed the

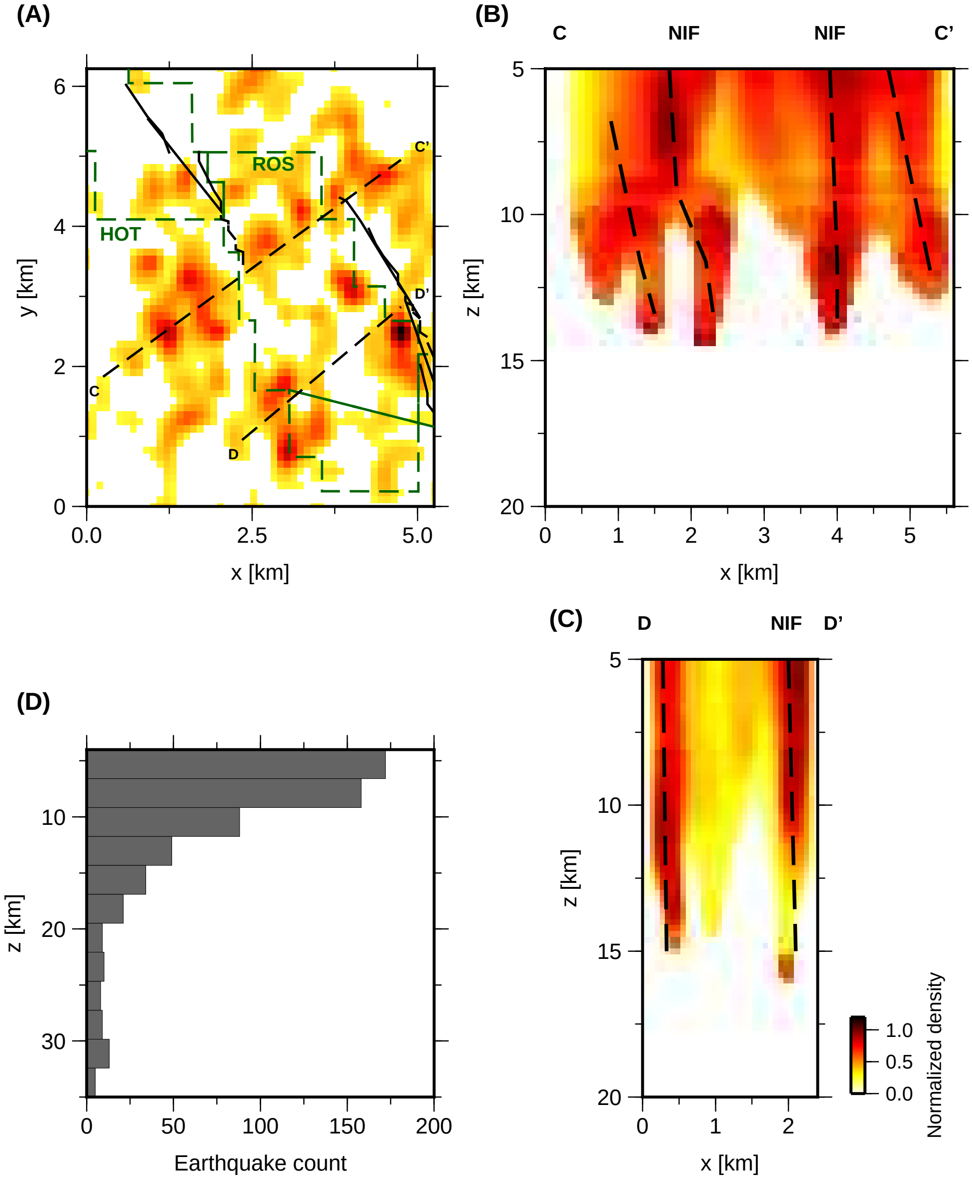

Figure 2.7: The spatial distribution of earthquake density from a catalog spanning 25 nights of the Rosecrans dataset. (A) Rosecrans catalog event density for the depth range 5-35 km. (B)-(C) A vertical cross-section along lines C-C' and D-D' in panel E. We normalized the densities in panel A by the maximum value, and the density in the cross-sections by the maximum in 2 km depth bins. (D) The event depth distribution. The location of the NIFZ surface trace, and inferred faults are indicated by solid and dashed black lines, respectively. The local oilfields are indicated by green dashed lines. ROS: Rosecrans, HOT: Howard Townsite.

temporal clustering of LB seismicity. Because our spatial resolution is limited by location uncertainties that are likely larger than the rupture dimensions of the earthquakes we imaged, we focused on aspects of the population's temporal and size distributions which varied on scales of several hundred meters.

We can investigate the degree of earthquake interaction using the ratio between the number of small and large earthquakes, commonly characterized by the b-value ($b = -d\log_{10}(N)/dM$, where N is the number of earthquakes of magnitude larger than M). In most tectonic environments b-values vary between 0.8 and 1.5 and decrease with increasing deviatoric stress (Scholz, 2015). Larger b-values are associated with an increase in ductility, and a reduction of fault strength, both in the lab (Scholz, 1968) and on natural faults (Spada et al., 2013). Recent observations of Low-Frequency Earthquakes (LFE), whose collective failure results in tectonic tremors, suggest that their number fall off rapidly with size (estimated from tremor amplitudes). Those studies suggest that LFE numbers are better described by an exponential distribution (Watanabe, Hiramatsu, and Obara, 2007; Shelly and Hardebeck, 2010; Sweet, Creager, and Houston, 2014), or a very steep power-law (Bostock et al., 2015). The rapid fall-off in LFE numbers with increasing size is similar to deep NIFZ seismicity. However, unlike other areas, the NIFZ catalog captures a depth-dependent transition in earthquake properties (Figure 2.8A-B). The distribution of shallow (<15 km) earthquakes in the 6 months period is consistent with that of the 30-years spanning SCSN catalog.

Note that for $b > 1.5$, the integral over the frequency-magnitude distribution does not converge at the limit of very small magnitudes (e.g. Molnar, 1979). However, as shown in Figure 2.8B, the deep event population is better fitted by an exponential distribution. This ensures that the integral over the event counts does converge even at a magnitude range which is below our detection level.

Spatio-temporal clustering is ubiquitous in earthquake catalogs and manifests most strikingly in the form of mainshock-aftershock sequences. We can model seismic activity as a random Poissonian process because it decorrelates at large distances or long time intervals. To determine if this behavior is depth-dependent, we analyzed the temporal autocorrelation functions of the spatially smoothed earthquake rates at different depth ranges. To estimate the degree of temporal clustering we divide the volume into shallow (<10 km) and deep (>25 km) depth ranges, and bin the events at 2.5×3 km, and 3×4.5 km cells, respectively. For each depth range and for each bin we compute seismicity rates by using a fixed data window. We resample the rate functions at 2-minute bins using linear interpolation, zero-pad the rates on both ends, compute their autocorrelation function, and stack the autocorrelations for each depth range. The autocorrelation function of a random process should appear as a zero-peaked delta function. The increase in degree of temporal clustering for shallow event clusters causes the stacked autocorrelation function to decay more gradually relative to the one computed for the deeper clusters.

We use larger bins for deeper events to ensure that the number of events in these clusters is not significantly different than the size of shallow clusters. However, the total number of deep events is only about 30% of the number of shallow events, which may bias our results. In addition, some artifacts are introduced into the autocorrelation analysis due to zero-padding of short sequences. We address these issues by analyzing a synthetic catalog in which event times are drawn from a Poissonian distribution, and whose temporal distribution is similar to the distribution of the deep events clusters (i.e. about 6-7 events per cluster, with average inter-event times of about 1.5 hours). We compute the rates of each simulated sequence, and, in the same fashion as the real data, compute and stack the autocorrelation functions. The dashed black curve in Figure 2.8C presents the results of the analysis using 30 simulated clusters. We find that the temporal distribution of deep earthquake clusters resembles more a random, Poissonian process than the distribution of the shallow event clusters.

To conclude, deep earthquake occurrence shows weak temporal correlation and resembles a random Poissonian process. This indicates diminished earthquake interactions at these depths.

2.10 Interpretation

Models of lithospheric strength may explain deep NIFZ seismicity while incorporating constrains on lower crustal rheology (Hirth and Beeler, 2015). However, relevant parameters such as temperature, grain size, lithology, and water content are generally poorly constrained. One possibility is that lateral as well as vertical compositional changes in the lower crust will promote brittleness within ductile, generally aseismic regions. A line of evidence supports the existence of considerable heterogeneity in material properties at lower-crustal to upper-mantle depth beneath the NIFZ. These include the observation of a sharp offset in the lithosphere-asthenosphere boundary extending to 90 km depth beneath the NIFZ (Lekic, French, and Fischer, 2011), a 10 km jump in the Moho 16 km to the west of the NIFZ (Schmandt and Clayton,

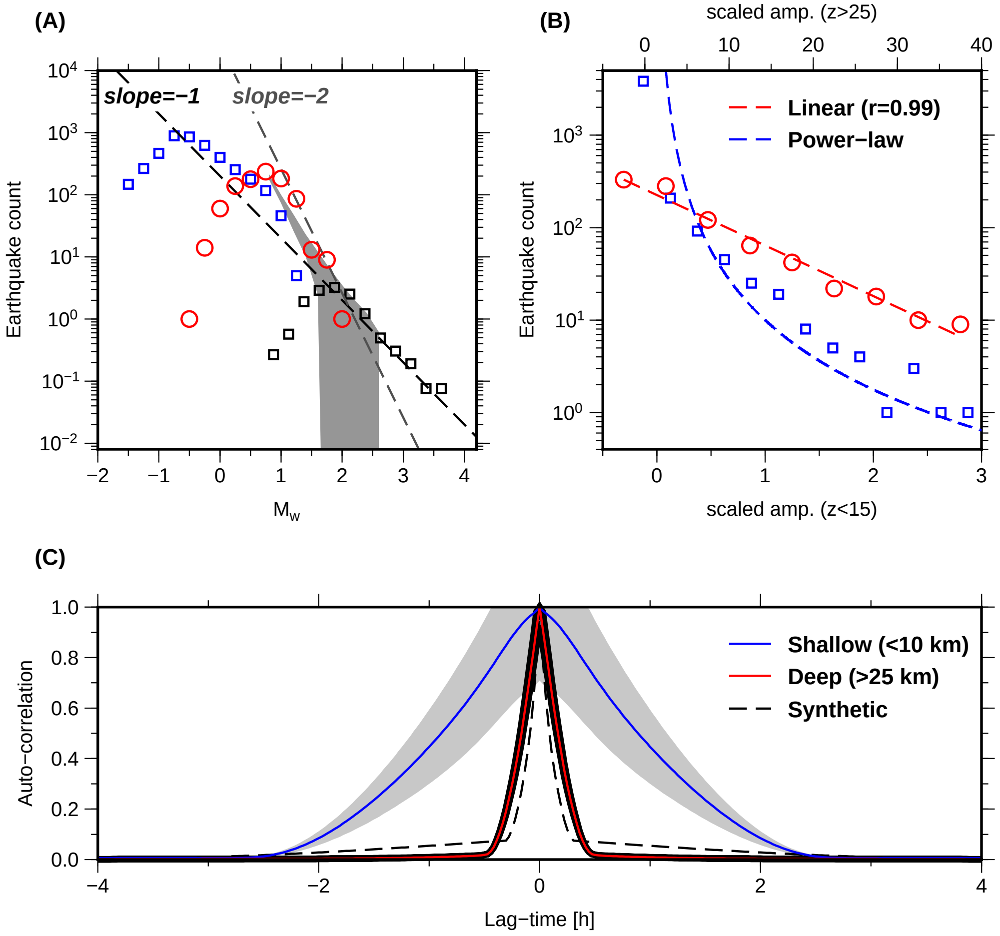

Figure 2.8: Temporal analysis and earthquake size distribution in LB. (A) The distribution of earthquake magnitudes. The blue squares and red circles are for shallow (<15 km) and deep (>25 km) events. Grey area indicates the expected variability in frequency distributions from synthetic catalogs with a *b*-value that lies between 1.7-1.9. The black squares are for the SCSN catalog, and are normalized according to the LB array spatio-temporal coverage. The slope of black and grey curves is equal to -1 and -2, respectively. (B) The distribution of earthquake signal amplitudes, which we define as the maximum of the downward-continued, migrated stack in a 5-second window containing the event, scaled by the maximum of the synthetic stack computed for a collocated source with $M_w = 1$. We indicated the best fitting exponential model, which appears linear in this semi-logarithmic scale, by a red curve. The blue curve is a power-law. (C) The autocorrelation as a function of lag-time between earthquake rate time-series for shallow (<10 km) at deep (>25 km) clusters. The blue and red curve indicate the average values we computed for 112 shallow and 52 deep clusters, respectively, with 1-sigma uncertainties in grey. The black dashed curve is for a synthetic earthquake catalog with a random, Poissonian distribution of earthquake occurrences.

2013), travel-time tomography showing a fast, possibly mafic body starting at ∼18 km beneath the LA basin (Hauksson, 2000), magnetic profiles suggesting that the NIFZ is the southern boundary of an ultramafic body (Romanyuk, Mooney, and Detweiler, 2007), and along-strike variations in the orientation of the principal stress axes (Hauksson, 1987), the distribution of mantle Helium (Boles et al., 2015), and near-surface (Wright, 1991) and deep faulting styles. Structural factors may also assist slip localization. The fabric of foliated mica schists, which are thought to be distributed at lower crustal depths beneath California (Porter, Zandt, and McQuarrie, 2011; Audet, 2015), possibly contain discrete surfaces accommodating seismic slip. Unstable frictional sliding of mafic rock has been observed in lab experiments (King and Marone, 2012; Mitchell, Fialko, and Brown, 2015), and in the field. (Ueda et al., 2008; Matysiak and Trepmann, 2012). This behavior may be further encouraged in the presence of fluids, either by reducing the effective normal stress or by promoting strain localization in narrow shear bands (Getsinger et al., 2013), perhaps akin to the localized deformation zone we imaged beneath LB (Figure 2.6C).

The rheological transition has profound implications on the degree of fault localization, relaxation mechanisms, and earthquake scaling properties. We can reconcile these observations with a conceptual framework in which deep deformation is predominately accommodated by ductile flow but interspersed by seismogenic asperities. Seismic rupture nucleated in a brittle asperity can penetrate into the surrounding region, up to a certain distance that generally depends on the asperity size and stress drop and on the resistance of the matrix. This effective radius R_e controls the range of interaction between asperities. The ratio between R_e and inter-asperity distance Δ determines the ability of asperities to break together in seismic events, despite the intervening creep, and thus the statistics of the earthquake catalog. When R_e/Δ is large, ruptures can involve multiple asperities. This strong interaction regime potentially leads to a scale-free, power-law earthquake size distribution (Figure 2.8A) and temporal clustering (Figure 2.8C), as observed at shallow depths. When R_e/Δ is small, asperities tend to break in isolation. In this weak interaction regime seismicity is temporally uncorrelated and, if asperities have a characteristic size, the earthquake size distribution is scale-bound, as observed in the deep NIFZ beneath LB. A systematic decrease of R_e/Δ with increasing depth may result from several processes, which are not necessarily independent. One possibility is a rheological control: R_e may decrease with depth due to increasing velocity-strengthening of the creeping matrix or decreasing stress drop within the asperities. Another possibility is a geometrical/structural control: at larger depths the range of asperity sizes (and hence of R_e) may be narrower or Δ may be larger, due for instance to lithological variations.

References

Audet, Pascal (2015). “Layered crustal anisotropy around the San Andreas Fault near Parkfield, California”. In: *J. Geophys. Res.* 120.5, pp. 3527–3543. ISSN: 2169-9313. DOI: `10.1002/2014JB011821`.

Barrows, A G (1974). “A review of the geology and earthquake history of the Newport-Inglewood structural zone, southern California”. In: *Calif. Div. Mines Geol. Spec. Rept.* 114.

Boles, J. R. et al. (2015). “Mantle helium along the Newport-Inglewood fault zone, Los Angeles basin, California: A leaking paleo-subduction zone”. In: *Geochem. Geophys. Geosyst.* 16.7, pp. 2364–2381. DOI: `10.1002/2015GC005951`.

Bostock, M. G. et al. (2015). “Magnitudes and moment-duration scaling of low-frequency earthquakes beneath southern Vancouver Island”. In: *J. Geophys. Res.* 2015JB012195. DOI: `10.1002/2015JB012195`.

Bouchon, M., V. Durand, et al. (2013). “The long precursory phase of most large interplate earthquakes”. In: *Nature Geo.* 6.4, 299–302. DOI: `{10.1038/NGEO1770}`.

Bouchon, M., H. Karabulut, et al. (2011). “Extended Nucleation of the 1999 M-w 7.6 Izmit Earthquake”. In: *Science* 331.6019, 877–880. DOI: `{10.1126/science.1197341}`.

Bryant, B. (1988). “Recently active traces of the Newport-Inglewood fault zone, Los Angeles and Orange Counties”. In: *Calif. Div. Mines Geol. Open-File Rept.* 88-14.

Bryant, B. and L. Jones (1992). “Anomalously deep crustal earthquakes in the Ventura Basin, southern California”. In: *J. Geophys. Res.* 97.B1, pp. 437–447. ISSN: 2156-2202. DOI: `10.1029/91JB02286`. URL: `http://dx.doi.org/10.1029/91JB02286`.

Bürgmann, R. and G. Dresen (2008). “Rheology of the Lower Crust and Upper Mantle: Evidence from Rock Mechanics, Geodesy, and Field Observations”. In: *Annu. Rev. Earth Planet. Sci.* 36.1, pp. 531–567. DOI: `10.1146/annurev.earth.36.031207.124326`.

Claerbout, J F (1976). *Fundamentals of geophysical data processing : with applications to petroleum prospecting*. McGraw-Hill.

Crouch, J K and J Suppe (1993). “Late cenozoic tectonic evolution of the Los-Angeles basin and Inner California Borderland - A model for core complex like crustal extension”. In: *Geo. Soc. Am. Bull.* 105.11, 1415–1434. DOI: `{10.1130/0016-7606(1993)105<1415:LCTEOT>2.3.CO;2}`.

Gazdag, J. (1978). “Wave-equation migration with phase-shift method”. In: *Geophysics* 43.7, 1342–1351. DOI: `{10.1190/1.1440899}`.

Getsinger, A. J. et al. (2013). “Influence of water on rheology and strain localization in the lower continental crust”. In: *Geochem.Geophys.Geosyst.* 14.7, pp. 2247–2264. ISSN: 1525-2027. DOI: `10.1002/ggge.20148`.

Grant, L B et al. (1997). “Paleoseismicity of the north branch of the Newport-Inglewood fault zone in Huntington Beach, California, from cone penetrometer test data”. In: *Bull. Seis. Soc. Am.* 87.2, 277–293.

Hauksson, E. (1987). “Seismotectonics of the Newport-Inglewood fault zone in the Los-Angeles basin, southern California”. In: *Bull. Seismol. Soc. Am.* 77.2, pp. 539–561.

– (2000). “Crustal structure and seismicity distribution adjacent to the Pacific and North America plate boundary in southern California”. In: *J. Geophys. Res.* 105.B6, pp. 13875–13903. DOI: `10.1029/2000JB900016`.

– (2011). “Crustal geophysics and seismicity in southern California”. In: *Geophys. J. Int.* 186.1, pp. 82–98. DOI: `10.1111/j.1365-246X.2011.05042.x`.

Hauksson, E. and S. Gross (1991). “Source parameters of the 1933 Long-Beach earthquake”. In: *Bull. Seis. Soc. Am.* 81.1, 81–98.

Hauksson, E., Y. Wenzheng, and P. M. Shearer (2012). “Waveform Relocated Earthquake Catalog for Southern California (1981 to June 2011)”. In: *Bull. Seismol. Soc. Am.* 102.5, pp. 2239–2244. DOI: `10.1785/0120120010`.

Hirth, Greg and N. M. Beeler (2015). “The role of fluid pressure on frictional behavior at the base of the seismogenic zone”. In: *Geology* 43.3, pp. 223–226. ISSN: 0091-7613. DOI: `10.1130/G36361.1`.

Kahraman, M. et al. (2015). “Crustal-scale shear zones and heterogeneous structure beneath the North Anatolian Fault Zone, Turkey, revealed by a high-density seismometer array”. In: *Earth Planet. Sci. Lett.* 430, pp. 129–139. ISSN: 0012-821X. DOI: `http://dx.doi.org/10.1016/j.epsl.2015.08.014`.

Kennedy, B. M. et al. (1997). “Mantle fluids in the San Andreas fault system, California”. In: *SCIENCE* 278.5341, pp. 1278–1281. ISSN: 0036-8075. DOI: `10.1126/science.278.5341.1278`.

King, D. S. H. and C. Marone (2012). “Frictional properties of olivine at high temperature with applications to the strength and dynamics of the oceanic lithosphere”. In: *J. Geophys. Res.* 117. DOI: `{10.1029/2012JB009511}`.

Kohlstedt, D. L., B. Evans, and S. J. Mackwell (1995). “Strength of the lithosphere: Constraints imposed by laboratory experiments”. In: *J. Geophys. Res.* 100.B9, pp. 17587–17602. ISSN: 2156-2202. DOI: `10.1029/95JB01460`.

Lekic, V., S. W. French, and K. M. Fischer (2011). “Lithospheric Thinning Beneath Rifted Regions of Southern California”. In: *Science* 334.6057, pp. 783–787. ISSN: 0036-8075. DOI: `10.1126/science.1208898`.

Lindsey, E. O. and Y. Fialko (2013). “Geodetic slip rates in the southern San Andreas Fault system: Effects of elastic heterogeneity and fault geometry”. In: *J. Geophys. Res.* 118.2, pp. 689–697. DOI: `10.1029/2012JB009358`.

Maggi, A. et al. (2000). “Earthquake focal depths, effective elastic thickness, and the strength of the continental lithosphere”. In: *Geology* 28.6, pp. 495–498. DOI: `10.1130/0091-7613(2000)28<495:EFDEET>2.0.CO;2`.

Magistrale, H (2002). “Relative contributions of crustal temperature and composition to controlling the depth of earthquakes in Southern California”. In: *Geophys. Res. Lett.* 29.10. DOI: `10.1029/2001GL014375`.

Matysiak, A. K. and C. A. Trepmann (2012). “Crystal-plastic deformation and recrystallization of peridotite controlled by the seismic cycle”. In: *Tectonophys.* 530, pp. 111–127. DOI: `10.1016/j.tecto.2011.11.029`.

Mitchell, E. K., Y. Fialko, and K. M. Brown (2015). “Frictional properties of gabbro at conditions corresponding to slow slip events in subduction zones”. In: *Geochem.Geophys.Geosyst.* 16.11, pp. 4006–4020. DOI: `10.1002/2015GC006093`.

Molnar, P. (1979). “Earthquake recurrence intervals and plate tectonics”. In: *Bull. Seismo. Soc. Am.* 69.1, pp. 115–133. URL: `http://bssa.geoscienceworld.org/content/69/1/115`.

Norris, R. J. and A. F. Cooper (2003). “Very high strains recorded in mylonites along the Alpine Fault, New Zealand: implications for the deep structure of plate boundary faults”. In: *J. Struct. Geol.* 25.12, pp. 2141–2157. DOI: `http://dx.doi.org/10.1016/S0191-8141(03)00045-2`.

Plesch, A. et al. (2011). “Updates for the CVM-H including new representations of the offshore Santa Maria and San Bernardino basin and a new Moho surface”. In: *SCEC Annual Meeting*. Palm Springs, California.

Porter, Ryan, George Zandt, and Nadine McQuarrie (2011). “Pervasive lower-crustal seismic anisotropy in Southern California: Evidence for underplated schists and active tectonics”. In: *Lithosphere* 3.3, pp. 201–220. ISSN: 1941-8264. DOI: `10.1130/L126.1`.

Price, L. C, M. J. Pawlewicz, and T. A. Daws (1999). “Organic metamorphism in the California petroleum basins; Chapter A, Rock-Eval and vitrinite reflectance”. In: *U.S. Geol. Surv. Bull.* 2174-A. URL: `http://pubs.er.usgs.gov/publication/b2174A`.

Rice, J. R. (2006). “Heating and weakening of faults during earthquake slip”. In: *J. Geophys. Res.* 111.B5. ISSN: 0148-0227. DOI: `10.1029/2005JB004006`.

Romanyuk, T., W. D. Mooney, and S. Detweiler (2007). “Two lithospheric profiles across southern California derived from gravity and seismic data”. In: *J. Geodyn.* 43.2, pp. 274–307. DOI: `10.1016/j.jog.2006.09.011`.

Rubin, A. M. (2002). “Aftershocks of microearthquakes as probes of the mechanics of rupture”. In: *J. Geophys. Res.* 107.B7. DOI: `{10.1029/2001JB000496}`.

Rubin, A. M., D. Gillard, and J. L. Got (1999). “Streaks of microearthquakes along creeping faults”. In: *Nature* 400.6745, 635–641. DOI: `{10.1038/23196}`.

Schmandt, Brandon and Robert W. Clayton (2013). “Analysis of teleseismic P waves with a 5200-station array in Long Beach, California: Evidence for an abrupt boundary to Inner Borderland rifting”. In: *J. Geophys. Res.* 118.10, 5320–5338. DOI: `{10.1002/jgrb.50370}`.

Scholz, C. H. (1968). “The frequency-magnitude relation of microfracturing in rock and its relation to earthquakes”. In: *Bull. Seismo. Soc. Am.* 58.1, pp. 399–415.

– (2015). “On the stress dependence of the earthquake b value”. In: *Geophys. Res. Lett.* 42.5, pp. 1399–1402. DOI: `10.1002/2014GL062863`.

Shaw, J. H. et al. (2015). “Unified Structural Representation of the southern California crust and upper mantle”. In: *Earth Planet. Sci. Lett.* 415, pp. 1–15.

Shelly, D. R. and J. L. Hardebeck (2010). “Precise tremor source locations and amplitude variations along the lower-crustal central San Andreas Fault”. In: *Geophys. Res. Lett.* 37.14. L14301. DOI: `10.1029/2010GL043672`.

Spada, M. et al. (2013). “Generic dependence of the frequency-size distribution of earthquakes on depth and its relation to the strength profile of the crust”. In: *Geophys. Res. Lett.* 40.4, pp. 709–714. ISSN: 1944-8007. DOI: `10.1029/2012GL054198`. URL: `http://dx.doi.org/10.1029/2012GL054198`.

Süss, M. P. and J. H. Shaw (2003). “P wave seismic velocity structure derived from sonic logs and industry reflection data in the Los Angeles basin, California”. In: *J. Geophys. Res.* 108.B3. DOI: `10.1029/2001JB001628`.

Sweet, J. R., K. C. Creager, and H. Houston (2014). “A family of repeating low-frequency earthquakes at the downdip edge of tremor and slip”. In: *Geochem.Geophys.Geosyst.* 15.9, pp. 3713–3721. DOI: `10.1002/2014GC005449`.

Thurber, C. et al. (2006). “Three-Dimensional Compressional Wavespeed Model, Earthquake Relocations, and Focal Mechanisms for the Parkfield, California, Region”. In: *Bull. Seismol. Soc. Am.* 96.4B, S38–S49. DOI: `10.1785/0120050825`.

Ueda, T. et al. (2008). “Mantle earthquakes frozen in mylonitized ultramafic pseudotachylytes of spinel-lherzolite facies”. In: *Geology* 36.8, pp. 607–610. ISSN: 0091-7613. DOI: `10.1130/G24739A.1`.

Watanabe, T., Y. Hiramatsu, and K. Obara (2007). “Scaling relationship between the duration and the amplitude of non-volcanic deep low-frequency tremors”. In: *Geophys. Res. Lett.* 34.7. DOI: `10.1029/2007GL029391`.

White, J. C. (2012). “Paradoxical pseudotachylyte – Fault melt outside the seismogenic zone”. In: *J. Struct. Geol.* 38, pp. 11–20. ISSN: 0191-8141. DOI: `http://dx.doi.org/10.1016/j.jsg.2011.11.016`.

Wright, T. L. (1991). “Structural geology and tectonic evolution of Los-Angeles basin”. In: *Bull. Am. Ass. Pet. Geo.* 71.5, p. 629.

Zhu, L P and L A Rivera (2002). “A note on the dynamic and static displacements from a point source in multilayered media”. In: *Geophys. J. Int.* 148.3, 619–627. DOI: `{10.1046/j.1365-246X.2002.01610.x}`.

Ziv, A (2006). “On the role of multiple interactions in remote aftershock triggering: The Landers and the Hector Mine case studies”. In: *Bull. Seis. Soc. Am.* 96.1, 80–89. DOI: `10.1785/0120050029`.

Chapter 3

INFERENCE OF DEEP TRANSIENT SLIP FROM JOINT ANALYSIS OF STRAIN AND EARTHQUAKE DATA

3.1 Introduction

Continental strike-slip faults are mostly seismically active above 10 to 15 km depth, and exhibit predominantly aseismic behavior at larger depths. Due to the limited sensitivity of surface monitoring systems, the mechanical properties of the deep seismic-aseismic transition zone are not well resolved. One approach for probing the downward extent of crustal faults is to analyze the accelerated deformation following large mainshocks, which is typically characterized by rapid afterslip and numerous aftershocks. It has been long recognized that aftershocks can be driven by the stressing imposed by afterslip (e.g. Perfettini and Avouac, 2004; Lengliné and Marsan, 2009; Hsu et al., 2006; Pritchard and Simons, 2006; Chlieh et al., 2007; Perfettini and Avouac, 2007; Ozawa et al., 2012; Lengliné, Enescu, et al., 2012). However, a joint analysis of the two phenomena is challenging, mainly because it requires a sensitive geodetic network capable of detecting deformations that marginally exceed the signal due to non-tectonic sources, as well as a complete and accurate seismicity catalog. Designing an approach that will simultaneously satisfy both the geodetic and aftershock datasets is also complicated by the fact that aftershocks trigger their own aftershock sequences and redistribute stresses in their vicinity. Since the relative importance of earthquake interaction and aseismic fault slip for triggering of seismicity is unknown, and since afterslip and aftershock rates show similar temporal decay (e.g. Perfettini and Avouac, 2004), separating their effects in the observed seismicity is difficult.

Details of the space-time evolution of seismicity are therefore rarely used to constrain geodetic slip inversions. Instead, they have been used as a posterior test of consistency of the inversion solution with the notion that earthquakes are triggered at locations of increased Coulomb stress (King, Stein, and J. Lin, 1994). The results of such tests are not always positive. For example, Ziv (2012) found that most of the aftershocks in the first day following the 2004 $M_w 6.0$ Parkfield earthquake occurred in areas where a geodetic-only slip inversion, which fits well the one-day static GPS displacement data, predicted reduced Coulomb stresses.

Some authors have explored the possibility of using aftershocks to constrain the slip distribution under the assumption that the stress change due to slip is the dominant mechanism for aftershock triggering. One possibility is to optimize the correlation between Coulomb stress increase and aftershock locations (Seeber and Armbruster, 2000; Bennington et al., 2011; Wang et al., 2012). Another approach is to relate observed variations in seismicity rates to variations in stressing rate via the seismicity evolution model introduced by Dieterich (1994), which incorporates time-dependent earthquake nucleation and laboratory-motivated rate-and-state friction. This approach was applied to the 1992 Landers aftershock sequence (Gross and Kisslinger, 1997) and to infer stresses associated with volcanic deformation (Dieterich, Cayol, and Okubo, 2000). It was also used to jointly analyse seismicity and deformation during dike intrusions (Segall, Desmarais, et al., 2006; Segall, Llenos, et al., 2013) and aseismic transients (Lohman and McGuire, 2007). A related approach was introduced by Ziv (2012) to infer the spatial distribution of co-seismic (mainshock) slip by joint inversion of geodetic data and first-day aftershock rates. Here, we extend this approach to study longer term aseismic transients occurring over time scales of weeks.

We analyze transient slip events and seismicity along the central San Jacinto Fault (SJF) near Anza, southern California, following the regional 2010 M7.2 El Mayor-Cucapah and the local 2010 M5.4 Collins Valley mainshocks. Both earthquakes were followed by numerous aftershocks near Anza and by deformation transients well recorded by Plate Boundary Observatory (PBO) borehole strain meters operative since 2008 (Figure 3.1). These strain transients are interpreted here as resulting primarily from triggered creep on the SJF. Our interpretation is based on strain changes that are coherent across the Anza PBO network, and that can be correlated with observed changes in the spatiotemporal distribution of seismicity. Following the approach of Dieterich, Cayol, and Okubo (2000), we map the observed seismicity rates to stress changes on secondary faults near the main SJF strand. We use the cumulative post-seismic stresses and strains to jointly invert for the distribution of afterslip in the first ten days following each mainshock, and to constrain the mode of stress transfer between creeping fault segments to seismically active clusters.

3.2 Seismotectonic Background

The SJF is the most seismically active fault in the Southern San Andreas Fault system. Between its northernmost section near San Bernardino to its southern termination near Borrego Springs, this 250 km long fault zone may be roughly

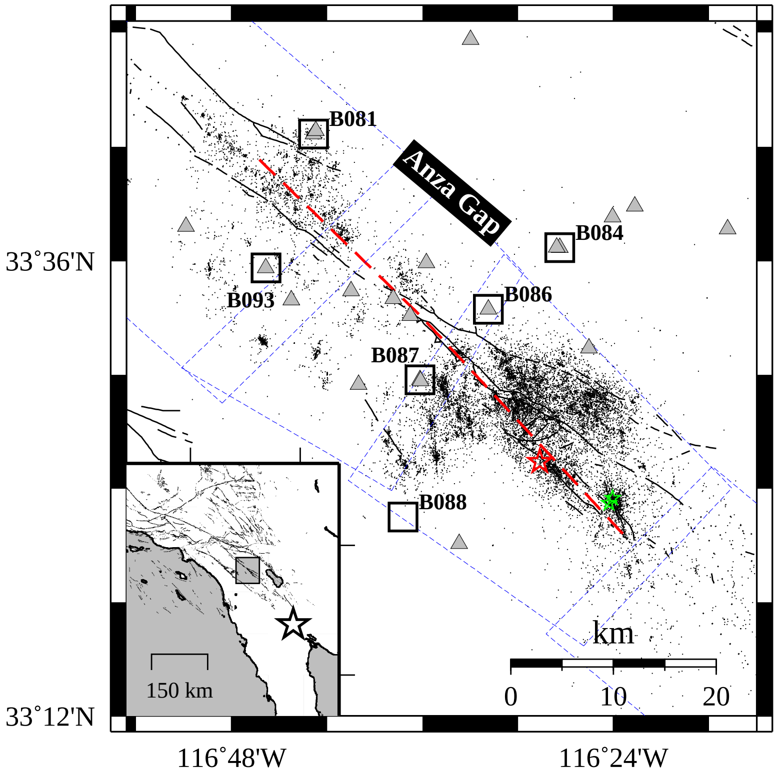

Figure 3.1: Location map. Triangles and squares indicate seismic stations and PBO strain-meters, respectively. Black lines are fault traces and the red dashed line our assumed fault model. Red, green and white stars indicate the locations of the M5.4 Collins Valley mainshock, the two M>4 earthquakes of June 13, 2010, and the M7.2 El Mayor-Cucapah mainshock, respectively. Blue curves outline the polygons considered in the relocation procedure.

divided into three sections, the most active of which is the central section near Anza. Long-term deformation along that section is mainly accommodated by the Clark fault (Figure 3.1), whose geologic slip rate is 10-15 mm/year (Rockwell, Loughman, and Merifield, 1990; Salisbury et al., 2012). Southeast of Anza the main strand of the Clark fault branches into several active faults. The transition is characterized by a 25 km long section almost devoid of seismicity, which is known as the Anza Seismic Gap (Sanders and Kanamori, 1984). It is also marked by the strongest velocity anomaly along the central SJF, expressed by a 5 km wide region of low Vp/Vs ratio that extends to a depth of about 8 km (Allam and Ben-Zion, 2012; Allam, Ben-Zion, et al., 2014), and a well developed, ~ 400 m thick damage zone which is well resolved in seismic datasets (H. Yang et al., 2014; Zigone et al., 2014). Although nine $M > 6$ events occurred along the central SJF in the past 120 years (Sanders and Kanamori, 1984), the Anza Gap has not been ruptured by $M > 7$ earthquakes in over 200 years (Salisbury et al., 2012; Rockwell, Dawson, et al., 2015). With a contemporary slip rate of about 19 mm/year (Lindsey and Fialko, 2013), the 25 km long Anza section is well capable of producing events with $M > 6$ in the near future, thus posing a major threat to nearby communities.

The inter-seismic strain accumulation along the central SJF is characterized by strong fault-normal gradients. To fit such high strain rates, geodetic inversions assuming a dislocation model require the Anza segment to be locked from the surface to a relatively shallow depth of 10.4 ± 1.3 km (Lindsey, Sahakian, et al., 2014). In contrast, the maximum depth of seismicity, which we define as the depth above which 95% of the earthquakes occur, is 16.5 km (Smith-Konter, Sandwell, and P. Shearer, 2011). A possible mechanism that may contribute to the high strain rates observed at the surface, and thus to reconcile the seismic and geodetic observations in Anza, is transient deep fault creep (Wdowinski, 2009). According to this view, the deep transition between fully locked and steady slipping portions of the fault consists of aseismically creeping patches, capable of sustaining transients, interspersed by seismogenic asperities whose dynamic failure results in microseismicity. The topology of the asperities and the heterogeneity of frictional properties within the transition zone account for the statistics of the earthquake catalog. As has been observed in a number of subduction zones (Schwartz and Rokosky, 2007), aseismic release of strain accumulated in the transition zone beneath the SJF could manifest itself by deep intermittent creep events as well as by the occurrence of tectonic tremors. Since the sensitivity of surface deformation to deep slip is small, it is expected that tectonic tremors, if they occur, will provide useful constraints on transient deformation in the transition zone. To date, compelling evidence for the occurrence of tectonic tremors near Anza has not been presented.

Moderate ($M > 5$) events along the Anza segment tend to nucleate at the base of the seismogenic zone, and are accompanied by numerous aftershocks located as far as 50 km from the mainshock. The large, several weeks long increase in seismicity rates at remote sites suggests that physical processes promoting long-range earthquake interactions may be operating along this fault. Felzer and Kilb (2009) studied aftershock sequences triggered by two $M \approx 5$ Anza mainshocks that occurred in 2001 and 2005. They concluded that the distribution of aftershocks density as a function of distance to these mainshocks followed the typical inverse power-law decay observed in southern California, and argued that aseismic slip is not required to explain the spatial extent of seismicity. There are however other observations that point to the possibility of aseismic transients. Meng and Peng (2016) conducted a systematic study of 10 aftershock sequences triggered by $M \approx 4 - 5$ events that occurred between 2001-2013 near Anza. They found that the size of the aftershock zone scales with the mainshock depth and that the aftershock expansion rate is logarithmic, and concluded that aseismic creep at the base of the seismogenic zone is driving deep aftershock expansion in Anza. Several of these events have also caused an increase in local strain rates identified by a long-baseline strain meter installed in the Piñyon Flats Observatory (Agnew and Wyatt, 2005; Agnew, Wyatt, et al., 2013). This observation further suggests that creep and seismicity are indeed spatiotemporally correlated. Similar to the slip transients near the Parkfield and San Juan Bautista sections of the San Andreas Fault (e.g. Linde et al., 1996; Murray and Segall, 2005), the Anza creep transients occur near the edges of a locked fault segment (the Anza Gap). However, unlike the Parkfield segment, where the fault sections adjacent to the locked segment creep at the plate rate near the surface, the segments bordering the Anza Gap do not exhibit shallow fault creep (Lindsey, Sahakian, et al., 2014). This suggests that a considerable fraction of strain accumulated along the deeper portions of the Anza section is potentially released in deep episodic creep events. In this study, we test this hypothesis by performing a joint analysis of strain and seismicity data. Next, we present the geodetic and seismicity data sets, and analyze their spatiotemporal distribution during the 2010 El Mayor-Cucapah, and the 2010 Collins Valley aftershock sequences.

3.3 Data

Strain Data

We analyze continuous strain measurements from 6 out of 8 PBO borehole strain meters located in Anza (Figure 3.1). PBO stations B082 and B089 are omitted due to poor signal-to-noise ratio caused by a nearby water pumping station. The strainmeters consist of four collocated horizontal extensometers, which were installed at depths of 140 to 240 m. The data provided by PBO are down-sampled to a rate of 1 sample per 5 minutes, calibrated, corrected for instrumental noise, and converted to the areal and shear strain components. The transformation matrices from the measurements at each extensometer to the horizontal components of the strain matrix are routinely computed from the predicted tidal response (Hodgkinson et al., 2013).

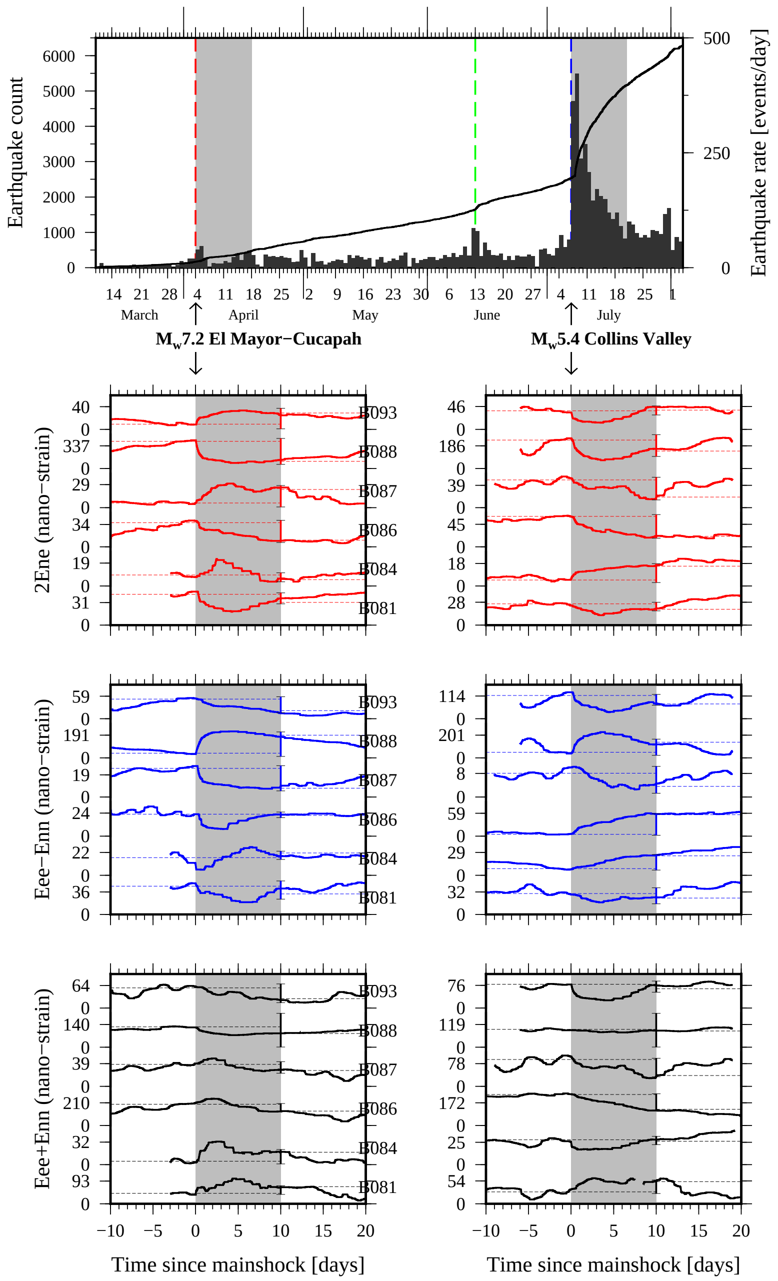

Since the analysis yields only three components of the strain field, the problem is over-determined, and may be solved using measurements at only 3 extensometers. For most of the analyzed time interval data from all four extensometers are available. When only 3 extensometers are operative we convert the raw data to the areal and shear strains using a 3-gauge calibration matrix (K. Hodgkinson, personal communication, 2014). Recently, several studies pointed to potential errors associated with the response of PBO strain-meter instruments. John Langbein (2015) found that the co-seismic response of stations installed near the San Francisco Bay to the

Figure 3.2: Strain data and pre-, co- and post-El Mayor-Cucapah relocated SJF seismicity. Top panel: Cumulative number of events (solid line) and earthquake rate (vertical bars) as a function of time during 2010. Red, green, and blue dashed curves indicate the time of the M7.2 El Mayor-Cucapah, M5.4 Collins Valley, and two M>4 foreshocks, respectively. Grey regions indicate periods of analysis around both mainshocks shown in the rows below. Bottom panels: Left and right columns are for the El Mayor-Cucapah and Collins Valley sequences, respectively. Second, third, and fourth rows show the differential extensional, areal and shear strain components, respectively. Horizontal dashed lines indicate pre- and post-seismically mean strain levels. Vertical bars indicate cumulative post-seismic strains at the end of the analysis periods (grey bands) and their respective uncertainties.

M_w6.4 South Napa earthquake deviates significantly from model predictions. He attributes the discrepancies mainly to the influence of tidal model errors on the strain calibration scheme. As was noted by Hodgkinson et al. (2013), the Anza network is sufficiently removed from the coast so that tidal model errors should exert little influence on the calibration matrices. Barbour, Agnew, and Wyatt (2015) also found poor agreement between observed and predicted co-seismic offsets in Anza PBO strain-meter data during the El Mayor-Cucapah earthquake, and better agreement between the two for the Collins Valley earthquake. These discrepancies were mainly attributed to mechanical shaking induced by seismic waves, and thus should have negligible effect on the post-seismic records we analyze here.

Strain measurements are contaminated by various sources, which include barometric effects, ocean and solid Earth tides, and borehole deformation. The contribution of the latter appears as a linear trend in our records. The signal-to-noise ratio at several epochs is low such that the tectonic signal is obscured by the ambient noise. To recover the tectonic signal, we adopt the approach of Hawthorne and Rubin (2010), and estimate empirical correction terms from time intervals around the period of interest. For each station and for each strain component, the time-series can be approximated by the sum of the tectonic offset and the contribution from borehole deformation, barometric effects, tidal loading, and noise:

$$\epsilon(t) = c_1+c_2t+c_3p(t)+c_4F(t-t_{tra})+\sum_{k}^{17} m_k cos(2\pi t/T_k)+l_k sin(2\pi t/T_k)+c_5H(t-t_{ms})+n(t), \tag{3.1}$$

where p is the recorded barometric pressure, n is measurement noise, and t_{ms} and t_{tra} are mainshock time and the end time of the transient of interest, respectively. The constants m_k and l_k are associated with a tidal signal composed of the following

17 periods (in hours): Q1, 26.8684; O1, 25.8193; NO1, 24.8332; P1, 24.0659; S1, 24.0000; K1, 23.9345; J1, 23.0985; OO1, 22.3061; e2, 13.1272; MU2, 12.8718; N2, 12.6583; M2, 12.4206; L2, 12.1916; S2, 12.0000; K2, 11.9672; et2, 11.7545; M3,8.2804. The fourth term in Equation 3.1 accounts for finite strain accumulated due to post-seismic deformation, which contributes to a total offset, c_4, that we model in the inversion procedure. The transient time function F is such that $F(t) = 0$ if $t < t_{ms}$ and $F(t) = 1$ if $t > t_{tra}$, and has arbitrary shape in the interval $[t_{ms}, t_{tra}]$. The term associated to a step function $H(t)$ represents the co-seismic strain of the mainshock.

We apply the following processing steps to the data from each station and strain component. We first estimate the co-seismic offset, c_5, which appears as a step in the strain records, by removing from the post-seismic strain records the difference between averaged strains in one-hour intervals immediately before and after the mainshock. We then determine t_{tra} by visual inspection, as an interval in which strain rates in most of the stations have returned to pre-mainshock levels. Next, we fit Equation 3.1 to the data in two 10-day-long windows, one before t_{ms} and one after t_{tra}. We finally evaluate the correction terms (i.e. all but the c_4 term) for the entire time period and subtract them from the observations to obtain the processed strain time-series (Figure 3.2). We found that records obtained via this empirical approach contain less noise than the archived PBO processed strain data. Several of the processed strain time-series contain steps and short-term ramps, which result in strains that are comparable to the offset during the transients (e.g. sites B087 and B093 for the El Mayor-Cucapah and Collins Valley episodes, respectively). To minimize the effect of unmodeled noise on the inversion procedure, we use as data for our inversion a cumulated transient strain defined on each channel as the difference between 3-day averages before and after the transient window (dashed lines in Figure 3.2). We adopt an empirical approach for estimating the noise term $n(t)$. We select 100 30-days segments that did not contain any detectable transients. We process these data in the same fashion as for the windows containing the transients, after setting the value of the fitting coefficients c_4 and c_5 equal to zero. We filter the residuals between the observed and modeled strains using with a 3-day median window. For each 30-day segment of smoothed residuals, we compute the difference between all data points separated by 10 days intervals. We use the standard deviation of the distribution of these differences as a measure of uncertainty on the strain data. These values range between a few nano-strain to up to about 50 nano-strain in the noisiest records.

Aftershock Data

Earthquake Rates and Stress Inference

Dieterich (1994) modeled the temporal evolution of seismicity rate of a population of earthquake nucleation patches subjected to an arbitrary stress history in the framework of rate-and-state friction. In this model, aftershocks occur on rate-weakening fault patches that are already accelerating towards failure. The seismicity rate, $\dot{N}$, is related to a state variable of the fault population, γ, proportional to its inter-event time (Segall, Llenos, et al., 2013), by

$$\dot{N} = \frac{\dot{N}_{bg}}{\gamma \dot{\tau}_{tect}}, \tag{3.2}$$

where $\dot{N}_{bg}$ is the background seismicity rate and $\dot{\tau}_{tect}$ is the background tectonic stressing rate. The evolution of the seismicity state variable is related to the stressing history by the following equation:

$$\dot{\gamma} = \frac{1}{a\sigma}(1 - \gamma\dot{\tau}), \tag{3.3}$$

where σ is the effective normal stress (normal stress minus fluid pressure), a is a constitutive parameter quantifying the sensitivity of the fault friction to logarithmic changes of the sliding velocity, and $\dot{\tau}$ is the time-varying Coulomb stressing rate.

Solving Equation 3.3 for a stress history consisting of a stress step, $\Delta\tau$, applied in the middle of a time interval of duration Δt gives (Dieterich, Cayol, and Okubo, 2000):

$$\Delta\tau = a\sigma \ln\left[\frac{\gamma_i + \frac{\Delta t}{2a\sigma}}{\gamma_{i+1} - \frac{\Delta t}{2a\sigma}}\right], \tag{3.4}$$

where γ_i and γ_{i+1} are the values at the beginning and end of the interval, respectively. Values of γ as a function of time are derived using Equation 3.2 from estimates of seismicity rates on cells that contain 10 or more aftershocks. The cells have a size of 1.5 km along-strike, 0.4 km vertically and 6 km in the fault-normal direction. Earthquake rates are assumed to be uniformly distributed within each cell.

Seismicity rates may be computed using either time or data windows. During most of the aftershock sequence, aftershock decay rate is roughly proportional to $1/t$ and therefore rates computed on logarithmic time windows are very sensitive to the duration of the window. Additionally, the time window scheme may suffer from an awkward situation in which a window does not contain any event. To avoid these issues, we adopt the following approach for computing the seismicity rate. We compute the rate for an initial window containing 5 earthquakes. Next, we slide the window by one event and increase the window length by one event. This step is repeated until a pre-defined window length of 10 events is reached, after which the number of events in each window remains constant. The corresponding time of the instantaneous rate measured in the interval $\Delta t = t_2 - t_1$ is (Rubin, 2002):

$$t' = \Delta t / \ln(t_2/t_1). \tag{3.5}$$

By varying the window length we are able to capture slight temporal variations in the seismicity rates early in the aftershock sequence as well as the decay to the background rate late in the sequence. The procedure we use to estimate the uncertainties on the computed rates is presented in Section 3.4.

A principal outcome of *Dieterich's* aftershock model is that the stress change is a logarithmic function of the change in seismicity rate (Equation 3.4). This implies that inferred stresses on seismically active cells are relatively insensitive to the completeness of the seismic catalog (Ziv, 2012). However, a more complete catalog will increase the number of model cells on which stresses can be resolved. We therefore use the catalog of Meng and Peng (2014), who applied a waveform matched filter technique to detect events that were previously unlisted in the Southern California Seismic Network (SCSN) catalog. This newly compiled catalog is complete down to M~0, about 1.5 magnitude units less than the magnitude of completeness of the relocated seismicity catalog of Hauksson, W. Yang, and P M Shearer (2012) for the study area. Meng and Peng (2014) assign the template location to the newly detected events, which, for a dense aftershock sequence, might result in spurious increase of the stresses we infer. To eliminate this bias, we have relocated the newly detected events. Our approach for earthquake relocation is described in Section 3.5.

The incorporation of the more complete, precisely located catalog allows us to compute earthquake rates (and hence stresses) at a large number of sites. Nonetheless, multiple sites contain too few earthquakes to reliably estimate their rate. The distribution of cells with well- and poorly-resolved earthquake rates is presented in Figure 3.3-c,d. Note that here we assume all events are occurring on the SJF plane, while in reality many events occur within the volume surrounding the fault. We account for the three-dimensional distribution of seismicity in the inversion procedure by perturbing the locations of seismically active cells with respect to the SJF fault plane (Section 3.7).

Rates on each cell that contains between 1 and 10 aftershocks (target cell) are estimated from the nearest cells in a 2 kilometer radius in which rates are well resolved (reference cells). For this purpose, we resample the observed rates of reference cells in 1-hour intervals, stack them and scale them by the ratio of number of events in the target cell to the number in the reference cells evaluated at the time of the last event in the target cell. This procedure allows us to asses the evolution of seismicity rates in areas with very few earthquakes. The stress change on cells whose background rates are well resolved (>50 events in the 10 years preceding the El Mayor-Cucapah mainshock, or in the 3 months preceding the Collins Valley mainshock), but do not contain any aftershock is set to zero. The real stress change might be positive or negative in these cells but, but because of their small number and large uncertainties, their overall contribution is small.

The background seismicity rate prior to the El Mayor-Cucapah and the Collins Valley mainshocks are evaluated for events that occurred between 2001 and April 3, 2010 , and between April 14, 2010 and July 6, 2010, respectively. For a small number of cells the background rate prior to the Collins Valley mainshock is not well resolved (Figure 3.3b). These cells are assumed to maintain the level of activity estimated from the 10-year period prior to the El Mayor-Cucapah mainshock. The prior to the El Mayor-Cucapah mainshock are computed using the relocated catalog of Hauksson, W. Yang, and P M Shearer (2012), whose magnitude of completeness is about 0.5 magnitude units larger than the relocated version of Meng and Peng (2014)'s catalog (Section 3.5). To account for missing events we complete the former catalog with the number of events that would have been present if it had the same magnitude of completeness as Meng and Peng (2014)'s catalog, by assuming a Gutenberg-Richter distribution of event sizes with $b = 1$. The spatial distribution of background rates used in Equation 3.2 is obtained from earthquake counts between 2001 and 2010 smoothed using a median filter whose width is 9 and 1.6 km in the horizontal and vertical directions, respectively (Figure 3.3-a). The tectonic stressing rate is obtained from an analytical solution (Segall, 2010) for the stresses induced due to strike-slip motion along an infinitely long vertical fault that is locked between 0-16 km, and which is slipping at rate of 19 mm/year (Lindsey and Fialko, 2013) below this depth.

Our approach for estimating the stresses from observed seismicity rates assumes that the stress history during the time interval Δt is composed of a constant stressing rate, followed by a stress step, followed by a return to a constant (pre-step) stressing

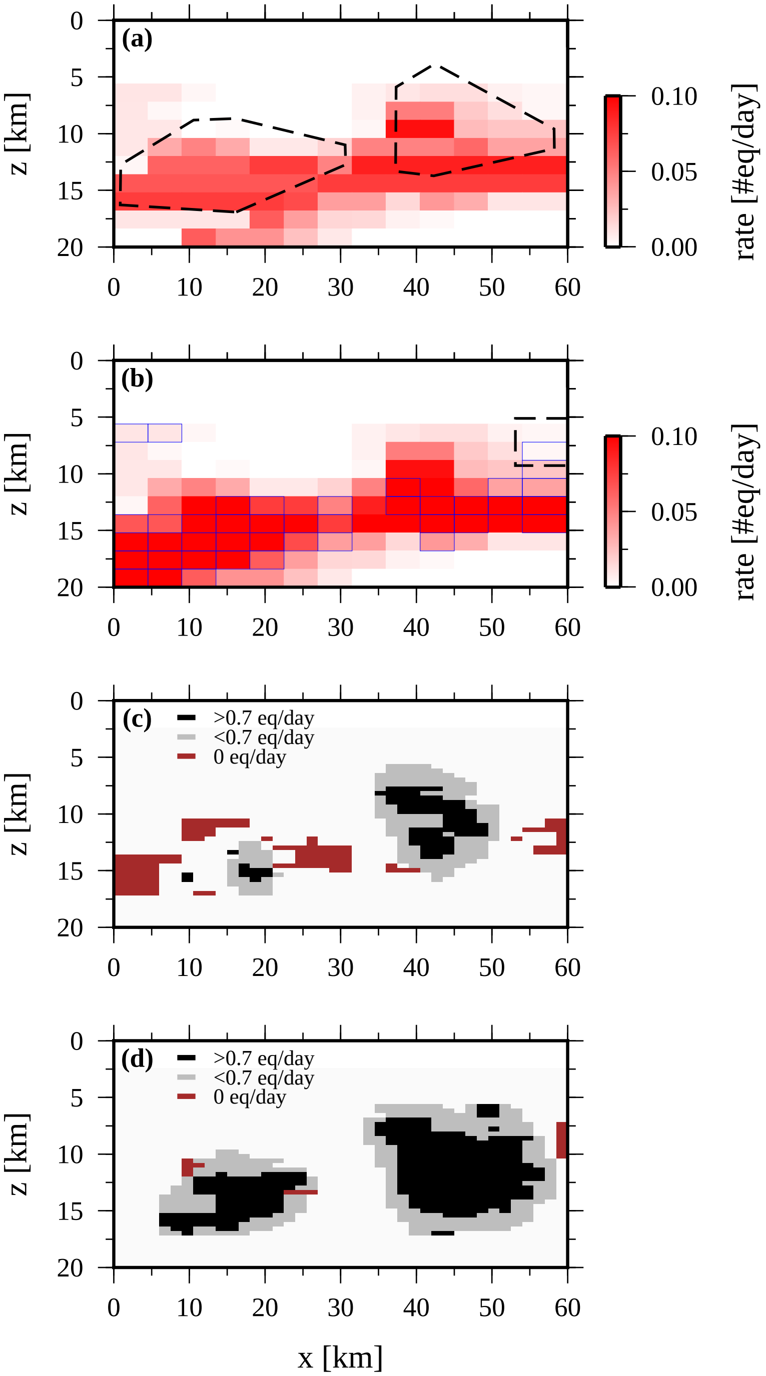

rate. A different approach was taken by Segall, Llenos, et al. (2013), who assumed that during the interval Δt the stressing rate is a liner function of time. Under some conditions, and especially when the stressing rate varies smoothly as a function of time, Segall, Llenos, et al. (2013)'s approach may be more suitable for estimating

Figure 3.3: Background seismicity rate and spatial distribution of model cells for input stress calculation. (a) Background seismicity rate between January 1, 2001 and April 3, 2010, spatially smoothed with a median filter of 9 km horizontal width and 1.6 km vertical width. Dashed polygons indicate areas that contain more than 50 events. (b) Same as panel a but for the time interval preceding the Collins Valley mainshock. Blue rectangles indicate cells that contained more than 2 events occurring between April 14 and July 6, 2010. All other cells have the same background rate as in panel a. (c) Model cells with available background seismicity rates and >10 (black), 1-10 (grey) and 0 (brown) aftershocks in the 10-day period following the El Mayor-Cucapah mainshock. (d) Same as panel c for the Collins Valley aftershocks.

stresses. Both approaches, however, should provide similar estimates if the duration of Δt is sufficiently small compared to T_γ, the typical time scale of fluctuations of the seismicity state parameter γ:

$$T_\gamma \approx \gamma/\dot{\gamma}. \tag{3.6}$$

We can approximate γ and $\dot{\gamma}$ as:

$$\gamma \approx (\gamma_i + \gamma_{i-1})/2, \tag{3.7}$$

and

$$\dot{\gamma} \approx (\gamma_i - \gamma_{i-1})/\Delta t. \tag{3.8}$$

Thus, the requirement $\Delta t << T_\gamma$ leads to the following practical condition:

$$|\gamma_i - \gamma_{i-1}| << (\gamma_i + \gamma_{i-1})/2. \tag{3.9}$$

We find that the condition in Equation 3.9 is met 95% of the times. As the stress changes in the remaining 5% of the times generally do not exceed 10-20% of the maximum inferred stresses, we consider that Δt to be sufficiently small such that it reasonably captures fluctuations in γ.

3.4 The Error of Inferred Stresses

Uncertainties in aftershock rates (and hence inferred stresses) may be result from several factors. One source of bias may be mis-located aftershocks contaminating the event counts within seismic cells. The location uncertainties can be separated into absolute and relative error. We account for absolute location uncertainty by coupling the least-squares algorithm with a Monte Carlo scheme in which the locations of seismic cells containing aftershocks are perturbed before each inversion.

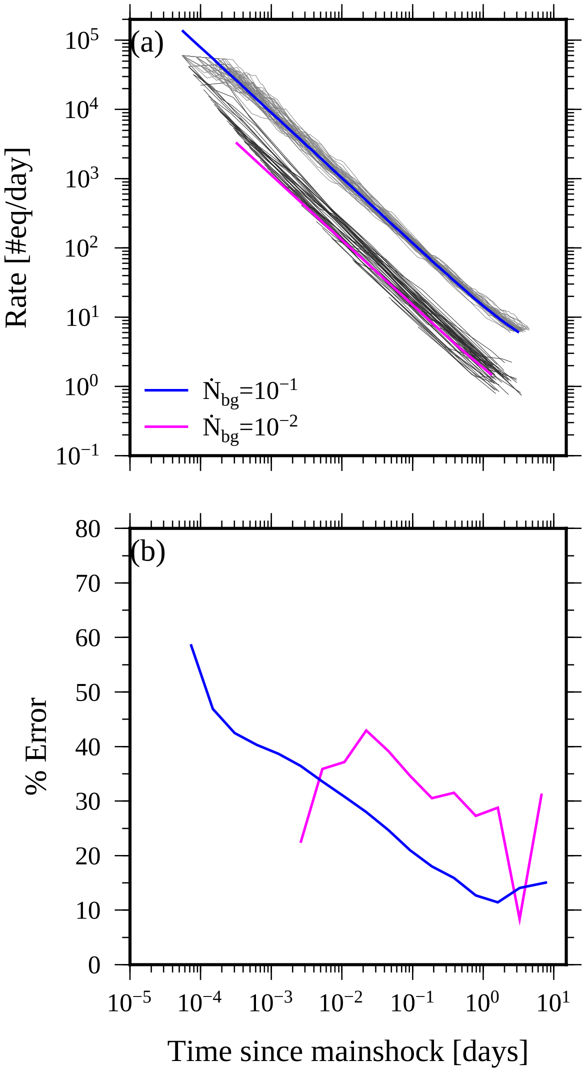

Figure 3.4: Stress errors from synthetic tests. (a) Earthquake rate as a function of time since the mainshock. Grey curves are for synthetic catalogs whose inter-event times are drawn from a non-stationary Poissonian distribution with prescribed stress history. Blue and magenta curves are for the expected rates computed with $\dot{N}_{bg} = 10^{-1}$ and $\dot{N}_{bg} = 10^{-2}$ earthquakes/day, respectively, and with $\dot{N}/\dot{N}_{bg} = 10^{6}$, and $a = 10^{-3}$. (b) Stress error computed as the mean difference between stresses inferred from synthetic catalogs and the actual stresses, normalized by the latter. Colored curves correspond to the rates in panel a.

The relative location uncertainty is smaller than the dimension of the cells and, since the inferred stresses are assumed to be representative of the stress in the mid-cell position, shuffling event locations within a given cell would not change the estimated stresses.

Two other sources of bias arise from our aftershock counting procedure. The first is the possible inclusion of secondary aftershocks, which are the result of earthquake interactions that are not accounted for in *Dieterich's* model. We show in Section 3.10 that the effect of these secondary aftershocks on the output slip distribution is small. A second source of bias is related to the number of events used to evaluate seismicity rates in each time window. Our rate estimation scheme is based initially on only 5 aftershocks, and later on up to 10 aftershocks. Our objective in this section is to estimate the error on rates computed with this technique. We propagate the error on rates in our stress computations (Equations 3.2 and 3.4) to obtain uncertainties on the inferred stress used in our inversion (Section 3.7).

We model aftershocks as non-stationary Poissonian processes with time-dependent rate $\lambda(t)$. As a transient scenario we consider an initial constant stressing rate, $\dot{\tau}_{tect}$, followed by a stress step $\Delta\tau$, and then by a different constant loading rate, $\dot{\tau}$. The resulting evolution of seismicity rate in the rate-and-state model is (Dieterich, 1994):

$$\lambda(t) = \frac{\dot{N}_{bg}\dot{\tau}/\dot{\tau}_{tect}}{\left[\frac{\dot{\tau}}{\dot{\tau}_{tect}}\exp\left(\frac{-\Delta\tau}{a\sigma}\right) - 1\right]\exp\left(\frac{-t}{t_a}\right) + 1}, \tag{3.10}$$

where t_a is the characteristic duration of the aftershock sequence, which is close to 10 days for the Anza sequences. The ratio $\dot{\tau}/\dot{\tau}_{tect}$ is set to 10. The constant $\Delta\tau$ is defined as change in stress associated with a instantaneous change in seismicity rate (Ziv, 2012):

$$\Delta\tau = a\sigma \ln\left(\frac{\dot{N}}{\dot{N}_{bg}}\right), \tag{3.11}$$

where $\dot{N}$ and $\dot{N}_{bg}$ represent the seismicity rate immediately before and immediately after the stress step, respectively, a is a constitutive parameter, and σ is the effective normal stress. We construct synthetic catalogs by simulating a non-stationary Poisson process with this prescribed rate (Figure 3.4a). To asses the sensitivity of the computed rates to the number of events in the simulated catalogs, we vary the value of $\dot{N}_{bg}$ in the range between 0.01-1 earthquakes/day similar to the observed background rates in the Anza catalog (Figure 3.3). Our estimate of the ratio $\dot{N}/\dot{N}_{bg}$ is taken as the median value of the observed rate in each cell, and the value of a

spans the range $1 \times 10^{-6} - 1 \times 10^{-1}$ used in the inversion procedure. We estimate stress time-histories from the rates of each simulated sequence, following the same procedure as for the real data, and compare it to the exact stresses obtained via Equation 3.11.

Figure 3.4b presents the average stress error as a function of time since the mainshock using 100 simulated catalogs. We find that uncertainties on stresses associated with our rate estimations are highly time-dependent, and are highest early in the aftershock sequence when the number of events in the rate-estimation window is smallest. The stress error increases to up to about 12-15% of the cumulative stresses near the end of the period of analysis (10 days).

The analysis presented in Section 3.6 suggests that the response at the NW cluster was delayed by about one day, which is approximately the time it takes for the propagating creep front to arrive near that area. To mimic this behavior, we conducted the same statistical analysis on synthetic catalogs in which the mainshock time is delayed by one day. We found that delaying the mainshock time had little effect on the errors presented in Figure 3.4b.

3.5 Earthquake Relocation

We use seismic data recorded by local SCSN and PBO stations in Anza (Figure 3.1). Our relocation approach follows the method of Got et al. (2002) . We divide the study area into polygons that delimit the SJF trace but do not cut through dense clusters of seismicity. The polygons overlap to allow for earthquake clusters to extend beyond a boundary. In each polygon, for each event pair and for each channel, we compute the waveform coherency in the 1-12 Hz frequency band for 2.56 s long windows centered on the P- and S-wave arrivals. Whenever phase data are not available (about 97% of the events), we compute theoretical travel times using a 1-D local velocity model (E. Hauksson, personal communication, 2014) and run an automatic picking algorithm to determine the arrival times (P. M. Shearer, Prieto, and Hauksson, 2006). We visually reviewed the picks for many waveforms to ensure that the P- and S-wave trains are contained within the time-window used for cross-correlation. Time-delays are derived from the slope of the best linear fit (in the least-squares sense) to the cross-phase spectrum of the shifted waveforms. This method generally yields time-delay estimates with sub-sample precision. Once the polygon's coherency matrix is obtained, the events are grouped into clusters. We use a k-means clustering algorithm (Press et al., 1992) with a coherency threshold of 0.8. These clusters contain from 10 to a few hundred events, and span up to a few hundred meters.

Event relocation is performed using an iterative procedure, which weights the input in each iteration according to its deviation from the median delay-time residuals. An implicit assumption in relocation techniques is that within each cluster, the inter-event distances are much smaller than the average distance to the receiver. In order for this assumption to remain valid, the relocation is done sequentially. We start with clusters that contain up to 40 events, and add an event to that cluster if its average coherency with the other members in the cluster exceeds 0.7. We then relocate the new cluster while considering delay times for pairs whose coherency is larger than 0.8. Our resulting catalog contains 7079 events divided into clusters whose dimensions are up to a few hundred meters.

3.6 Space-time Analysis of the $M_w 7.2$ El Mayor-Cucapah, and the $M_w 5.4$ Collins Valley Earthquake Sequences and Recorded Strain

In this section we analyse the seismicity and strain during each of the aftershock sequences, and show that the observations support the hypothesis that these phenomena are correlated both in space and in time. Our relocated version of Meng and Peng (2014)'s catalog (Section 3.5) allows us to study the response of the fault to perturbations from the local and remote mainshocks at fine temporal and spatial scales. To do that, we compare the space-time evolution of seismicity immediately following the El Mayor-Cucapah and the Collins Valley earthquakes in Figure 3.5 and 3.6. The temporal evolution on a longer time-scale is presented in Figure 3.2.

Seismicity is mainly concentrated along two segments located to the southeast and northwest of the Anza Gap. The gap itself is clearly visible in Figures 3.5 and 3.6 as an area mostly devoid of seismicity that extends between 25 and 40 km along fault strike. We refer to the two active segments that extend between 0-30 km and 30-60 km as the NW and SE clusters, respectively. We identify migration of seismicity along fault strike during the El Mayor-Cucapah and Collins Valley mainshock. The spatio-temporal distribution of the Collins Valley aftershocks indicates that their migration speed is inversely proportional to time since the mainshock. The small number of events and the short spatial scale prevents us form determining the rate at which the El Mayor-Cucapah aftershocks migrate along the SJF strike. We added a line indicating a logarithmic migration trend to Figure 3.6. Similar rapid initial expansion of the aftershock zone during the Collins Valley sequence, as well as

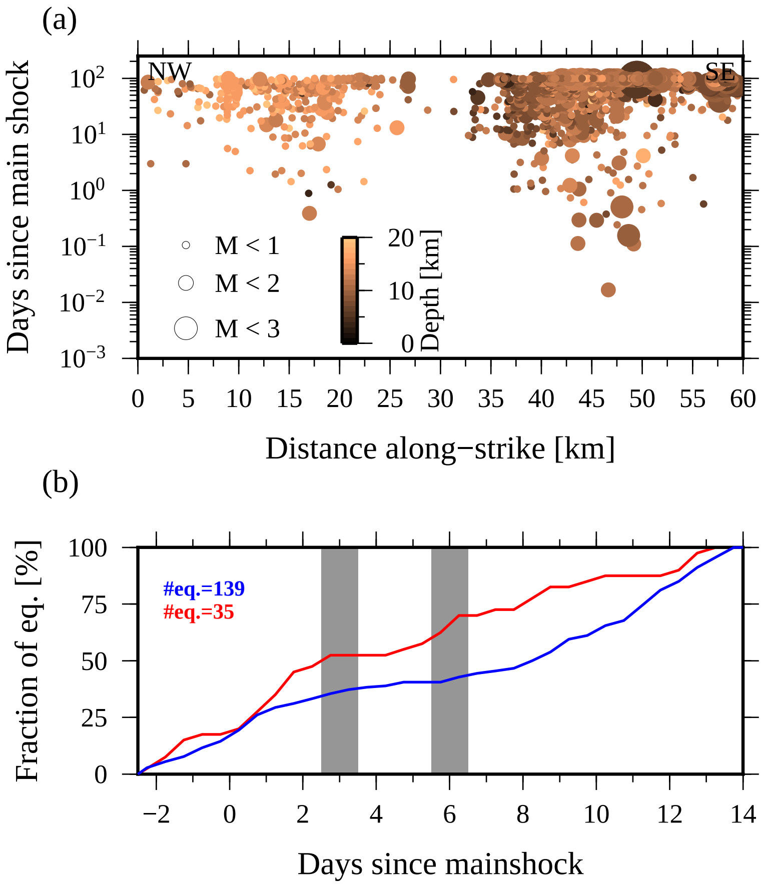

Figure 3.5: Space-time seismicity diagrams for the El Mayor-Cucapah sequence. (a) Aftershock locations projected along fault strike as a function of time since the mainshock. The symbol color and size indicate depth and magnitude, respectively. (b) Cumulative event count as a function of time since the El Mayor-Cucapah earthquake in the NW (red) and SE (blue) clusters, defined as segments spanning locations 0-30 km and >30 km along-strike in panel a, respectively. Grey bands indicate intervals of rapid strain rate changes identified in the strain-meter data (Figure 3.7).

during sequences triggered by several other moderate Anza mainshocks was also observed by Meng and Peng (2016). Of the events recorded by the Anza strain network, only the El Mayor-Cucapah and the Collins Valley earthquakes generated strong, coherent signals at the borehole strain-meters, which allowed us to perform the comprehensive analysis presented in this chapter.

We compare the cumulative number of aftershocks in the SE and NW clusters as a function of time since the mainshocks (Figures 3.5b and 3.6b). This analysis allows us to identify abrupt changes in seismicity rates, which we will later relate to the

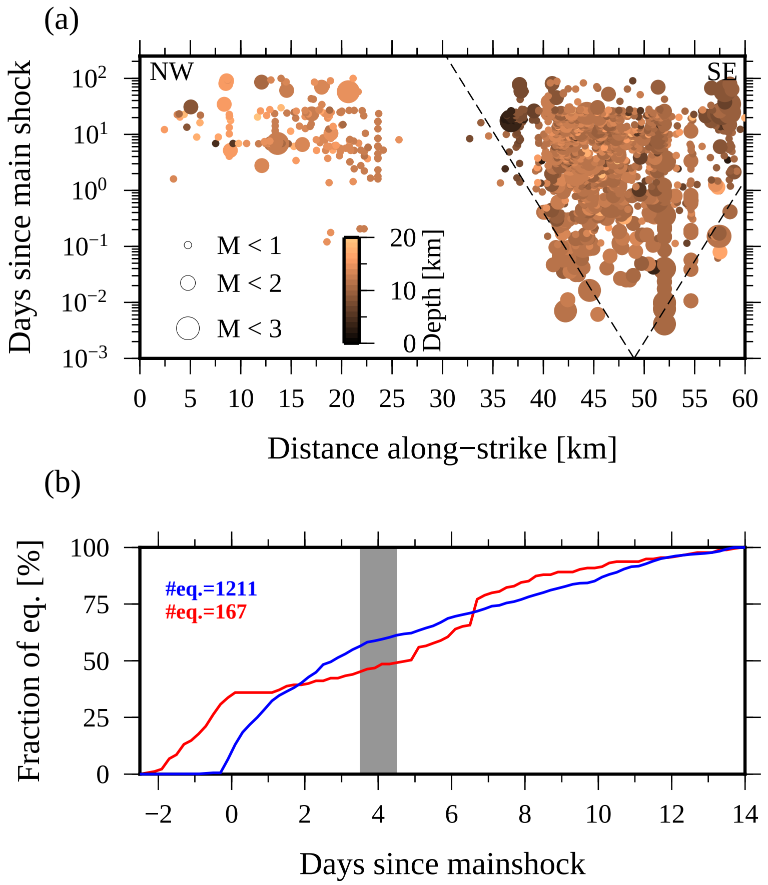

Figure 3.6: Space-time seismicity diagrams for the Collins Valley sequence. Dashed curve indicates migration velocity that decays as $1/t$, where t is time since the mainshock. See the caption of the previous figure for details.

observed strain rates. The instantaneous response of seismicity in the SE cluster to the local (Collins Valley) and remote (El Mayor-Cucapah) stress perturbation is similar. In both cases cumulative event numbers exhibit approximately a logarithmic dependence on time since the mainshock, indicative of an Omori type aftershock sequence. However, while the Collins Valley aftershocks in the SE cluster continue for about 2 weeks, the El Mayor-Cucapah aftershocks in that cluster take only 3-4 days to decay. Th post-El Mayor-Cucapah rate increase is followed by a short quiescence and then by an increase on the 6-th day to a new rate that is comparable or higher than the pre-mainshock seismicity rate. Anomalously high seismicity rates in Anza persist for several months leading to the Collins Valley mainshock (Figure 3.2). We present a detailed spatiotemporal analysis of seismicity leading to the Collins Valley earthquake in Section 3.9.

The immediate effect of the Collins Valley mainshock is to reduce the seismicity rates in the NW cluster. The rate increases about 4 days after the mainshock, and then decays logarithmically with time for the remaining two weeks. The temporal evolution of El Mayor-Cucapah aftershocks in the NW cluster differs significantly: their rate accelerates immediately following the mainshock, then undergoes a few days of quiescence, and accelerates again about 6 days after the mainshock. This behavior is similar to the activity in the SE cluster during the El Mayor-Cucapah sequence. We note that the magnitude of events in the NW cluster during the quiescence periods does not exceed $M = 1.5$. This observation, together with high strain rates observed at the surface, suggests that loading due to nearby fault creep is the likely cause for the rate increase in the NW cluster 6 and 4 days after the El Mayor-Cucapah and Collins Valley earthquakes, respectively. Quiescence in nearby areas is most likely the result of stress unloading at the tail of the passing creep front. The lack of a strong mainshock and the increase in strain rates presented below suggest that the increase in seismicity rates after the quiescence is due to additional loading from creep occurring later in that sequence.

The difference in the time-dependent strain release during the El Mayor-Cucapah and the Collins Valley sequences is also apparent in the strain time-series data, which is, at least qualitatively, temporally correlated with seismicity. To identify coherent strain signals across the network we compute, for each data point, the direction and size of principal strain axes after removal of non-tectonic signals and co-seismic offsets using the approach outlined in Section 3.3. The processed strain data are filtered using a 5-hour median window to remove unmodeled steps in the strain time-series. We estimate the uncertainties on these measurements from synthetic simulations, in which, for each simulation, we perturb each data point of the three strain channels. The magnitude of the perturbation is randomly drawn from a normal distribution whose variance is equal to the variance of the noise in the strain time-series data (see Section 3.3). We perform 500 tests, and find that the uncertainty on the principal strain directions and magnitudes is approximately 5%.

Figures 3.7c and 3.7d present the second-invariant of the strain tensor relative to the pre-event strain field as a function of time since the El Mayor-Cucapah and Collins Valley earthquakes, respectively. We identify coherent changes in strain magnitudes across the Anza strain-meter network 3 and 6 days following the El Mayor-Cucapah mainshock. The strain-rate increase on the third day is correlated with a reduction of seismic activity in the NW cluster, and the one on the sixth day

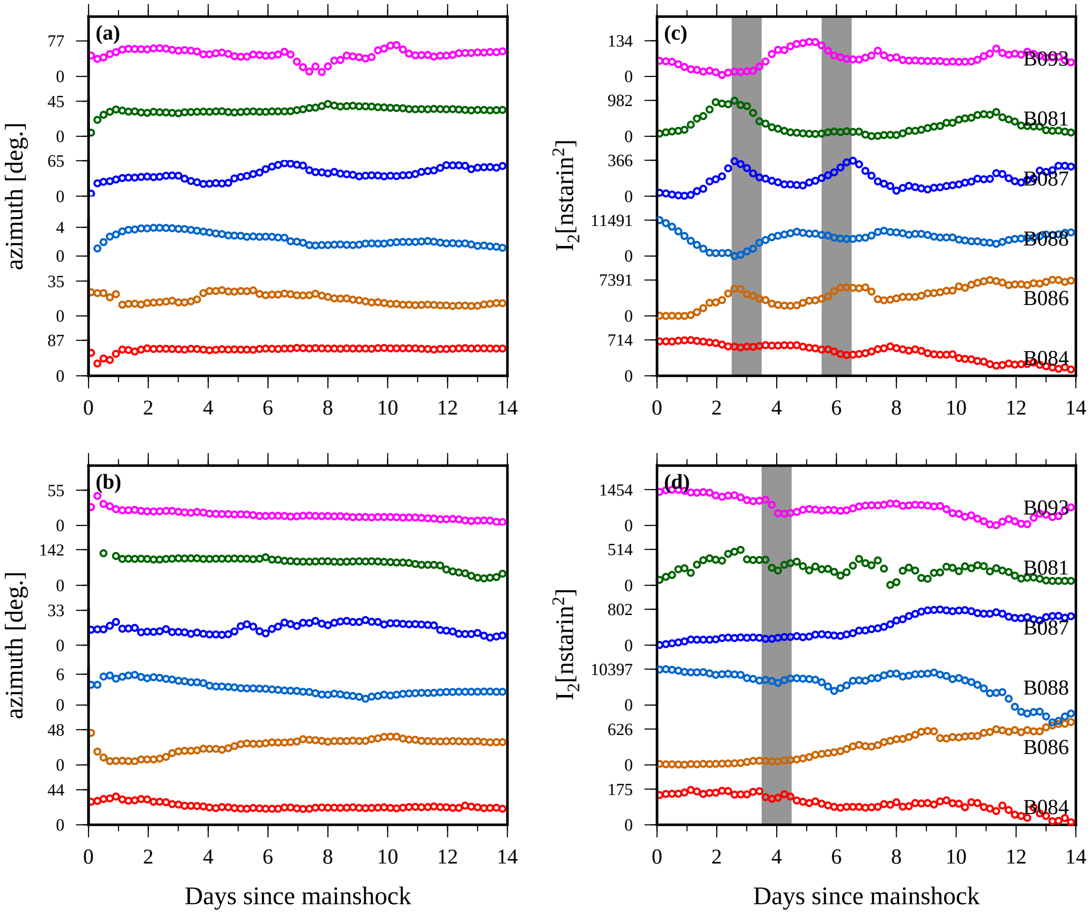

Figure 3.7: Temporal evolution of principal strains. Top and bottom rows are for the El Mayor-Cucapah and Collins Valley sequences, respectively. (a)-(b) Azimuth of the largest principal strain direction as a function of time since the mainshock. (c)-(d) Second invariant of the strain tensor as a function of time since the mainshock. Station names are indicated in the rightmost column. Vertica grey bands indicate abrupt strain rate changes at periods corresponding to seismicity rate changes (Figure 3.5b and 3.6b).

is correlated with seismicity rate increase in both the SE and NW clusters (Figure 3.5b). In contrast, strain build up following the Collins Valley sequence is gradual, and accelerates somewhat about 4 days into the sequence. The gradual increase in strain magnitude early in the Collins Valley sequence is in agreement with the slow initiation of aftershock activity in the NW cluster, and the timing of strain acceleration slightly precedes the seismicity rate increase in that cluster about 4 days after the mainshocks.

Similar to aftershock migration, triggered creep is also observed to propagate along fault strike. We obtain direct evidence of slip propagation by examining the temporal dependence of principal strain directions during each of the transients. The azimuth of the largest principal strain direction as a function of time is presented in Figures 3.7a and 3.7b. Migrating slip causes strain rotations that vary between 10 and 40°, depending on the location of the station relative to the propagating creep front. In the first day following the mainshocks several stations exhibit rapid changes in the principal strain orientations (e.g. stations B088, B081, B093 and stations B086, B088, B093 during the El Mayor-Cucapah and the Collins Valley sequences, respectively). This pattern is also apparent in the fast migration of early (first-day) aftershocks during these sequences (Figure and 3.5a 3.6a), suggesting that afterslip and aftershocks are migrating together along the SJF strike.

The response at the two most north-western stations (B081 and B093) is most interesting. These stations record principal strain direction rotations immediately following the El Mayor-Cucapah and Collins Valley earthquakes. During both sequences, rapid rotations of up to 40° relative to the pre-event principal strain directions occur over a period of about a day. The sense of rotations during each of the episodes at stations B081 and B093 is equal. However, the principal strain directions at the two stations rotate in a clockwise and anti-clockwise directions during the El Mayor-Cucapah and the Collins Valley sequence, respectively. If creep during the El Mayor-Cucapah sequence is migrating along the SJF strike as seismicity does (Figure 3.5a), one would expect the principal strain axes at sites B093 and B081 to rotate clockwise. By comparing the rotations to results of synthetic tests, we find that the sense of rotation at site B093 during the El Mayor-Cucapah sequence is consistent with a slip front propagating unilaterally from the SE towards the NW below the site, similar to the trend observed in the migration of seismicity presented in Figure 3.5a.

The qualitative analysis of seismicity and strain suggests that the observations are correlated to within one day, which is near the limit of the temporal resolution of these data sets. We are interested in inferring the cumulative slip distribution that gives rise to deep seismicity and surface strain, and thus proceed by jointly inverting the two data sets using the scheme presented in the next section. This analysis allows us to test the hypothesis that static stress transfer from fault patches slipping aseismically triggers seismicity along the SJF.

3.7 The Inversion Scheme

We model the seismicity and the strain variations following the El Mayor-Cucapah and the Collins Valley earthquakes assuming that they were driven by aseismic slip on the SJF. The observed strains and inferred stresses are therefore jointly inverted to recover the best-fitting distribution of slip. At this stage we are focusing on the slip accumulated during each transient, and thus only try to fit the measured cumulated strains (Figure 3.10) and the cumulated stress changes derived from the seismicity (Figure 3.11a and 3.11d). Here we try to explain these observations as a result of aseismic slip on the SJF. In reality, the stresses we infer also contain the static co-seismic stress change due to the mainshock. Note that the co-seismic strain change was removed from the strain data. Because of the rapid decay of stress with distance away from the mainshock, our approach may bias the stresses we infer for the Collins Valley sequence on cells located near the hypocenter. However, as we show below, the peak slip we infer from the joint data set is over 1 meter, much larger than the expected co-seismic slip during the $M_w 5.4$ Collins Valley mainshock. We therefore ignore the contribution of co-seismic stress change, and attribute the inferred stresses to post-seismic slip.

The inversion procedure is set up to minimize the following cost function:

$$C = C_1 + \beta^2 C_2 = ||W(Au - d)||^2 + \beta^2 ||S\Delta u||^2, \tag{3.12}$$

where $||\cdot||$ denotes the L_2 norm of a vector. The term C_1 is a joint misfit function, in which d is a vector containing the observed strains and inferred stresses at the end of the transient, u is the solution vector comprising the slip distribution at the end of the transient, A is a model matrix relating model parameters to data, and W is a diagonal matrix of weights given to each data set. The term C_2 is a regularization term introduced to stabilize the inversion by imposing spatial smoothness on the slip distribution. S a smoothing matrix, Δ is the Laplacian operator, and β is a smoothness coefficient that controls the importance of the regularization term.

The weights are computed according to the errors of each data set:

$$W_i = 1/s_i, \tag{3.13}$$

where s_i are the standard deviation of the strain residuals (Section 3.3) and of the estimated error on the inferred stresses (Appendix A). The stress errors range between 10% and 20% of the inferred stress.

We define the matrix A as follows:

$$A = \left(\begin{array}{c} G_{ij} \end{array} \right), \tag{3.14}$$

for the strain only inversion, and

$$A = \begin{pmatrix} G_{ij} \\ \alpha_\beta K_{kj} \end{pmatrix}, \tag{3.15}$$

for the joint inversion. G_{ij} and K_{kj} are elastic kernels (Okada, 1992), which relate strain at location i, ϵ_i, and stress change at location k, $\Delta\tau_k$, to unit slip at location j, u_j. Slip is constrained to be right-lateral and positive, and is tapered by overweighting the Laplacian on the edges relative to cells in the interior of the model. Model cells measure 1.5 and 0.4 km in the along-strike and along-depth directions, respectively.

Inherent differences in the sensitivity of the geodetic and aftershock data to fault slip are to be taken into account in order to obtain a realistic slip distribution satisfying both data sets. While the geodetic data are most sensitive to the long-wavelength component of slip, the aftershock data are most sensitive to a local, short wavelength slip variation, probably of similar scale as the aftershock clusters. To account for these differences, it is useful to weigh the model smoothness according to the resolution power of the joint data set. We down-weight poorly resolved areas in the model by defining the matrix S as:

$$S = \frac{diag(A^t A)}{max(A^t A)}. \tag{3.16}$$

Applying these weights to the smoothing operator adjusts the correlation length between cells according to the resolution power of the data, thus providing compact slip distributions in well-resolved areas and vice versa (Ortega-Culaciati, 2013).

The constant α_β is introduced to account for the length difference between the data vectors ϵ_i and $\Delta\tau_k$, and its value is chosen such that we obtain equal misfits to the strain and stress data. For each value of β, we find the corresponding α_β by 1-D line minimization (Press et al., 1992) of the cost function with the constrain that the difference between the weighted misfits to each dataset are smaller than 1% of the average of the misfit to each data set. We found that after a few iterations the differences between the normalized misfits match our predefined threshold.

Seismicity southeast of the Anza seismic gap is distributed over several fault branches that compose a complex fault zone, where multiple active secondary faults are located within some distance from the main fault strand. We model stress transfer to these secondary faults by assuming that slip on the main fault triggers seismicity at sites located off the fault's surface. The stresses on off-fault patches are computed according to Equation 3.4, and are related to slip as in Equation 3.15. The stress history obtained from solving Equation 3.4 is taken to be the representative value for stress at the mid-cell location. To account for a non-negligible change in normal stress at off-fault sites, we use the inferred changes in Coulomb stress $\Delta CFF = \Delta\tau - f\Delta\sigma$ as input. The static friction coefficient, f, is assumed constant and its value is set to 0.6. We incorporate the uncertainties associated with the absolute location of events in the catalog by coupling the least-squares algorithm with a Monte-Carlo scheme, such that in each iteration we perturb the distances between the seismic cells and the fault plane. The perturbed distances are drawn from a normal distribution whose variance is equal to 2 km, similar to the actual spatial scatter around the assumed fault plane. To reduce the number of unknowns in the problem we assume that the orientation of each sub-fault is identical to that of its nearest cell of the main fault plane. This assumption is consistent with the observation of a rather homogeneous distribution of focal mechanisms along the Anza section of the SJF (Bailey et al., 2010).

Equation 3.12 is solved using the least-squares algorithm with positivity constraints of Lawson and Hanson (1974). We assume Poisson's ratio and Young's modulus equal to 0.25 and 30 GPa, respectively. The value of the constitutive parameter a is assumed to be spatially uniform. A flowchart of the joint inversion and pre-processing is presented in Appendix A.

3.8 Results: Slip distribution and Static Stress Transfer to Seismic Cells

I apply the inversion procedure outlined in Section 3.7 to strain and aftershock data from the 2010 El Mayor-Cucapah and Collins Valley mainshocks. Figures 3.8a and 3.8b present, for each value of the smoothness coefficient β, the norm of smoothed slip distribution scaled by the value of β as function of the norm of the residuals. The decrease in the norm of the residual with an increase in the roughness of the model (smaller values of β) is a well-known attribute of geophysical inversions and represents a trade-off between model resolution and variance. We adopt a conventional L-curve approach to choose a model that is sufficiently rough without over-fitting the data: I select the β value corresponding to the inflection point of the solid blue curve in Figure 3.8a and 3.8b.

A central assumption in our inversions is that static stresses due to aseismic slip on a main fault strand are transferred to secondary seismically active faults. Under this assumption we obtain a satisfactory fit to the strain and aftershock data. In Section 3.13, we test an alternative mode of stress transfer in which seismicity

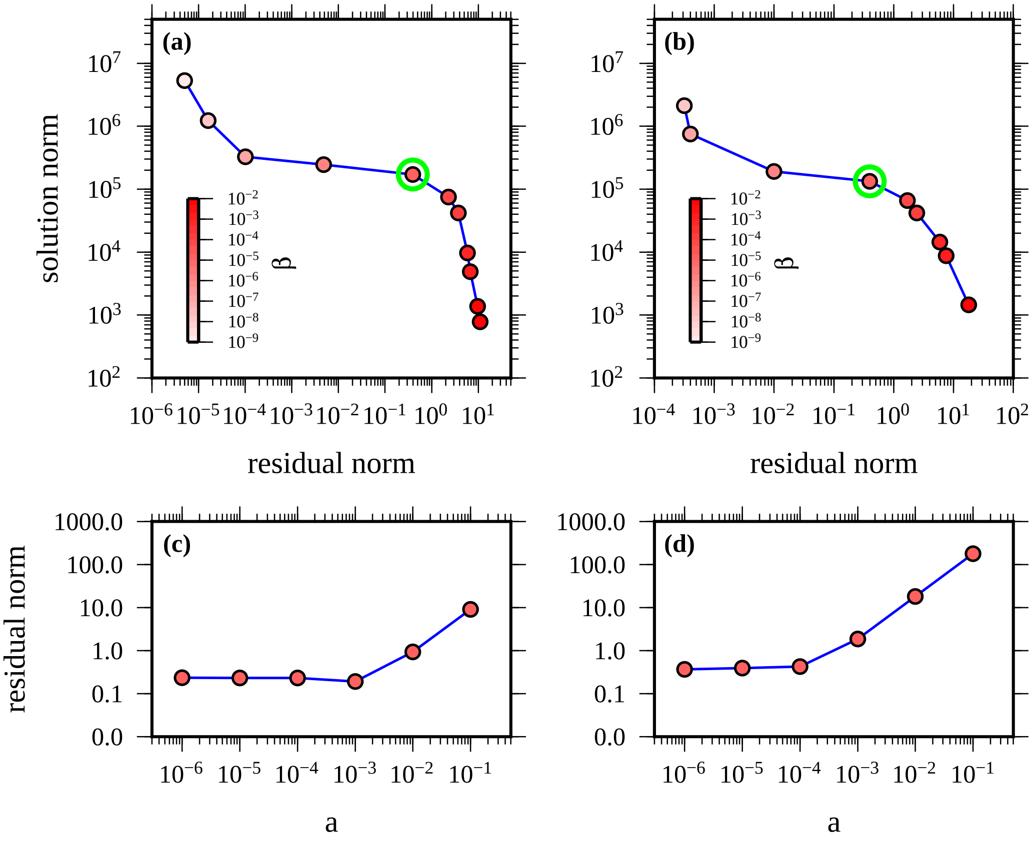

Figure 3.8: Top row: The square root of the regularization term C_2 as a function of the square root of the joint misfit C_1. Bottom row: Square root of C_1 as a function of the constitutive parameter a. The color scale indicates the value of the smoothing coefficient β. Left (a, c): El Mayor-Cucapah. Right (b, d): Collins Valley. Green circles indicate the preferred solutions.

occurs on asperities embedded in the main fault, driven by stresses imposed by creep in the surrounding fault regions. This assumption is common in models of repeating earthquake sequences (e.g Chen and Lapusta, 2009). We find that this model provides a significantly poorer fit to the joint dataset.

Figure 3.9 presents the slip distributions of our preferred models of afterslip triggered by the El Mayor-Cucapah and Collins Valley mainshocks. The observed and modeled strains and stresses are shown in Figures 3.10 and 3.11, respectively. Figure 3.10 also presents the computed GPS displacements at several sites in Anza for the slip distributions in Figure 3.9. For most sites the predicted displacements do not exceed 5 mm, a value comparable to the uncertainty of GPS data. Because the sensitivity of the GPS network to deep (> 5 km) fault slip is small we do not expect

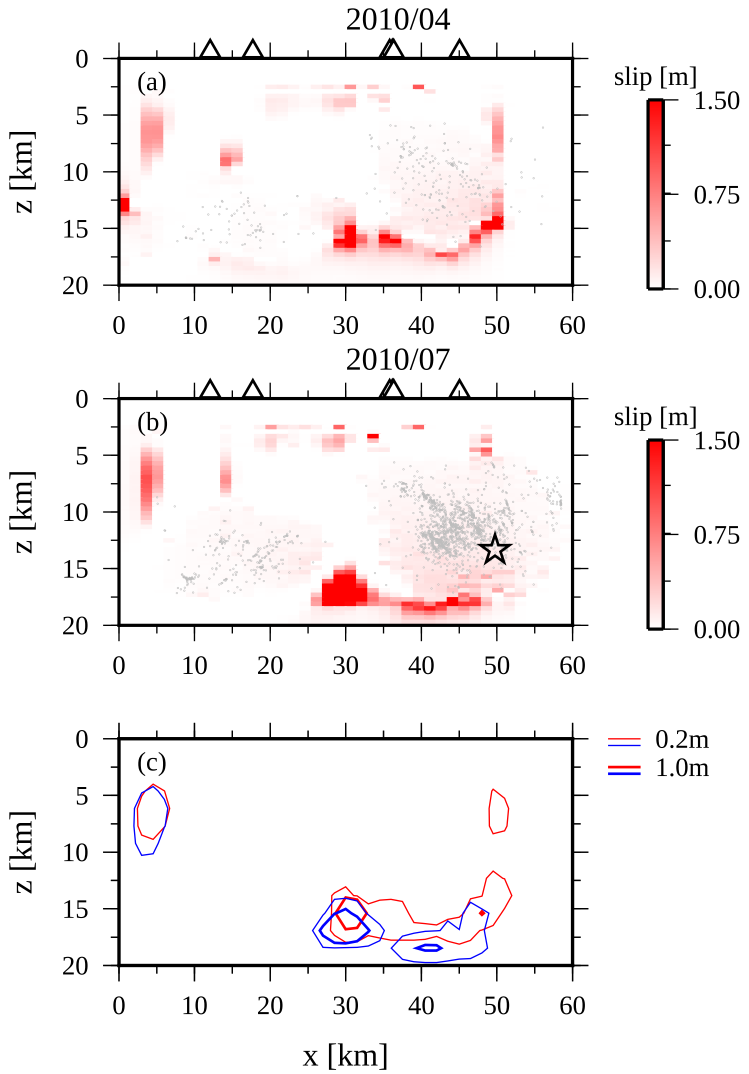

Figure 3.9: Inferred afterslip distributions. (a) El Mayor-Cucapah. (b) Collins Valley. Triangles indicate along-strike location of PBO strain-meters. Star indicates location of the Collins Valley mainshock. Grey circles indcate the location of aftershocks projected onto the SJF strand. (c) Slip contours of afterslip triggered by the El Mayor-Cucapah (red) and Collins Valley (blue) mainshocks.

the GPS instruments to detect the deep slip imaged via our joint inversion approach.

The moment magnitude of afterslip in a 10 day interval is 6.2 and 5.9 for the El Mayor-Cucapah and Collins Valley sequences, respectively. To estimate the robustness of this result we have conducted synthetic tests in which we invert only the strain data for slip in scenarios with uniformly distributed slip around the Collins Valley mainshock with moment magnitude 6.2. We found that the strain-only inversion recovered the input moment but, as expected, was not able to recover

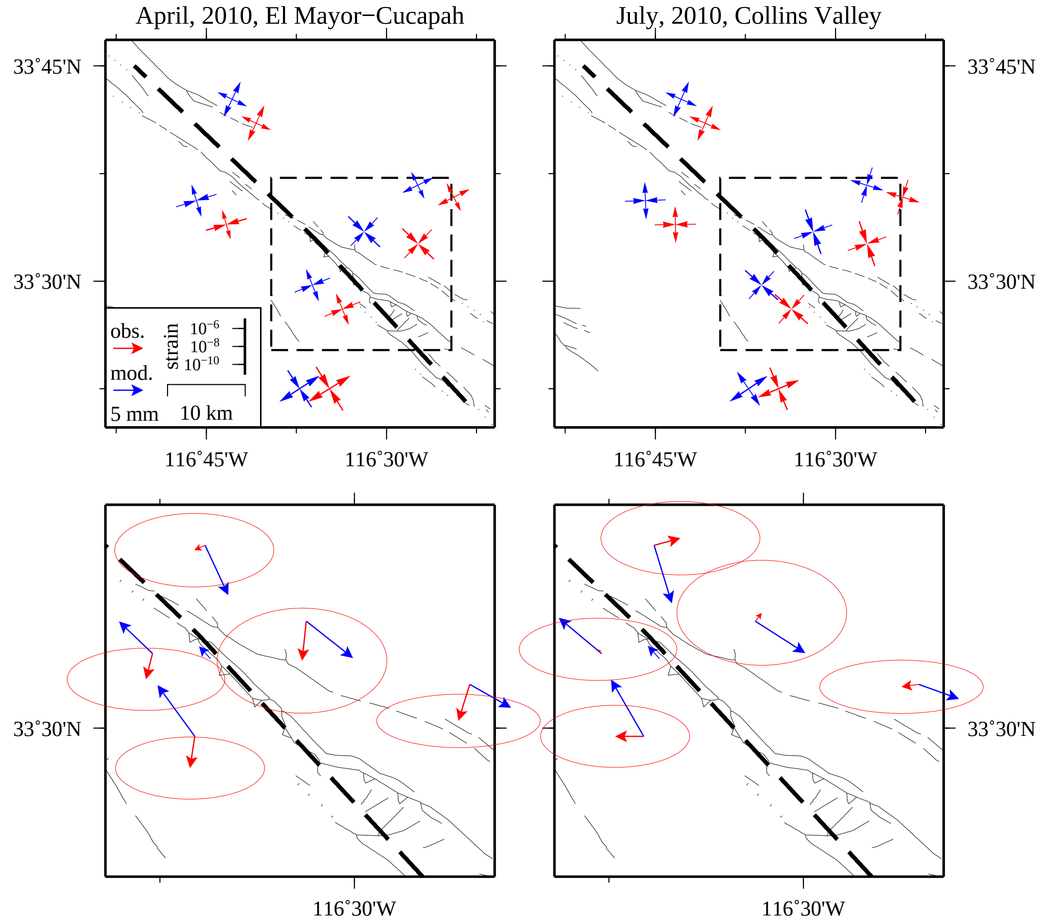

Figure 3.10: Observed and modeled strains and surface displacements for the El Mayor-Cucapah (left) and Collins Valley (right) sequences. Dashed black line indicates the modeled fault trace. Top row: Observed and modeled strains are indicated by red and blue crosses, respectively. Location of observed strains are offset for clarity. The dashed polygons indicate the area covered by the bottom panels. Bottom row: Observed and predicted (using slip models in Figure 3.9) surface displacements at nearby GPS sites are indicated by red and blue vectors, respectively. 1-σ uncertainties are indicated by the red circles.

the slip distribution satisfactorily. We therefore conclude that the estimated moment is robustly constrained by the inversion procedure.

Note that in both sequences, the modeled slip is spatially anti-correlated with aftershock locations. This feature results from our assumption that aftershock rates increase in areas that experience a positive Coulomb stress change due to slip on the main fault. Because of this anti-correlation, the output slip distribution is non-smooth like the spatial aftershock distribution.

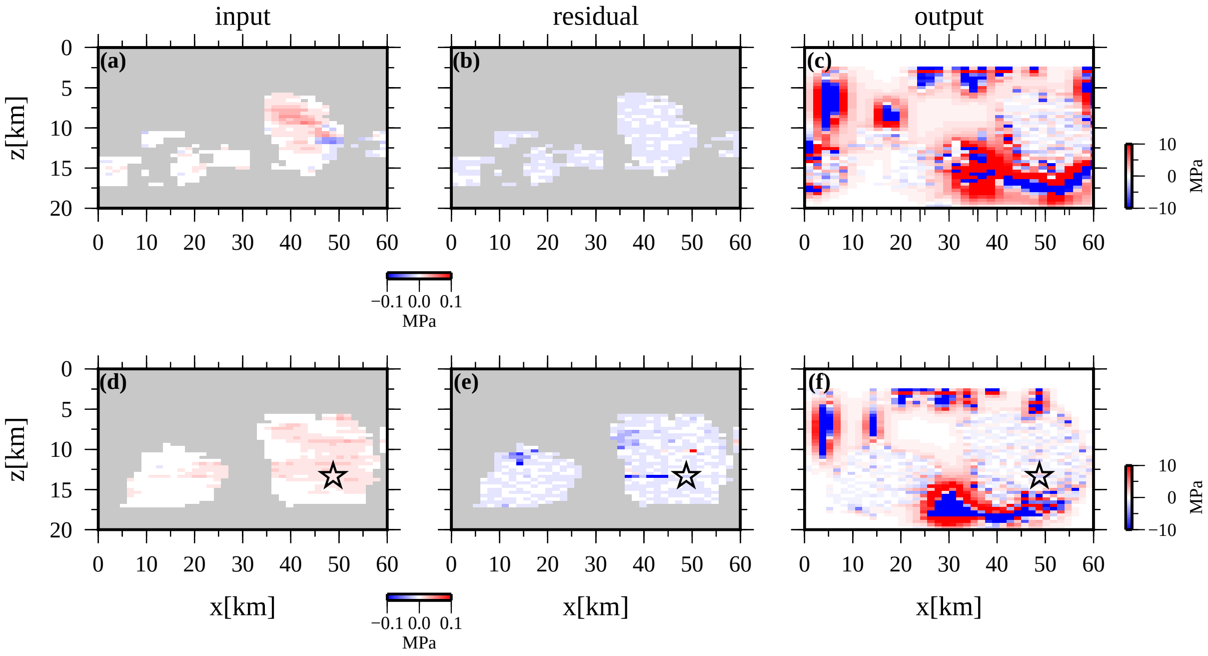

Figure 3.11: Observed and modeled stresses for the El Mayor-Cucapah (top) and Collins Valley (bottom) sequences. Left, middle and right columns are for the inversion input, stress residuals (using the models in Figure 3.9), and output on-fault stresses, respectively. Note the color scale difference between the rightmost and middle columns.

In our preferred models, slip occurs primarily below a dense cluster of aftershocks located southeast of the Anza Gap and extends to the northwest below the Anza segment. The amplitude and location of small slip patches around the SE and NW clusters are mainly constrained by the stress distributions inferred from aftershock activity, while the overall distribution of slip (at length scales larger than about 1 km) is determined primarily by the strain data. In order to obtain a reasonable fit to the data set, slip must occur below the Anza Gap itself. Since the data sensitivity to slip beneath the Anza Gap is small, the solution is distributed over areas that extend as much as 5 and 2.5 km in the along-strike and along-dip directions, respectively. The afterslip distribution along the NW segment is significantly different between the two models: it has larger amplitude and is more compact during the El Mayor-Cucapah sequence than during the Collins Valley sequence. A qualitative difference in the temporal evolution of seismicity in the NW cluster between these two sequences was also demonstrated in Section 3.6.

We find that the spatial distributions of afterslip following the Collins Valley and the

El Mayor-Cucapah mainshocks are complementary (Figure 3.9c). Here, the term complementary is used to indicate little spatial overlap. This is reminiscent of the behavior of earthquakes rupturing fault gaps left unbroken by previous earthquakes and initiating in highly stressed areas at the edges of past ruptures (e.g. Wei et al., 2013; Ye et al., 2014). To the best of our knowledge, this type of behavior has not been observed for aseismically slipping fault segments. Note that the Collins Valley afterslip peaks between 30-40 km along the SJF strike, and that its pattern is anti-correlated with stresses imposed by the early (10 days) post-seismic slip due to the El Mayor-Cucapah earthquake (Figure 3.11c). One interpretation of this observation is that the stress field due to the El Mayor-Cucapah afterslip determined the spatial extent of the Collins Valley afterslip. This is supported by the results presented in Figure 3.11c, which show that the early (10 days) El Mayor-Cucapah afterslip increased the stresses in the area that later hosted the peak Collins Valley afterslip, and that the Collins Valley afterslip termination to the northwest is adjacent to a patch on which the El Mayor-Cucapah afterslip left negative stresses. An alternative interpretation is that the spatial distribution of afterslip is the result of strong heterogeneity of frictional properties within the transition zone.

Our inversions also provide constraints on the product $a\sigma$. The value of a quantifies the sensitivity of friction to logarithmic changes in the sliding velocity of the receiver faults, and therefore this result provides further insight into the mechanical properties within the transition zone. In this paragraph we assume that the effective normal stress σ is hydrostatic with crustal rock density of 2700 kg/m^3. Figures 3.8c-d present the norm of the stress and strain residuals as a function of a for inversions employing a value of β that is equal to 1×10^{-5}. We determine the preferred value of a by performing inversions with a in the range $1 \times 10^{-6} - 1 \times 10^{-1}$. We select the value that best fits (in the least-squares sense) the joint dataset. This corresponds to the minima of the curves in Figure 3.8c-d. For El Mayor-Cucapah, the smallest residuals are obtained with a in the range between 1×10^{-4} and 1×10^{-3}. The uncertainty on this value is quite large, and values as small as 1×10^{-6} provide reasonable fit to the joint dataset. For Collins Valley, our resolution on the value of a is even poorer, and we can only provide an upper bound $a < 10^{-5}$.

The best fit a values are 1 to 4 orders of magnitude smaller than experimental values obtained for granite in the relevant temperature and pressure conditions (Blanpied, Lockner, and Byerlee, 1995), but are generally larger than the value of 1×10^{-4} obtained as an upper bound for the Parkfield using a similar approach (Ziv, 2012). For comparison, Gross and Kisslinger (1997) estimated $a \sim 3 \times 10^{-3}$ from aftershocks triggered by the Landers earthquake and (Thomas et al., 2012) estimated $a\sigma$ values in the range between 0.4 to 1.6 kPa from the response of non-volcanic tremor activity to tidal stresses.

Note that we can only constrain the product $a\sigma$. Different assumptions on the effective normal stresses acting on the fault will affect our estimates of a. For example, a pore pressure higher than hydrostatic will lead to higher values of a. Also note that our analysis provides an estimate of $a\sigma$ averaged over all secondary faults hosting seismicity and not on the main fault strand hosting afterslip, in contrast to approaches such as the one taken by Johnson, Bürgmann, and Larson (2006). The spatial distribution of $a\sigma$ on the main SJF strand may be different than what we obtained for the secondary faults surrounding it.

Using laboratory derived values of a would require much lower effective normal stresses to fit the Collins Value dataset than to fit the El Mayor-Cucapah dataset. At present, we cannot provide a simple explanation for this apparent inconsistency. One alternative is that the difference in the value of a reflects the difference in the distribution of receiver faults between the two sequences, such that information on the value of a in these two sequences originates from essentially different areas. In the SE cluster, the maximum depth of the Collins Valley aftershocks is 1-2 km deeper than the El Mayor-Cucapah early aftershocks (Figure 3.9b and 3.9c). Interestingly, the average depth of seismicity following the 1992 Landers earthquake increased by about 5 km, which was attributed to deepening of the brittle-ductile transition zone following significant post-seismic strain rate increase (Rolandone, Bürgmann, and Nadeau, 2004). The expected strain rate increase in Anza following the remote El Mayor-Cucapah event is much smaller than near the Landers earthquake, which may explain the relatively mild seismicity depth increase. In any case, if a significant portion of stress data for the Collins Valley earthquake is inferred from deeper seismically active patches, then some decrease in the value of a may be expected. However, it seems difficult to reconcile the 1-2 km deepening of seismicity with a 10- to 100-fold decrease in the value of a, unless along-depth frictional properties are extremely heterogeneous.

3.9 Results: Aseismic Slip and Seismicity Triggered by the El Mayor-Cucapah Earthquake Leading to the Collins Valley Earthquake

The El Mayor-Cucapah earthquake triggered an aftershock sequence on the SJF (Figure 3.5), whose rate decayed within 4-5 days to about ten times the pre-mainshock rate (Figure 3.2-top). The new rate persisted through the months leading to the Collins Valley earthquake. This sustained period of elevated seismicity rate includes two M>4 events near the impending Collins Valley hypocenter, 24 days before that mainshock (Figure 3.1). The time between these two events is anomalously short compared to the average interval of 15 months between M4-5 events in the SW cluster since 2001. No significant transient is observed in the strain-meter data between 10 days after the El Mayor-Cucapah mainshock and the Collins Valley mainshock.

The elevated seismicity rates that persisted during the months leading to the Collins Valley mainshock, and the spatial complementarity between the El Mayor-Cucapah and Collins Valley afterslip (Figure 3.9c) are intriguing observations. Stress release by the El Mayor-Cucapah afterslip should have been followed by a gradual return to the background seismicity rates, or even lower, especially given the large amount of post-seismic slip. The average fault slip rate immediately following the El Mayor-Cucapah earthquake increased by a factor larger than 100 relative to the long-term slip rates. A period of increased slip rate must be compensated later by slip rates lower than the long-term average, and hence lead to seismic quiescence as reported in aftershock sequences following small ($M < 2$) earthquakes (Ziv, Rubin, and Kilb, 2003) and, more rarely, following large ($M > 6$) mainshocks (Marsan, 2003). The spatial complementarity between the two events suggests that strong afterslip induced by the El Mayor-Cucapah redistributed stresses in a manner that promoted the failure of the segment hosting the Collins Valley mainshock.

We propose that the El Mayor-Cucapah mainshock initiated a several-months long transient on the SJF, too slow to be detected by the borehole strain-meters. The observed strain-rates indeed decay 10-14 days following the El Mayor-Cucapah earthquake. According to this scenario, the deep afterslip that we imaged using the first 10 days of seismicity and strain data following the El Mayor-Cucapah earthquake (Figure 3.9a,c) continued to accumulate, more slowly, for at least another 80 days. Deep slip during this period may have increased loading on nearby secondary faults, thus triggering seismicity in the SE cluster, and eventually culminating in the Collins Valley earthquake.

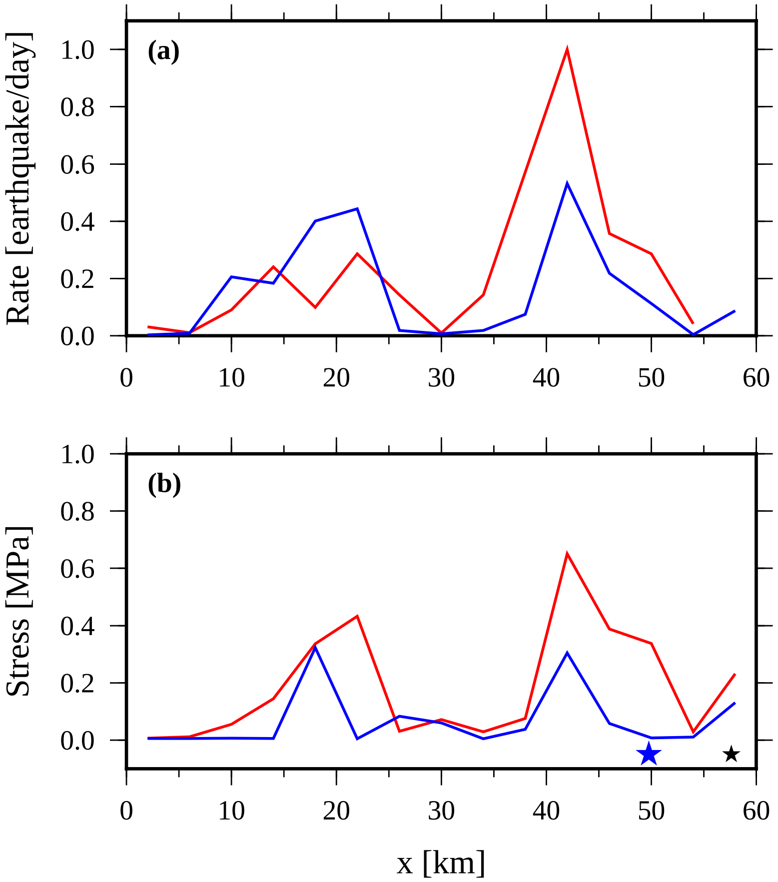

Figure 3.12: Earthquake rates and stresses along the SJF. (a) Seismicity rates as a function of distance along fault strike, from 7 to 14 days (red) and from 14 to 94 days (blue) after the El Mayor-Cucapah earthquake. (b) Cumulative shear stresses inferred from seismicity rates as a function of distance along fault strike, from 0 to 14 days (red) and from 14 to 94 days (blue) after the El Mayor-Cucapah earthquake. Calculations were done using $a = 1\times10^{-3}$. Blue and black stars indicate the location of the July 7, 2010, M5.4 Collins Valley, and the June 13, 2010 M>4 earthquakes, respectively. Seismicity rates and stresses are averaged between 12 and 15 km depth.

In order to test the hypothesis of a deep transient extending up to 94 days following the El Mayor-Cucapah earthquake, we estimate stresses from earthquake rates between April 14 and July 7, 2010. This time window begins when the surface strain signal due the El Mayor-Cucapah afterslip becomes negligible (Figure 3.2) and ends on the day of the Collins Valley earthquake. The duration of this interval is much longer than the intervals we considered in previous sections for the analysis of afterslip induced by the two mainshocks. This complicates the strain data processing and makes our joint approach difficult to implement. We therefore only use stresses inferred from seismicity using the approach outlined in Section 3.3 to crudely characterize the evolution of fault slip.

Figure 3.12 presents the earthquake rates in the weeks leading to the Collins Valley earthquake and the inferred cumulative shear stresses in the region extending out to 3 km on both sides of the SJF strand (between approximately 10 and 15 km depth). These results are consistent with a scenario in which the El Mayor-Cucapah afterslip continued to grow in amplitude and remained relatively stationary in space, thus triggering seismicity in nearby segments. In particular, Figure 3.12a shows that the spatial distribution of seismicity rates is similar in the periods of 7-14 days and 14-94 days following the El-Mayor Cucapah earthquake. As a result, the highly stressed areas on both sides of the Anza Gap inferred for days 0-14 and 14-94 following the El Mayor-Cucapah earthquake are spatially correlated (Figure 3.12b). If afterslip had continued migrating during the months leading to the Collins Valley earthquake at the same rate as during the first days following the El Mayor-Cucapah earthquake, it should have resulted in stress concentrations further away from peak-slip locations inferred in the initial 14 days (Figure 3.9a), as well as in a distinguishable strain signal at the surface. In contrast, we find that high-stress areas are located on segments directly adjacent to the zone of peak-afterslip of El Mayor-Cucapah, while low-stress areas reside within that zone. This spatial pattern resembles the stress field that would have resulted from continuous slip in the segment hosting the peak El Mayor-Cucapah afterslip. The stationarity of the late El Mayor-Cucapah afterslip is further supported by the lack of observed migration of seismicity in that time interval, in contrast to the observed migration of both aftershock sequences (Figures 3.5 and 3.6) which was also confirmed by the rotations of principal strain directions (Figure 3.7).

Stresses to the SE of the peak El Mayor-Cucapah afterslip strongly encourage the Collins Valley mainshock. From the location of peak afterslip, the pre-Collins Valley earthquake shear stresses increase up to about 0.5 MPa near the Collins Valley hypocenter, and are also high near the SE edge of the fault, where two $M \approx 4$ earthquakes occurred 25 days before that event. Such stress levels are extremely high compared to the ambient tectonic stresses acting on the SJF: they are 50 to 100 times larger than the stresses at the Collins Valley hypocentral depth resulting from uniform steady slip below 16 km at 19 mm/year during 90 days.

This analysis suggests that the El Mayor-Cucapah earthquake triggered a long aseismic transient at the bottom of the seismogenic zone, which was accompanied by elevated seismicity rates. The case for sustained seismicity induced by deep aseismic slip due to co-seismic stress redistribution is most clearly exemplified by the Collins Valley sequence.

3.10 Importance of Earthquake Interactions

Earthquakes are known to change the stresses in adjacent regions and trigger their own aftershock sequences and post-seismic slip. Since the stress change in the vicinity of a given aftershock may greatly exceed the stresses imposed in that location by the more distant mainshock or by afterslip, it is not readily apparent which is the dominant mechanism driving seismicity at remote sites. To measure the extent to which earthquake interactions are important in triggering seismicity along the Anza segment, it is instructive to compare the static stress changes transferred by aftershocks to the stresses transferred by aseismic slip. Next, we compare the cumulative stresses in the SE and NW clusters to the output stress distributions in each of the sequences, and show that during both studied sequences, earthquake interactions play a negligible role in aftershock triggering compared to the loading due to aseismic slip.

We start by analyzing the activity in the SE cluster, where most of the strain in both the El Mayor-Cucapah and Collins Valley sequences was released. Given its distance from the El Mayor-Cucapah mainshock, dynamic stresses, which decay slower than static stresses with distance to the mainshock, may have been dominant in triggering aseismic slip in the SE cluster. The expected amplitude of dynamic stresses in Anza due to the passage of seismic waves generated by the El Mayor-Cucapah mainshock is up to several tens of kPa (e.g. Hill, 2012). For comparison, our afterslip distribution implies stress changes of the order of several MPa near the SE cluster (Figure 3.11e). Thus, it is more likely that triggered afterslip was the dominant driver of the sustained seismicity in that cluster during the El Mayor-Cucapah sequence. For the Collins Valley sequence, the large afterslip moment (about 10 times larger than the seismic moment of the mainshock and its aftershocks) suggests also that afterslip is the dominant driver of aftershocks.

Earthquake triggering in the NW cluster is more challenging to explain. That slip is observed to propagate from the SE towards the NW During the El Mayor-Cucapah sequence, and that very few events in that cluster occur prior to the expected arrival of the slip front (Figure 3.5a) seem to suggest that aseismic slip is driving the seismicity in the NW cluster as well. However, several events in that cluster may have been dynamically triggered by seismic waves from the El Mayor or Collins Valley earthquakes, or statically triggered due to long-range elastic interactions following the Collins Valley earthquake, and so one alternative would be that afterslip in the NW cluster was triggered by events occurring in that cluster.

To examine this alternative we compare the static stress changes induced by aftershocks and by the estimated aseismic slip. The slip of each microearthquake is inferred from its seismic moment assuming a standard circular crack Eshelby (1957) with stress drop of 3 MPa, a typical value in Southern California. In most cells, stresses induced by a microearthquake are computed using Okada's stress kernels. In a cell containing a microearthquake stresses induced by earthquake slip are non-uniformly distributed. In such cells we compute the stress at the center of the cell located at a distance x from the center of the crack using the following approximate relation (Dieterich, 1994):

$$\Delta\tau = \begin{cases} -\Delta\tau_e \left[\left(1 - \frac{R^3}{x^3}\right)^{-\frac{1}{2}} - 1 \right], & x > R \\ \Delta\tau_e & x < R \end{cases} \tag{3.17}$$

where $\Delta\tau_e$ and R are the stress drop in the interior of the crack and the crack radius, respectively. The stress changes inside the crack is negative, and thus the negative sign indicates that stress increases outside crack. This relation does not incorporate any azimuthal dependency in the stress distribution, but provides a first-order estimate of the stress decay with distance. To account for the uncertainty in the value of x, we randomly perturb the catalog locations, and report the average values from 50 Monte-Carlo simulations. In addition, to prevent stress singularities from exceeding the elastic strength of the medium, we cap the stresses at the crack tip at a value equal to $0.6 \times \sigma$.

We compare the static stresses due to aftershocks to the stresses from aseismic fault slip during the Collins Valley sequence. Since the number of NW cluster aftershocks is larger and slip along the NW segment is smaller during the Collins Valley sequence than during the El Mayor-Cucapah sequence (Figure 3.9), using the former dataset to test static-stress transfer is more conservative. Figure 3.13 presents the ratio between the sum of stresses due to Collins Valley aftershocks and the stresses due to cumulative afterslip in a 10-day period as a function of position. That ratio is small, it does not exceed 30% in most of the NW cluster. In several locations, however, the stresses imposed by aftershocks greatly exceed the stresses due to afterslip. Such variation occurs on a shorter wavelength than the scale we expect to resolve with the available strain and earthquake data sets. We therefore

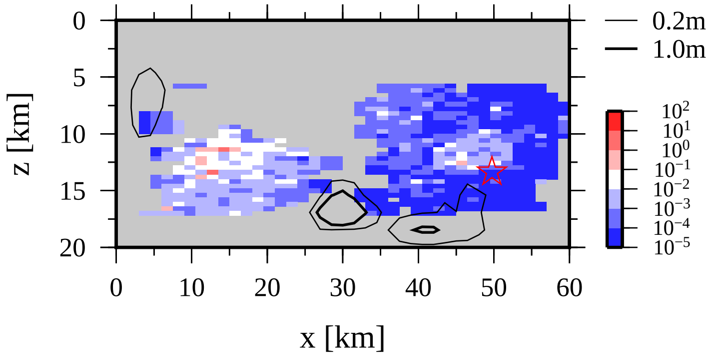

Figure 3.13: Amplitude of shear stress differences between cumulative stresses due to Collins Valley aftershocks and stresses due to the Collins Valley afterslip. Differences are normalized by the stresses due to afterslip. Contours are for the afterslip distribution in Figure 3.9.

conclude that stresses due to long-range static earthquake interactions may explain a small fraction of seismicity in the NW cluster, and that most of the events in this area are triggered by a creep transient initiated near the mainshock.

Creep near the NW cluster during the Collins Valley sequence could have been triggered dynamically due to body-waves or statically due to aseismic slip extending below the Anza Gap from the source region. To examine these two alternatives, we inverted the aftershock and strain data for the cumulative slip distribution in the first day following the mainshock. Due to large errors of the inferred stresses from the rates of aftershocks occurring during the first day following the mainshock (Figure 3.4), the modeled slip is less reliably determined than the one we obtained using 10 days of strain and aftershock data. Accounting for these uncertainties, we find that the stress change near the NW cluster due to static slip occurring in the first day following the Collins Valley mainshock is of the order of about 1 MPa, much larger than the expected dynamic stress change due to body-waves at this site. This implies that aseismic slip in the NW cluster is mainly triggered due to static stresses transfered to the area from creep extending from the SE cluster.

3.11 Importance of Secondary Aftershocks

A major assumption in *Dieterich's* aftershock model is that nucleation sites do not interact: stress perturbations caused by aftershocks are neglected. These additional stresses can trigger secondary aftershocks, which may occur in the days and weeks following the mainshock and at distances of several rupture radii from the mainshock (e.g. Ziv, 2006a). A large fraction of secondary aftershocks relative to direct

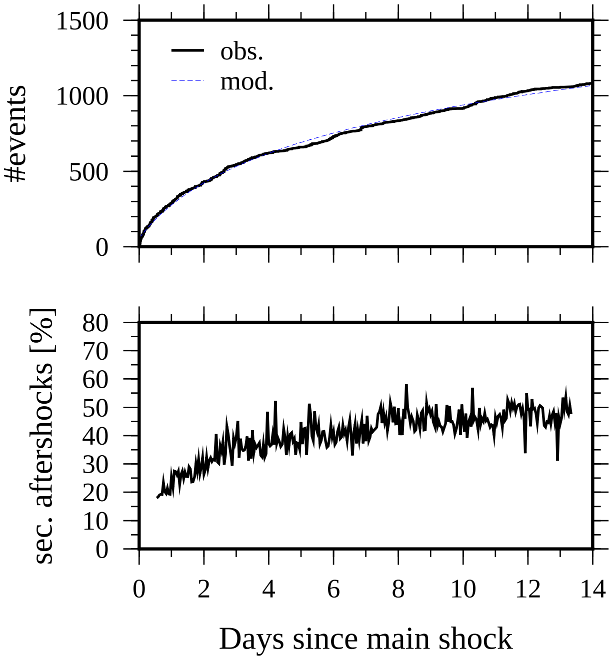

Figure 3.14: Temporal evolution of direct and secondary aftershocks. (a) Observed and modeled aftershock counts for the Collins Valley aftershock sequence. (b) The fraction of secondary aftershocks as a function of time from ETAS simulations.

aftershocks may bias the inferred stresses, and hence the slip model. To assess this potential bias we quantify the importance of secondary aftershocks in the Collins Valley sequence, which contains more events than the El Mayor-Cucapah sequence, and is thus more amenable to the statistical analysis we perform. We will show that secondary aftershocks play a negligible role in transferring stresses during the first few days following the mainshock, the period during which strain rates are highest.

Studies that estimate the fraction of secondary aftershocks usually classify individual events by de-clustering the seismic catalog. Since most de-clustering algorithms use somewhat arbitrary conditions to discriminate between mainshocks, direct, and secondary aftershocks, we choose a different approach to the problem. We generate synthetic earthquake catalogs in which the rates of secondary and direct aftershocks is known, and use these estimates to correct the observed rates for the rates of secondary aftershocks. This approach allows us to infer stresses from the rates of direct aftershocks in our observations. Next, we describe our approach and compare the slip distribution from an inversion in which stress data is based on the rate of direct aftershocks to the distribution presented in Section 3.8.

We generate synthetic catalogs by using an epidemic-type aftershock model (ETAS) (e.g. Ogata, 1999; Felzer and Kilb, 2009). Such statistical models are often used to mimic aftershock distributions by assuming several empirical relations. Here, aftershock rate decays with time since the mainshock according to the modified Omori Law (Utsu, 1961):

$$\dot{N} = \frac{k}{(t+c)^p}, \tag{3.18}$$

where k, c, and p are fitting coefficients that we obtain from modeling the cumulative event counts. The value of the aftershock decay constant, p, is usually near one. For short aftershock sequences, such as the Collins Valley one, it is advantageous to use the cumulative form of Equation 3.18 with $p = 1$ (Ziv, 2006b):

$$N = \int \dot{N} dt = k \ln(t+c) + N_0, \tag{3.19}$$

where N_0 is an integration constant. Figure 3.14 presents the observed and modeled cumulative number of aftershocks as a function of time since the Collins Valley mainshock. The modified Omori law with $p = 1$ provides a good fit to the aftershock data. The second empirical relation describes the distribution of earthquake sizes by a Gutenberg-Richter magnitude-frequency distribution with $b = 1$, which characterizes that distribution in Anza during the 2010 transients. The third empirical relation describes the aftershock density decay as a function of distance to the mainshock by an inverse power-law. The distance decay exponent is set to 1.9, which is more suitable for triggering of direct aftershocks (Marsan and Lengliné, 2010). Tests with values as small as 1.7 (Felzer and Kilb, 2009) gave similar results.

We generate 500 synthetic catalogs by performing 500 ETAS simulations. For each catalog, rates of events with $M > 0.5$ are computed according to the scheme outlined in Section 3.3. In ETAS simulations, secondary aftershocks can be readily distinguished from direct aftershocks. Figure 3.14b presents the rate of secondary aftershocks as a function of time since the mainshock, averaged over the 500 synthetic catalogs. In the first few days, the fraction of secondary aftershocks is less than 30%. We use the results presented in Figure 3.14b to correct the observed rates for the rate of secondary aftershocks. In each time step, the expected fraction of secondary aftershocks is removed from the observations to obtain the rates of direct aftershocks. Using the methodology described in Section 3.3, these rates are used to infer stresses, which are then used as input for the joint inversion (Section 3.7).

Figure 3.15 presents the fractional differences between the slip distribution presented in Figure 3.9 and the slip distribution obtained from inversion in which the input

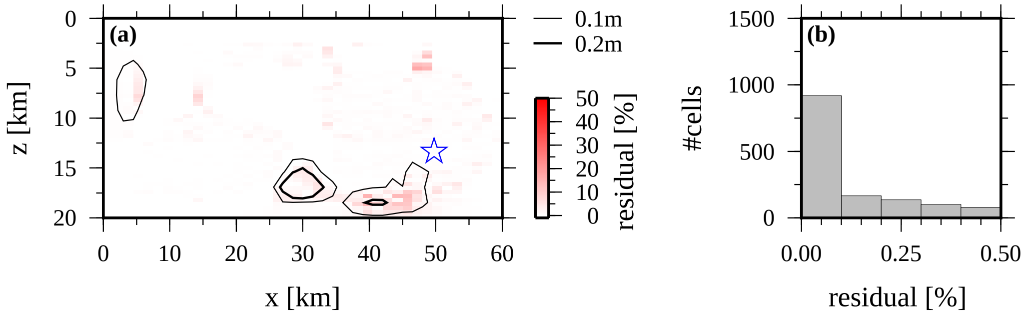

Figure 3.15: Normalized difference between the afterslip distribution in Figure 3.9 and slip from joint inversion with stresses inferred from direct aftershock rates (Figure 3.14). Differences are normalized by the best fit slip distribution. (a) Spatial distribution. Contours indicate inverted afterslip distribution. Star indicates the Collins Valley mainshock hypocenter. (b) Histogram of normalized residuals.

stresses were computed from the rate of direct aftershocks, using the procedure outlined in Section 3.3, with $a = 1 \times 10^{-}5$ and $\beta = 1 \times 10^{-5}$. The value of α_β is determined iteratively as described in Section 3.7. In most areas of the model, and in particular near patches that accumulate substantial post-seismic slip, the difference between the two distributions is less than 10%. This small difference validates *Dieterich's* assumption of non-interacting nucleation sites for the Collins Valley sequence. As shown in Section 3.10, it is the spatiotemporal distribution of afterslip that dictates the dynamics of the system during aftershock sequences in Anza. Since the amplitude of slip decays rapidly with time, our slip estimates are mostly sensitive to early seismicity rates, in periods where the fraction of secondary aftershocks is small.

3.12 Seismic and Aseismic Strain Release along the Anza Segment

The cumulative moment due to aseismic fault slip in the 10 days following the El Mayor-Cucapah and the Collins Valley earthquakes is remarkably large compared to the co-seismic moment of the Collins Valley earthquake, or the total seismic moment of earthquakes during the first 10 days of the El Mayor-Cucapah and Collins Valley aftershock sequences. For large ($M > 7$) earthquakes, equivalent moment of afterslip generally does not exceed 30% of the co-seismic moment (Bürgmann et al., 2002; Chlieh et al., 2007; Y. N. Lin et al., 2013). However, most geodetic studies exclude the first day of post-seismic deformation, and so may underestimate the afterslip moment. Some studies have reported examples where afterslip following a smaller earthquake was much larger than the co-seismic moment. For example, the moment due to afterslip following the 2004 M_w6.0 Parkfield earthquake exceeded the co-seismic moment after 9 months (J. Langbein, Murray, and Snyder, 2006) and was twice as large as the co-seismic moment after 5 years (Bruhat, Barbot, and Avouac, 2011). Murray and Segall (2005) argued that the aseismic moment of episodic slip accompanying 3 $M \approx 4.5$ Parkfield mainshocks was ten times larger than the combined seismic moment of the triggering mainshocks. Yarai and Ozawa (2013) found that moment due to afterslip over an 8 year interval following two events with $M_w6.8$ and $M_w6.7$ in the Hyuga-Nada area, southwest Japan, was about 3 times larger than the sum of the moments of the two mainshocks. These sequences occurred on faults that are known to exhibit steady-state creep interseismically (northwest of Parkfield) or that accommodate large episodic slow-slip events (northwest Japan). If fault strength is rate-and-state dependent, and if the frictional response of patches that slip aseismically is close to velocity neutral, one can expect moderate stress perturbations to trigger large amplitude aseismic slip (e.g. Perfettini and Ampuero, 2008).

3.13 An Alternative Model for Stress Transfer to Seismically Active Cells

The geodetic and seismic data sets allow us to assess whether aftershock seismicity is dominated by stress transfer to off-fault or to on-fault sites. The joint inversion of strain and aftershock data, whose results are presented in Figure 3.9, was preformed under the assumption that transient slip on a main fault strand triggered seismicity at off-fault sites (i.e. secondary faults off the main strand). In this section I examine an alternative mechanism for static stress transfer to aftershock nucleation sites on the main fault strand.

On several well-studied faults, earthquakes tend to occur repeatedly in the same location. These so-called repeaters are composed of tightly clustered microearthquakes, with nearly identical waveforms. Among continental transforms, they are most commonly observed on the Parkfield section of the San Andreas Fault, where their locations well delineate the main fault strand along which they occur. A physical mechanism for explaining repeating earthquakes, which is capable of reproducing observed scaling relations between earthquake recurrence interval and moment, is one in which frictional instabilities nucleate on velocity-weakening patches that are loaded by creep in the surrounding, velocity-strengthening area (e.g. Chen and Lapusta, 2009). Near the Anza segment, however, repeating earthquakes are not a common feature. Anza seismicity is diffuse and extends out to about 2 km on both sides of the fault (Figure 3.1). Such distribution may be the result of geometric irregularities that are an inherent feature of immature fault zones (Powers and Jor-

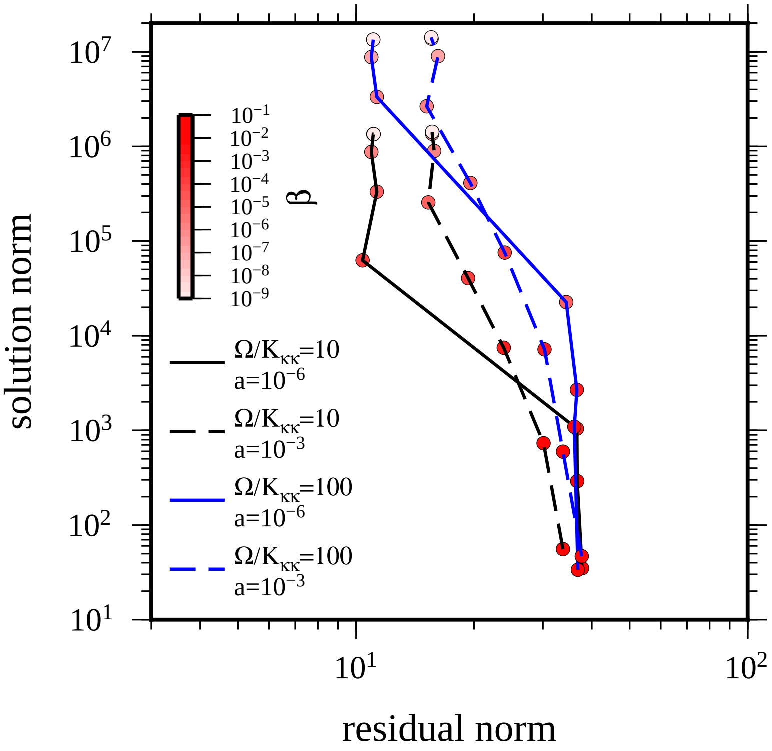

Figure 3.16: Norm of the solution scaled by the value of β as a function of the residual norm for inversions assuming on-fault aftershocks. Solid black and blue curves are for $\Omega/K_{kk} = 10$ and $\Omega/K_{kk} = 100$, respectively. Dashed black and blue curves are for $a = 10^-5$ and $a = 10^-3$, respectively.

dan, 2010). Nonetheless, I wish to exploit the available strain and aftershock data to test the hypothesis that seismic and aseismic patches share the same fault plane. This description is a priori admissible given that the absolute horizontal location uncertainty is about 2 km, which is in the range of distances between aftershocks and the model fault plane.

We consider a model in which seismically active cells are coplanar with the fault surface. We assume that aseismic slip occurs over most of the cell's area and is the primary source of loading on frictionally unstable asperities contained within the cell. The average stress on an asperity with radius R increases due to aseismic slip u outside the asperity by an amount proportional to $\mu u/R$. The stress on the k-th cell is the sum of the average stress on N locked asperities located within that cell and stresses due to slip on all other model cells:

$$\Delta\tau_k = \Omega u_k + \sum_{j\neq k} K_{jk} u_j, \tag{3.20}$$

where the stiffness of a cell containing N seismic asperities is

$$\Omega = \frac{\mu}{N} \sum_i \frac{1}{R_i} + K_{kk}, \tag{3.21}$$

R_i is the radius of the i-th asperity and μ is the shear modulus. The first term on the right hand side of Equation 3.21 is positive. The second term, the self-stiffness K_{kk} of an asperity-free cell, is negative and scales as $-\mu/\Delta x$, where Δx is the shortest cell dimension. For the magnitude range in our catalog, assuming a circular crack model with 3 MPa stress drop, individual asperities are expected to be roughly an order of magnitude smaller than the shortest cell dimension. Since $R_i \ll \Delta x$, the first term dominates and Ω is positive. We determine a uniform value of Ω (the same for all cells) that minimizes the cost function defined by Equation 3.12, through grid search. Setting $a = 10^{-5}$ I find that the best fitting model requires $\Omega \sim 10K_{kk}$ (Figure 3.16). Our estimate of Ω is consistent with our modeling assumptions.

For large values of Ω ($>100K_{kk}$), slightly better results are obtained when the value of a is increased to 10^{-3} (Figure 3.16). Note, however, that the values of Ω and a cannot be arbitrarily large. In the Collins Valley models, using $\Omega > 100$ and $a > 1$ results in output stresses that exceed the shear strength of the media. With larger values ($\Omega \approx 100$ and $a = 10^{-1}$), the misfit is still larger than the misfit of our preferred model developed in the main text (Figure 3.8). This indicates that the off-fault aftershock model is more probable than the on-fault aftershock model.

3.14 Conclusions

The El Mayor-Cucapah earthquake initiated a several-months long transient along the central section of the SJF near Anza. This is manifested by high seismicity rates and periods of elevated surface strain rates. We analyzed two periods of particularly intense seismicity and high surface strain rates. The first, which lasted approximately 10 days after the El Mayor-Cucapah earthquake, is characterized by initial rapid migration of seismicity and afterslip along the SJF strike, and aseismic moment magnitude of 6.1. The second initiated with the Collins Valley earthquake, which occurred 94 days after the El Mayor-Cucapah earthquake. The Collins Valley earthquake also triggered aftershocks and afterslip that migrated along the SJF strike, with afterslip moment magnitude of 5.9.

The joint inversion of strain and seismicity data allows us to resolve slip on deep segments. We model the joint dataset by assuming that slip on the main fault strand triggers seismicity on secondary faults. Our approach does not account for interactions between aftershocks. We find, however, that the effect of earthquake interactions on the slip distribution is small. This is most likely because the moment due to afterslip is much larger than the seismic moment, and thus aseismic fault slip is the dominant driver of seismicity, especially in the more seismically active segment southeast of the Anza Seismic Gap.

The joint dataset requires afterslip to occur at the edges of two large clusters of seismicity adjacent to the Anza Seismic Gap, and beneath the gap itself, at depths of 12 to 17 km. The distribution of afterslip following the El Mayor-Cucapah and Collins Valley earthquakes is complementary. Because afterslip is more important than aftershocks for generating stresses around the Anza segment, this spatial pattern implies that stresses due to the El Mayor-Cucapah afterslip on the SJF triggered the Collins Valley earthquake, and facilitated the large extent of its afterslip. Observations supporting this conclusion are that the Collins Valley earthquake initiated in the area of peak stress left by the El Mayor-Cucapah afterslip, and that the Collins Valley afterslip is spatially correlated with stresses imposed by the first 10 days of El Mayor-Cucapah afterslip.

We find that afterslip generated by El Mayor-Cucapah earthquake propagated rapidly in the first few days and then more slowly, as evidenced by the decaying surface strain rates. The segment hosting the largest afterslip continued slipping at rates that exceed the long-term slip rates, thus stressing nearby fault segments and producing seismicity at a rate 10 times larger than the long-term background seismicity rate. This loading most likely triggered the Collins Valley earthquake, which in turn fed back deep afterslip. The sequence as a whole illustrates the dynamics that can arise from coupling between seismic and aseismic slip. The whole sequence must have increased shear stresses on the locked portion of the SJF in the Anza Seismic Gap.

References

Agnew, D. C. and F. K. Wyatt (2005). “Possible Triggered Aseismic Slip on the San Jacinto Fault”. In: *Southern California Earthquake Center Annual Meeting*. Palm Springs, California.

Agnew, D. C., F. K. Wyatt, et al. (2013). “Strain-Rate Changes Triggered by Local and Regional Earthquakes? Strainmeter Observations in the Anza Section of the San Jacinto Fault”. In: *Southern California Earthquake Center Annual Meeting*. Palm Springs, California.

Allam, A. A. and Y. Ben-Zion (2012). “Seismic velocity structures in the southern California plate-boundary environment from double-difference tomography”. In:

Geophys. J. Int. 190.2, 1181–1196. DOI: `10.1111/j.1365-246X.2012.05544.x`.

Allam, A. A., Y. Ben-Zion, et al. (2014). "Seismic velocity structure in the Hot Springs and Trifurcation areas of the San Jacinto fault zone, California, from double-difference tomography". In: *Geophys. J. Int.* 198.2, 978–999. DOI: `10.1093/gji/ggu176`.

Bailey, I. W. et al. (2010). "Quantifying focal mechanism heterogeneity for fault zones in central and southern California". In: *Geophys. J. Int.* 183.1, 433–450. ISSN: 0956-540X. DOI: `10.1111/j.1365-246X.2010.04745.x`.

Barbour, A. J., D. C. Agnew, and F. K. Wyatt (2015). "Coseismic Strains on Plate Boundary Observatory Borehole Strainmeters in Southern California". In: *Bull. Seismol. Soc. Am.* 105.1, 431–444. ISSN: 0037-1106. DOI: `10.1785/0120140199`.

Bennington, N. et al. (2011). "Aftershock Distribution as a Constraint on the Geodetic Model of Coseismic Slip for the 2004 Parkfield Earthquake". In: *Pure App. Geophys.* 168.10, 1553–1565. DOI: `10.1007/s00024-010-0214-x`.

Blanpied, M. L., D. A. Lockner, and J. D. Byerlee (1995). "Frictional slip of granite at hydrothermal conditions". In: *J. Geophys. Res.* 100.B7, 13045–13064. DOI: `10.1029/95JB00862`.

Bruhat, L., S. Barbot, and J.-P. Avouac (2011). "Evidence for postseismic deformation of the lower crust following the 2004 Mw6.0 Parkfield earthquake". In: *J. Geophys. Res.* 116. DOI: `10.1029/2010JB008073`.

Bürgmann, R. et al. (2002). "Time-dependent distributed afterslip on and deep below the Izmit earthquake rupture". In: *Bull. Seismo. Soc. Am.* 92.1, 126–137. DOI: `10.1785/0120000833`.

Chen, T. and N. Lapusta (2009). "Scaling of small repeating earthquakes explained by interaction of seismic and aseismic slip in a rate and state fault model". In: *J. Geophys. Res.* 114. DOI: `10.1029/2008JB005749`.

Chlieh, M. et al. (2007). "Coseismic slip and afterslip of the great M-w 9.15 Sumatra-Andaman earthquake of 2004". In: *Bull. Seismo. Soc. Am.* 97.1, A, S, S152–S173. DOI: `10.1785/0120050631`.

Dieterich, J. H. (1994). "A constitutive law for rate of earthquake production and its application to earthquake clustering". In: *J. Geophys. Res.* 99.B2, 2601–2618. DOI: `10.1029/93JB02581`.

Dieterich, J. H., V. Cayol, and P. Okubo (2000). "The use of earthquake rate changes as a stress meter at Kilauea volcano". In: *Nature* 408.6811, 457–460. DOI: `10.1038/35044054`.

Eshelby, J. D. (1957). "The determination of the elastic field of an ellipsoidal inclusion, and related problems". In: *Proceedings of the Royal Society of London Series a Mathematical and Physical Sciences* 241.1226, 376–396. DOI: `10.1098/rspa.1957.0133`.

Felzer, K. R. and D. Kilb (2009). "A Case Study of Two M similar to 5 Mainshocks in Anza, California: Is the Footprint of an Aftershock Sequence Larger Than We Think?" In: *Bull. Seismo. Soc. Am.* 99.5, 2721–2735. DOI: `10.1785/0120080268`.

Got, J. L. et al. (2002). "A real-time procedure for progressive multiplet relative relocation at the Hawaiian Volcano Observatory". In: *Bull. Seismo. Soc. Am.* 92.5, 2019–2026. DOI: `10.1785/0120010174`.

Gross, S and C Kisslinger (1997). "Estimating tectonic stress rate and state with Landers aftershocks". In: *J. Geophys. Res.* 102.B4, 7603–7612. DOI: `10.1029/96JB03741`.

Hauksson, E., W. Yang, and P M Shearer (2012). "Waveform Relocated Earthquake Catalog for Southern California (1981 to June 2011)". In: *Bull. Seismo. Soc. Am.* 102.5, 2239–2244. DOI: `10.1785/0120120010`.

Hawthorne, J. C. and A. M. Rubin (2010). "Tidal modulation of slow slip in Cascadia". In: *J. Geophys. Res.* 115. DOI: `10.1029/2010JB007502`.

Hill, D. P. (2012). "Surface-Wave Potential for Triggering Tectonic (Nonvolcanic) Tremor-Corrected". In: *Bull. Seismol. Soc. Am.* 102.6, 2337–2355. DOI: `10.1785/0120120086`.

Hodgkinson, K. et al. (2013). "Tidal calibration of plate boundary observatory borehole strainmeters". In: *J. Geophys. Res.* 118.1, 447–458. DOI: `10.1029/2012JB009651`.

Hsu, Ya-Ju et al. (2006). "Frictional afterslip following the 2005 Nias-Simeulue earthquake, Sumatra". In: *Science* 312.5782, 1921–1926. ISSN: 0036-8075. DOI: `10.1126/science.1126960`.

Johnson, K. M., R. Bürgmann, and K. Larson (2006). "Frictional properties on the San Andreas fault near Parkfield, California, inferred from models of afterslip following the 2004 earthquake". In: *Bull. Seismo. Soc. Am.* 96.4, B, S, S321–S338. DOI: `10.1785/0120050808`.

King, G. C. P., R. S. Stein, and J. Lin (1994). "Static stress changes and the triggering of earthquakes". In: *Bull. Seismol. Soc. Am.* 84.3, 935–953.

Langbein, J., J. R. Murray, and H. A. Snyder (2006). "Coseismic and initial postseismic deformation from the 2004 Parkfield, California, earthquake, observed by global positioning system, electronic distance meter, creepmeters, and borehole strainmeters". In: *Bull. Seismo. Soc. Am.* 96.4, B, S, S304–S320. DOI: `10.1785/0120050823`.

Langbein, John (2015). "Borehole strainmeter measurements spanning the 2014 M-w 6.0 South Napa Earthquake, California: The effect from instrument calibration". In: *J. Geophys. Res.* 120.10, 7190–7202. DOI: `10.1002/2015JB012278`.

Lawson, C. L. and B. J. Hanson (1974). *Solving Least Squares Problems*. Prentice-Hall.

Lengliné, O., B. Enescu, et al. (2012). “Decay and expansion of the early aftershock activity following the 2011, M-w9.0 Tohoku earthquake”. In: *Geophys. Res. Lett.* 39. DOI: `10.1029/2012GL052797`.

Lengliné, O. and D. Marsan (2009). “Inferring the coseismic and postseismic stress changes caused by the 2004 M-w=6 Pa/rkfield earthquake from variations of recurrence times of microearthquakes”. In: *J. Geophys. Res.* 114. DOI: `10.1029/2008JB006118`.

Lin, Y. N. et al. (2013). “Coseismic and postseismic slip associated with the 2010 Maule Earthquake, Chile: Characterizing the Arauco Peninsula barrier effect”. In: *J. Geophys. Res.* 118.6, 3142–3159. DOI: `10.1002/jgrb.50207`.

Linde, A. T. et al. (1996). “A slow earthquake sequence on the San Andreas fault”. In: *Nature* 383.6595, 65–68. DOI: `10.1038/383065a0`.

Lindsey, E. O. and Y. Fialko (2013). “Geodetic slip rates in the southern San Andreas Fault system: Effects of elastic heterogeneity and fault geometry”. In: *J. Geophys. Res.* 118.2, pp. 689–697. DOI: `10.1029/2012JB009358`.

Lindsey, E. O., V. J. Sahakian, et al. (2014). “Interseismic Strain Localization in the San Jacinto Fault Zone”. In: *Pure App. Geophys.* 171.11, pp. 2937–2954. ISSN: 0033-4553. DOI: `10.1007/s00024-013-0753-z`.

Lohman, R. B. and J. J. McGuire (2007). “Earthquake swarms driven by aseismic creep in the Salton Trough, California”. In: *J. Geophys. Res.* 112.B4. DOI: `10.1029/2006JB004596`.

Marsan, D. (2003). “Triggering of seismicity at short timescales following Californian earthquakes”. In: *J. Geophys. Res.* 108.B5. DOI: `10.1029/2002JB001946`.

Marsan, D. and O. Lengliné (2010). “A new estimation of the decay of aftershock density with distance to the mainshock”. In: *J. Geophys. Res.* 115. DOI: `10.1029/2009JB007119`.

Meng, X. and Z. Peng (2014). “Seismicity rate changes in the Salton Sea Geothermal Field and the San Jacinto Fault Zone after the 2010 M-w 7.2 El Mayor-Cucapah earthquake”. In: *Geophys. J. Int.* 197.3, 1750–1762. DOI: `10.1093/gji/ggu085`.

– (2016). “Increasing lengths of aftershock zones with depths of moderate-size earthquakes on the San Jacinto Fault suggests triggering of deep creep in the middle crust”. In: *Geophys. J. Int.* 204.1, pp. 250–261. DOI: `10.1093/gji/ggv445`.

Murray, J. R. and P. Segall (2005). “Spatiotemporal evolution of a transient slip event on the San Andreas fault near Parkfield, California”. In: *J. Geophys. Res.* 110.B9. DOI: `10.1029/2005JB003651`.

Ogata, Y (1999). “Seismicity analysis through point-process modeling: A review”. In: *Pure App. Geophys.* 155.2-4. Workshop on Seismicity Patterns, NIKKO, JAPAN, MAY 11-12, 1998, 471–507. DOI: `10.1007/s000240050275`.

Okada, Y. (1992). “Internal deformation due to shear and tensile faults in a half-space”. In: *Bull. Seismo. Soc. Am.* 82.2, 1018–1040.

Ortega-Culaciati, F. (2013). “Aseismic deformation in subduction megathrusts : central Andes and north-east Japan”. PhD thesis. California Institute of Technology.

Ozawa, S. et al. (2012). “Preceding, coseismic, and postseismic slips of the 2011 Tohoku earthquake, Japan”. In: *J. Geophys. Res.* 117. ISSN: 2169-9313. DOI: `10.1029/2011JB009120`.

Perfettini, H. and J.-P. Ampuero (2008). “Dynamics of a velocity strengthening fault region: Implications for slow earthquakes and postseismic slip”. In: *J. Geophys. Res.* 113.B9. DOI: `10.1029/2007JB005398`.

Perfettini, H. and J.-P. Avouac (2004). “Postseismic relaxation driven by brittle creep: A possible mechanism to reconcile geodetic measurements and the decay rate of aftershocks, application to the Chi-Chi earthquake, Taiwan”. In: *J. Geophys. Res.* 109.B2. ISSN: 2169-9313. DOI: `10.1029/2003JB002488`.

– (2007). “Modeling afterslip and aftershocks following the 1992 Landers earthquake”. In: *J. Geophys. Res.* 112.B7. DOI: `10.1029/2006JB004399`.

Powers, P. M. and T. H. Jordan (2010). “Distribution of seismicity across strike-slip faults in California”. In: *J. Geophys. Res.* 115. DOI: `10.1029/2008JB006234`.

Press, W. H. et al. (1992). *Numerical recipes in C*. New York: Cambridge Univ. Press.

Pritchard, M. E. and M. Simons (2006). “An aseismic slip pulse in northern Chile and along-strike variations in seismogenic behavior”. In: *J. Geophys. Res.* 111.B8. DOI: `10.1029/2006JB004258`.

Rockwell, T. K., T. E. Dawson, et al. (2015). “A 21-Event, 4,000-Year History of Surface Ruptures in the Anza Seismic Gap, San Jacinto Fault, and Implications for Long-term Earthquake Production on a Major Plate Boundary Fault”. In: *Pure App. Geophys.* 172.5, SI, 1143–1165. DOI: `10.1007/s00024-014-0955-z`.

Rockwell, T. K., C. Loughman, and P. Merifield (1990). “Late quaternary rate of slip along the San-Jacinto fault zone near Anza, Southern California”. In: *J. Geophys. Res.* 95.B6, 8593–8605. DOI: `10.1029/JB095iB06p08593`.

Rolandone, F., R. Bürgmann, and R. M. Nadeau (2004). “The evolution of the seismic-aseismic transition during the earthquake cycle: Constraints from the time-dependent depth distribution of aftershocks”. In: *Geophysical Research Letters* 31.23. DOI: `10.1029/2004GL021379`.

Rubin, A. M. (2002). “Aftershocks of microearthquakes as probes of the mechanics of rupture”. In: *J. Geophys. Res.* 107.B7. DOI: `{10.1029/2001JB000496}`.

Salisbury, J. B. et al. (2012). “LiDAR and field observations of slip distribution for the most recent surface ruptures along the central San Jacinto fault”. In: *Bull. Seismo. Soc. Am.* 102.2, 598–619. DOI: `10.1785/0120110068`.

Sanders, C. O. and H. Kanamori (1984). “A seismotectonic analysis of the Anza seismic gap, San-Jacinto fault zone, Southern-California”. In: *J. Geophys. Res.* 89.NB7, 5873–5890. DOI: `10.1029/JB089iB07p05873`.

Schwartz, S. Y. and J. M. Rokosky (2007). “Slow slip events and seismic tremor at circum-pacific subduction zones”. In: *Rev. of Geophys.* 45.3. DOI: `10.1029/2006RG000208`.

Seeber, L. and J. G. Armbruster (2000). “Earthquakes as beacons of stress change”. In: *Nature* 407.6800, 69–72. DOI: `10.1038/35024055`.

Segall, P. (2010). *Earthquake and Volcano Deformation*. Princeton University Press.

Segall, P., E. K. Desmarais, et al. (2006). “Earthquakes triggered by silent slip events on Kilauea volcano, Hawaii”. In: *Nature* 442.7098, 71–74.

Segall, P., A. L. Llenos, et al. (2013). “Time-dependent dike propagation from joint inversion of seismicity and deformation data”. In: *J. Geophys. Res.* 118.11, pp. 5785–5804. DOI: `10.1002/2013JB010251`.

Shearer, P. M., G. A. Prieto, and E. Hauksson (2006). “Comprehensive analysis of earthquake source spectra in southern California”. In: *J. Geophys. Res.* 111.B6. DOI: `10.1029/2005JB003979`.

Smith-Konter, B. R., D. T. Sandwell, and P. Shearer (2011). “Locking depths estimated from geodesy and seismology along the San Andreas Fault System: Implications for seismic moment release”. In: *J. Geophys. Res.* 116.B6. B06401. DOI: `10.1029/2010JB008117`.

Thomas, A. M. et al. (2012). “Tidal triggering of low frequency earthquakes near Parkfield, California: Implications for fault mechanics within the brittle-ductile transition”. In: *J. Geophys. Res.* 117.B5. B05301. DOI: `10.1029/2011JB009036`.

Utsu, T. (1961). “A statistical study on the occurrence of aftershocks”. In: *Gephys. Mag* 30.

Wang, L. et al. (2012). “Stress- and aftershock-constrained joint inversions for coseismic and postseismic slip applied to the 2004 M6.0 Parkfield earthquake”. In: *J. Geophys. Res.* 117. DOI: `10.1029/2011JB009017`.

Wdowinski, S. (2009). “Deep creep as a cause for the excess seismicity along the San Jacinto fault”. In: *Nature Geosci.* 2.12, 882–885. DOI: `10.1038/ngeo684`.

Wei, S. et al. (2013). “Complementary slip distributions of the largest earthquakes in the 2012 Brawley swarm, Imperial Valley, California”. In: *Gephys. Res. Lett.* 40.5, 847–852. DOI: `10.1002/grl.50259`.

Yang, H. et al. (2014). “Low-velocity zones along the San Jacinto Fault, Southern California, from body waves recorded in dense linear arrays”. In: *J. Geophys. Res.* DOI: `10.1002/2014JB011548`.

Yarai, H. and S. Ozawa (2013). “Quasi-periodic slow slip events in the afterslip area of the 1996 Hyuga-nada earthquakes, Japan”. In: *J. Geophys. Res.* 118.5, 2512–2527. DOI: `10.1002/jgrb.50161`.

Ye, L. et al. (2014). “Complementary slip distributions of the August 4, 2003 M-w 7.6 and November 17, 2013 M-w 7.8 South Scotia Ridge earthquakes”. In: *EARTH AND PLANETARY SCIENCE LETTERS* 401, 215–226. DOI: `10.1016/j.epsl.2014.06.007`.

Zigone, D. et al. (2014). In: *Pure App. Geophys.* Pp. 1–26. DOI: `10.1007/s00024-014-0872-1`.

Ziv, A. (2006a). “What controls the spatial distribution of remote aftershocks?” In: *Bull. Seismo. Soc. Am.* 96.6, 2231–2241. DOI: `10.1785/0120060087`.

– (2006b). “On the role of multiple interactions in remote aftershock triggering: The Landers and the Hector Mine case studies”. In: *Bull. Seismo. Soc. Am.* 96.1, 80–89. DOI: `10.1785/0120050029`.

– (2012). “Inference of coseismic slip via joint inversion of GPS and aftershock data: The 2004 Parkfield example”. In: *J. Geophys. Res.* 117. DOI: `10.1029/2011JB008400`.

Ziv, A., A. M. Rubin, and D. Kilb (2003). “Spatiotemporal analyses of earthquake productivity and size distribution: Observations and simulations”. In: *Bull. Seis. Soc. Am.* 93.5, 2069–2081. DOI: `{10.1785/0120020117}`.

4

SUMMARY AND PERSPECTIVES

The Long-Beach (LB) and Rosecrans array deployments have provided us with rich datasets with which we were able to probe the deep seismogenic extension of the Newport-Inglewood Fault Zone (NIFZ). We showed that the transition from the upper, frictionally unstable to the lower, predominantly stable portion of the NIFZ beneath LB is characterized by the localization of seismicity, and by a transition in earthquake scaling properties. We postulate that this transition may be the result of a reduction in earthquake interactions due to rheological and/or geometrical factors.

We provide several evidence which suggest that deep deformation along the NIFZ may be regarded as paradoxical. Low deformation rates, both in comparison to other locations along the NIFZ strike or to other faults in the region, suggest that the section we focus on should not contain deep earthquakes. Moreover, given the local geotherm, many of the earthquakes we image nucleate at depths where rocks are expected to deform in a ductile manner. Most importantly, the observed seismicity progressively concentrates with increasing depth, in a manner that is generally observed in the shallow crust, but is unexpected at upper mantle conditions.

The paucity of deep seismicity along the San Andreas Fault System (SAFS) is puzzling. Active segments along this plate boundary are monitored with advanced networks, and both field and lab data suggest that earthquake nucleation at large depths and elevated temperatures is certainly plausible. However, lower-crustal seismicity, which is observed along both convergent and divergent margins that are relatively sparsely instrumented (Emmerson et al., 2006; Craig et al., 2011; Leyton et al., 2009), is almost entirely absent from the SAFS. This raises the question whether deep seismicity is limited to the NIFZ, or whether it could be detected along other faults once more dense array data become available. Future installations of 3-component nodes in dense arrays will extend our monitoring capabilities along major crustal faults. Such experiments are already underway, and will allow us to utilize advanced array processing techniques to better resolve incoming wavefronts generated by deep microearthquakes.

Earthquakes are regarded as the result of a frictional instabilities, and as such, their occurrence in lower-crustal and upper-mantle conditions is challenging to explain.

For instabilities to nucleate spontaneously shear resistance must weaken with fault slip at a rate that is faster than the effective elastic stiffness of the surrounding medium (Scholz, 1998). In the temperature range that prevails at the base of the crust, the condition for the onset of unstable sliding may be more easily met if the fault cuts through mafic-mineral-bearing rocks. However, recent laboratory studies show that frictional strength of Granite may be velocity weakening when sliding at temperatures as high as 600°C (Mitchell, Fialko, and Brown, 2016). In laboratory experiments olivine gouge exhibits velocity weakening behavior between 600-800°C, with dislocation glide interpreted as the dominant asperity-scale deformation mechanism, and transitions to velocity strengthening outside that range (King and Marone, 2012). Both temperature range and deformation mechanism are consistent with evidence from exhumed peridotites which were seismically deformed at lower crustal depths (Ueda et al., 2008; Matysiak and Trepmann, 2012). Ductile instabilities may nucleate in a mafic rock under high temperatures within a wide shear zone (>1 km), and/or under high strain rates (Hobbs, Ord, and Teyssier, 1986), in the range usually associated with seismic slip. Experiments (Miguel et al., 2001; Weiss and Marsan, 2003) and numerical simulations (Miguel et al., 2001; Csikor et al., 2007) show that instabilities nucleating in viscous materials are temporally and spatially clustered and their size distribution exhibits non-power-law tails (Csikor et al., 2007), reminiscent of the rapid fall-off of earthquake counts with increasing magnitude we observed beneath LB.

We showed that information on the time-space evolution of seismicity in Anza is crucial for understanding transient fault behavior in that area. The deployment of geodetic and seismic network, together with new satellite imagery with dense spatio-temporal coverage of many seismically active faults, will allow the implementation of joint geodetic-seismic approaches in other tectonic environments. A possible candidate for this type of research are Episodic Tremor and Slow-Slip (ETS), which regularly occur in central Cascadia at 2-years intervals, and are accompanied by intense tremor activity occurring in the periphery of the slow-slip front. Geodetic inversions show that slow-slip and tremor migrate together, but their results are smooth such that features separated by less than 50 km are not well resolved (e.g. Bartlow et al., 2011). The observation that interactions during ETS occur on much smaller scales (Rubin and Armbruster, 2013), warrants a joint approach for analyzing the tremor catalog and geodetic data. With the incorporation of several new data, our joint methodology will become well-fitted to study Cascadia ETS. Available tremor catalogs are precise enough (≈1 km location uncertainty) to ensure that tremor rates at a given location may be used to infer stresses. Additionally, slow-slip events have recently been shown to correlate well with ocean tides (Hawthorne and Rubin, 2010), such that the stresses imposed by the latter can be used as an additional constraint on the slip inversion. The joint approach may provide important insights onto complex mechanical processes controlling the style and degree of stress transfer between slow-slip and tremor observed in Cascadia.

Strain and seismicity may be jointly used to effectively monitor transitory fault slip behavior. In Anza, strain and seismicity are spatio-temporally correlated during several-week-long periods of rapid deformation. These datasets may also be used to study the pattern of strain accumulation in Anza on time scales of several months, thus increasing the likelihood of detecting smaller transients. The $M_w \approx 6$ transient slip events we imaged (Chapter 2) give rise to strain signals that are well above the instruments noise levels in most stations. We expect that slip events that are at least one unit of magnitude smaller would also be visible in the raw records. Even smaller events may be detected if the signal-to-noise ratio is increased by using more advanced strain-data processing techniques than the one presented in Section 3.3. These efforts may provide additional information on the scaling of slow-earthquakes near the observational limits, a topic of recent debate (Gomberg et al., 2016), with important implications on the physics of earthquake sources.

References

Bartlow, N. M. et al. (2011). "Space-time correlation of slip and tremor during the 2009 Cascadia slow slip event". In: *Geophys. Res. Lett.* 38. DOI: `{10.1029/2011GL048714}`.

Craig, T. J. et al. (2011). "Earthquake distribution patterns in Africa: their relationship to variations in lithospheric and geological structure, and their rheological implications". In: *Geophys. J. Int.* 185.1, pp. 403–434. ISSN: 1365-246X. DOI: `10.1111/j.1365-246X.2011.04950.x`.

Csikor, F. F. et al. (2007). "Dislocation avalanches, strain bursts, and the problem of plastic forming at the micrometer scale". In: *Science* 318.5848, 251–254. DOI: `{10.1126/science.1143719}`.

Emmerson, B. et al. (2006). "Seismicity, structure and rheology of the lithosphere in the Lake Baikal region". In: *Geophys. J. Int.* 167.3, pp. 1233–1272. ISSN: 1365-246X. DOI: `10.1111/j.1365-246X.2006.03075.x`.

Gomberg, J. et al. (2016). "Reconsidering earthquake scaling". In: *Geophys. Res. Lett.* 43.12. 2016GL069967, pp. 6243–6251. ISSN: 1944-8007. DOI: `10.1002/2016GL069967`. URL: `http://dx.doi.org/10.1002/2016GL069967`.

Hawthorne, J. C. and A. M. Rubin (2010). “Tidal modulation of slow slip in Cascadia”. In: *J. Geophys. Res.* 115. doi: `10.1029/2010JB007502`.

Hobbs, B. E., A. Ord, and C. Teyssier (1986). “Earthquakes in the ductile regime?” In: *Pure and Applied Geophysics* 124.1-2, pp. 309–336. issn: 0033-4553. doi: `10.1007/BF00875730`.

King, D. S. H. and C. Marone (2012). “Frictional properties of olivine at high temperature with applications to the strength and dynamics of the oceanic lithosphere”. In: *J. Geophys. Res.* 117. doi: `{10.1029/2012JB009511}`.

Leyton, F. et al. (2009). “Anomalous seismicity in the lower crust of the Santiago Basin, Chile”. In: *Physics of the Earth and Planetary Interiors* 175.1-2, 17–25. issn: 0031-9201. doi: `{10.1016/j.pepi.2008.03.016}`.

Matysiak, A. K. and C. A. Trepmann (2012). “Crystal-plastic deformation and recrystallization of peridotite controlled by the seismic cycle”. In: *Tectonophys.* 530, pp. 111–127. doi: `10.1016/j.tecto.2011.11.029`.

Miguel, M. C. et al. (2001). “Intermittent dislocation flow in viscoplastic deformation”. In: *Nature* 410.6829, pp. 667–671. doi: `10.1038/35070524`.

Mitchell, E. K., Y. Fialko, and K. M. Brown (2016). “Velocity-weakening behavior of Westerly granite at temperature up to 600°C”. In: *J. Geophys. Res.* 2016JB013081. issn: 2169-9356. doi: `10.1002/2016JB013081`. url: `http://dx.doi.org/10.1002/2016JB013081`.

Rubin, A. M. and J. G. Armbruster (2013). “Imaging slow slip fronts in Cascadia with high precision cross-station tremor locations”. In: *Geochem. Geophys Geosys.* 14.12, 5371–5392. doi: `{10.1002/2013GC005031}`.

Scholz, C. H. (1998). “Earthquakes and friction laws”. In: *Nature* 391.6662, pp. 37–42. doi: `10.1038/34097`.

Ueda, T. et al. (2008). “Mantle earthquakes frozen in mylonitized ultramafic pseudotachylytes of spinel-lherzolite facies”. In: *Geology* 36.8, pp. 607–610. issn: 0091-7613. doi: `10.1130/G24739A.1`.

Weiss, J. and D. Marsan (2003). “Three-Dimensional Mapping of Dislocation Avalanches: Clustering and Space/Time Coupling”. In: *Science* 299.5603, pp. 89–92. doi: `10.1126/science.1079312`.

A

JOINT INVERSION PROCESSING SCHEME

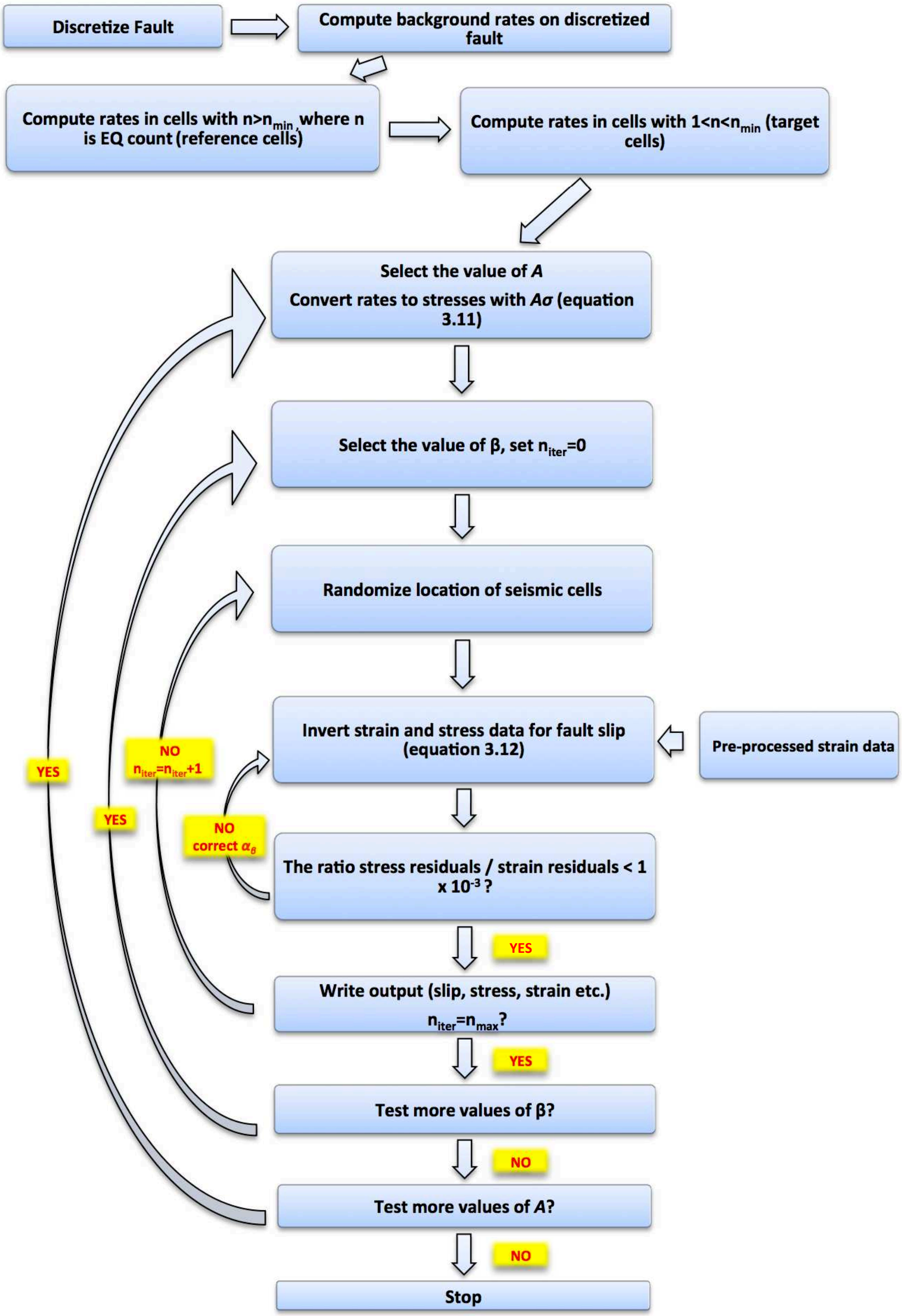
Discretize Fault
Compute background rates on discretized fault
Compute rates in cells with $n>n_{min}$, where n is EQ count (reference cells)
Compute rates in cells with $1<n<n_{min}$ (target cells)
Select the value of *A*
Convert rates to stresses with $A\sigma$ (equation 3.11)
Select the value of β, set $n_{iter}=0$
Randomize location of seismic cells
Invert strain and stress data for fault slip (equation 3.12)
Pre-processed strain data
The ratio stress residuals / strain residuals < 1×10^{-3} ?
NO correct α_β
YES
Write output (slip, stress, strain etc.)
$n_{iter}=n_{max}$?
NO $n_{iter}=n_{iter}+1$
YES
Test more values of β?
YES
NO
Test more values of *A*?
YES
NO
Stop